

UNIVERSITY OF OKLAHOMA

GRADUATE COLLEGE

INVESTIGATION OF ELECTROSPINNING PROCESS PARAMETERS AND  
STUDIES OF STABILIZATION KINETICS OF POLYACRYLONITRILE-BASED  
ELECTROSPUN CARBON NANOFIBERS

A DISSERTATION

SUBMITTED TO THE GRADUATE FACULTY

in partial fulfillment of the requirements for the

Degree of

DOCTOR OF PHILOSOPHY

By

BIPUL BARUA  
Norman, Oklahoma  
2015

INVESTIGATION OF ELECTROSPINNING PROCESS PARAMETERS AND  
STUDIES OF STABILIZATION KINETICS OF POLYACRYLONITRILE-BASED  
ELECTROSPUN CARBON NANOFIBERS

A DISSERTATION APPROVED FOR THE  
SCHOOL OF AEROSPACE AND MECHANICAL ENGINEERING

BY

---

Dr. Mrinal C. Saha, Chair

---

Dr. M. Cengiz Altan

---

Dr. Zahed Siddique

---

Dr. Yingtao Liu

---

Dr. Daniel E. Resasco

© Copyright by BIPUL BARUA 2015  
All Rights Reserved.

## ACKNOWLEDGEMENTS

The work presented in this dissertation would not have been possible without my close association with many people. It is a great pleasure to express my sincere gratitude and appreciation to all those who made this dissertation possible. I would first like to thank Dr. Mrinal C. Saha, my dissertation committee chair and advisor, for his dedicated help, advice, inspiration, encouragement and continuous support, throughout my graduate study. I would also like to thank him for keeping his trust in my ability, and giving me the opportunity to work on various interesting research projects. My special words of thanks go to Dr. M. Cengiz Altan for his continuous encouragement and motivation to keep up the good work. I also thank him for providing me with the high voltage power system. I owe my deepest gratitude to Dr. Brian P. Grady for his tireless help with X-ray scattering measurements. I would like to recognize the efforts of the other committee members, Dr. Daniel E. Resasco, Dr. Zahed Siddique, and Dr. Yingtao Liu, for their comments and suggestions which positively guided this work. My heartfelt thanks go to Mr. Billy Mays and Mr. Gregory Williams. The experimental work presented in this study would not have been possible without their help. I also thank Mr. Carl B. Van Buskirk and Mr. Chad E. Cunningham for assisting with high voltage power cable. I would like to extend my gratitude to the all of the faculty and staff members and my colleagues in the AME department at OU. Finally, special recognition goes out to my parents, brother, and Neelima for their continued moral support without which none of this would have been possible.

## TABLE OF CONTENTS

ACKNOWLEDGEMENTS .....	iv
TABLE OF CONTENTS .....	v
LIST OF TABLES .....	ix
LIST OF FIGURES .....	x
ABSTRACT .....	xvi
Chapter 1: INTRODUCTION .....	1
1.1 Carbon Fibers.....	1
1.2 Challenges with Conventional Spinning Methods for Further Improving the Mechanical Strength of Carbon Fibers .....	6
1.3 Vapor Grown Carbon Fibers and Nanofibers .....	9
1.4 Carbon Nanotubes.....	11
1.5 Current Challenges with VGCNFs and CNTs.....	12
1.6 Electrospinning: An Innovative Technique to Produce Continuous Carbon Nanofiber with a High Degree of Morphological and Structural Perfection.....	13
1.7 Fabrication of ECNFs from PAN Nanofibers.....	16
1.7.1 PAN.....	17
1.7.2 Heat Treatment of electrospun PAN Nanofiber.....	20
1.8 Scope of the Work .....	21
PART I: INVESTIGATION OF THE GOVERNING PARAMETERS IN THE ELECTROSPINNING OF POLYACRYLONITRILE NANOFIBERS.....	23
Chapter 2: ELECTROSPINNING.....	23
2.1 History .....	23
2.2 Fundamental Theory .....	25
2.3 Applications of Electrospun Nanofibers.....	27
2.4 Electrospinning Processing Parameters .....	28
2.4.1 Solution Parameters .....	28
2.4.2 Operational Parameters .....	30
2.4.3 Environmental Parameters .....	31
2.5 Key Research Questions – Part I .....	33
Chapter 3: ALIGNMENT OF ELECTROSPUN NANOFIBERS .....	36
3.1 Introduction.....	36

3.2 Review on Electrospinning Designs and Nanofiber Assemblies.....	36
3.3 Design of Electrospinning Setup .....	40
3.4 Effect of Collector Surface Velocity on Fiber Alignment .....	42
3.5 Chapter Conclusions .....	43
Chapter 4: INVESTIGATION OF ELECTRIC FIELD AND FLOW RATE .....	44
4.1 Introduction.....	44
4.2 Experimental.....	45
4.2.1 Polyacrylonitrile (PAN)/DMF Solution Preparation .....	45
4.2.2 Electrospinning Process .....	45
4.2.3 Yarn Preparation .....	46
4.2.4 Taylor Cone Analysis.....	47
4.2.5 Fiber Current Measurement .....	47
4.2.6 Diameter Distribution Characterization .....	51
4.2.7 Mechanical Testing .....	51
4.3 Results and Discussion .....	52
4.3.1 Investigation on Taylor cone Morphology.....	52
4.3.2 Upper and Lower Bounds of Flow Rate for Continuous Jet.....	55
4.3.3 Investigation on Fiber Current .....	56
4.3.4 Diameter Distribution of Electrospun Nanofibers .....	59
4.3.5 Effect of Electric Field and Flow Rate on Nanofiber Diameter.....	61
4.3.6 Mechanical Properties of Electrospun Nanofiber Yarns.....	62
4.3.6.1 Effect of Filament Diameter .....	62
4.3.6.2 Continuous Jet vs Discontinuous Jet .....	64
4.3.6.3 Effect of Flow Rate .....	65
4.3.7 Modeling of the Nanofiber Diameter .....	67
4.4 Chapter Conclusions .....	69
Chapter 5: INVESTIGATOIN OF RELATIVE HUMIDITY (RH) AND TEMPERATURE.....	70
5.1 Introduction.....	70
5.2 Ternary Phase Diagram .....	72
5.3 Experimental.....	76
5.3.1 Electrospinning Process .....	76
5.3.2 Characterization Techniques .....	77

5.4 Results and Discussion .....	79
5.4.1 Construction of Ternary Phase Diagram for Water/DMF/PAN System.....	80
5.4.2 Surface Morphology of Electrospun Nanofibers .....	82
5.4.2.1 Effect of RH .....	82
5.4.2.2 Effect of Temperature.....	84
5.4.2.3 Effect of Annealing .....	86
5.4.3 Interior Structure of Electrospun Nanofibers .....	87
5.4.3.1 Effect of RH and Temperature .....	87
5.4.3.2 Effect of Annealing .....	89
5.4.4 Bead Formation and Diameter Distribution of Electrospun Nanofibers.....	91
5.4.4.1 Mechanism of Bead Formation .....	91
5.4.4.2 Mechanism of Pores on Beads .....	91
5.4.4.3 Effect of RH, Temperature and Annealing on Fiber Diameter .....	93
5.4.4.4 Isolation of Two Mechanisms for Diameter Variation.....	94
5.4.5 Mechanical Properties of Electrospun Nanofiber Yarns.....	99
5.4.5.1 Effect of Humidity and Temperature .....	99
5.4.5.2 Effect of Annealing .....	101
5.5 Chapter Conclusions .....	103
<b>PART II: STABILIZATION STUDIES OF ELECTROSPUN PAN NANOFIBERS</b>	<b>105</b>
<b>Chapter 6: STABILIZATION OF PAN FIBERS</b> .....	<b>105</b>
6.1 Introduction.....	105
6.2 Stabilization Chemistry.....	106
6.2.1 Cyclization Reaction .....	106
6.2.2 Oxidation Reaction.....	107
6.2.3 Dehydrogenation Reaction.....	108
6.2.4 Cross-linking Reaction.....	109
6.2.5 Volatile Byproducts during Stabilization.....	109
6.2.6 Effect of Co-monomer .....	110
6.3 Methods to Characterize Stabilization .....	111
6.4 Overview of Research on Stabilization of Electrospun PAN Nanofibers .....	113
6.5 Key Research Questions – II .....	113
<b>Chapter 7: IN SITU CHARACTERIZATION AND KINETICS OF STABILIZATION REACTIONS</b> .....	<b>115</b>

7.1 Introduction.....	115
7.2 Experimental.....	115
7.2.1 Electrospun Nanofiber Production.....	115
7.2.2 In situ Characterization Techniques.....	115
7.3 Results and Discussion .....	116
7.3.1 Separation of Different Stabilization Reactions.....	116
7.3.2 Evolution of Kinetic Parameters of the Stabilization Reactions.....	118
7.3.3 Reaction Shrinkage in PAN Nanofiber Yarn during Stabilization .....	123
7.3.4 Dynamic Mechanical Properties of PAN Nanofiber Yarn during Stabilization .....	130
7.4 Chapter Conclusions.....	133
Chapter 8: OPTIMIZATION OF STABILIZATION TIME.....	134
8.1 Introduction.....	134
8.2 Experimental.....	134
8.2.1 Stabilization Process .....	134
8.2.2 Carbonization Process.....	135
8.2.3 Characterization Techniques.....	136
8.2.3.1 WAXD.....	136
8.2.3.2 Tensile Testing of ECNF Yarn.....	136
8.2.3.3 SEM.....	139
8.3 Results and Discussion .....	139
8.3.1 WAXD Analysis of Stabilized Nanofibers .....	139
8.3.2 Effect of Stabilization Time on Mechanical Properties of ECNFs .....	141
8.3.3 Effect of Constant Length Stabilization on Final ECNFs .....	142
8.4 Chapter Conclusions.....	146
Chapter 9: CONCLUDING REMARKS.....	147
9.1 Inferences.....	147
9.2 Contributions .....	149
9.3 Recommendations for Future Work .....	150
REFERENCES.....	153



## LIST OF TABLES

<b>Table 3.1</b> Schematic of various electrospinning setups with rotating collectors, and their advantages and disadvantages. ....	39
<b>Table 4.1</b> Comparison between estimated theoretical current and experimentally determined current. ....	51
<b>Table 5.1</b> Interaction parameters required to calculate ternary phase diagram of water/DMF/PAN system. ....	79
<b>Table 5.2</b> Isolating the effect of volumetric charge density and phase demixing on the average diameter of nanofibers electrospun at 20°C. ....	97
<b>Table 7.1</b> DSC peak maxima for electrospun PAN nanofibers in various gas environments. ....	120
<b>Table 7.2</b> Calculated kinetic parameters determined by Kissinger's and Ozawa's methods. ....	123
<b>Table 7.3</b> Isothermal time at various final temperatures to reach to the maximum shrinkage. ....	130
<b>Table 7.4</b> Calculated isothermal time at various final temperature to reach to the maximum storage modulus and loss modulus. ....	133
<b>Table 8.1</b> Tensile properties of carbonized nanofiber yarns after stabilization at 260°C for various times. No constraint was applied during stabilization and carbonization..	142
<b>Table 8.2</b> Tensile properties of carbonized nanofiber yarns after constant length stabilization at 260°C for various times. No tension was applied during carbonization. ....	144

## LIST OF FIGURES

<b>Figure 1.1</b> Schematic of CF productions from PAN and pitch precursors.....	4
<b>Figure 1.2</b> SEM micrographs (top) and corresponding structural models (bottom) of PAN-based (a, c) and mesophase pitch-based (b, d) CFs [6].....	5
<b>Figure 1.3</b> Schematic representation of various types of structural imperfections in CFs [8]. .....	8
<b>Figure 1.4</b> Schematic of (a) platelet and (b) staked cup type VGCFs and VGCNFs [11]. .....	8
<b>Figure 1.5</b> Schematic of the growth of VGCFs and VGCNFs (a) on a substrate and (b) in a gas flow [12].....	10
<b>Figure 1.6</b> Schematic showing (a) SWNT and (b) MWNT.....	11
<b>Figure 1.7</b> (a) Comparison of CF and ECNF. Comparison of (b) VGCNFs and (c) ECNFs showing significantly better nanofiber uniformity and sample purity [26]. .....	16
<b>Figure 1.8</b> Schematic figure of PAN molecule.....	18
<b>Figure 1.9</b> (a) Helical structure of PAN chains. (b) Morphological model of PAN fiber showing ordered and disordered regions [44]. .....	19
<b>Figure 2.1</b> Statistics of published research articles about electrospinning (Source: Web of Science Database, keyword: “electrospinning”). .....	24
<b>Figure 2.2</b> A schematic representation of electrospinning technique.....	26
<b>Figure 2.3</b> SEM images of electrospun PS fibers from various concentrations of (a) 5 wt%, (b) 10 wt%, (c) 20 wt%, and (d) 30 wt% [98].....	29
<b>Figure 3.1</b> (a) Schematic diagram of parallel auxiliary electrode arrangement. (b) Electric field profile from the spinneret to the parallel auxiliary electrodes. (c) Analysis of the electrostatic force on a charged nanofiber spanning across the gap. (d) Dark field optical micrograph of the nanofibers collected across the gap between two silicon stripes. (e) SEM image of the nanofibers taken from the region close to the edge of silicon strip [127].....	38
<b>Figure 3.2</b> A schematic of the electrospinning setup.....	41
<b>Figure 3.3</b> A photograph of the electrospinning setup. ....	41

<b>Figure 3.4</b> SEM images of electrospun PAN nanofibers collected onto the collector disc rotating at (a) 50 rpm, (b) 200 rpm, (c) 400 rpm, (d) 600 rpm, and (e) 800 rpm. ....	42
<b>Figure 4.1</b> Photographs showing (a) peeling off the PAN nanofiber yarn from the copper foil on the rotating disc and (b) drying rack with nanofiber yarns mounted. ....	46
<b>Figure 4.2</b> Optical image of the Taylor cone region (a) and its binary image (b) after processing using ImageJ software. ....	47
<b>Figure 4.3</b> Schematic representation of electrospinning process along with fiber current measurement technique. ....	48
<b>Figure 4.4</b> Circuit with known voltage and resistance for validation of the nA current measurement. ....	48
<b>Figure 4.5</b> Open circuit and 163.8 nA theoretical current reading of the multimeter. ..	50
<b>Figure 4.6</b> Anderson-darling normality test for the data shown in Fig. 4. (a) Open circuit reading, (b) 163.8 nA theoretical current reading. ....	50
<b>Figure 4.7</b> Various Taylor cone morphologies observed at different flow rates operating at 15 kV electric field. 1- Dripping, 2- Jet with intermittent drops (bottom: change in Taylor cone shape right at the time of drop falling), 3 - continuous jet with large, bounded variations, 4 - continuous jet with minimal fluctuations, 5 - narrow, variable continuous jet, 6 - discontinuous jet (top), no jet (bottom). ....	53
<b>Figure 4.8</b> Taylor cone angles for various regimes of interest (regime 2-5). ....	55
<b>Figure 4.9</b> Dependence of upper and lower bounds of flow rate on electric field for continuous jet operation. ....	56
<b>Figure 4.10</b> Instantaneous fiber current at different flow rates operating at 15 kV electric field: (a) 1 $\mu\text{L}/\text{min}$ , (b) 5 $\mu\text{L}/\text{min}$ (inset pictures show intermittent jet ejection), (c) 10 $\mu\text{L}/\text{min}$ , (d) 12 $\mu\text{L}/\text{min}$ , (e) 15 $\mu\text{L}/\text{min}$ , and (f) 20 $\mu\text{L}/\text{min}$ . ....	58
<b>Figure 4.11</b> SEM micrographs of PAN nanofibers and corresponding diameter distribution for 15 kV and at various flow rates in the regime of continuous jet. (a) 20 $\mu\text{L}/\text{min}$ , (b) 17 $\mu\text{L}/\text{min}$ , (c) 15 $\mu\text{L}/\text{min}$ , and (d) 12 $\mu\text{L}/\text{min}$ . ....	60
<b>Figure 4.12</b> SEM micrographs of PAN nanofibers and corresponding diameter distribution for 15 kV and at various flow rates in the regime of discontinuous jet. (a) 10 $\mu\text{L}/\text{min}$ , and (b) 5 $\mu\text{L}/\text{min}$ . ....	61
<b>Figure 4.13</b> Variations in average nanofiber diameter as a function of flow rates for 15 kV and 18 kV electric fields. ....	62

<b>Figure 4.14</b> Effect of filament diameter on tensile stress-strain behavior of PAN nanofiber yarns made from continuous jet conditions. Toughness was calculated from the area under the stress-strain curve.....	64
<b>Figure 4.15</b> Stress-strain plots of PAN nanofiber yarns having similar filament diameter produced from continuous and discontinuous jet conditions. Toughness was calculated from the area under the stress-strain curve.....	65
<b>Figure 4.16</b> Variation of tensile strength of PAN nanofiber yarns as a function of flow rate at different electrospinning voltage. Filled: Continuous jet, Non-filled: Discontinuous jet.....	66
<b>Figure 4.17</b> Correlation between the average nanofiber diameter, $d$ and volumetric charge density, $(I/Q)^{-2/3}$ . (a) $y=mx$ fit, (b) $y=mx+c$ fit.....	68
<b>Figure 5.1</b> Schematics illustrating VIPS mechanism during electrospinning. ....	71
<b>Figure 5.2</b> Schematics illustrating WAXD spectra analysis for (a-b) as-spun and (c-d) annealed nanofibers. ....	78
<b>Figure 5.3</b> Ternary phase diagram of water/DMF/PAN system at (a) 20°C and (b) 40°C. Included in the diagrams are the binodal curves (dashed line) and spinodal curves (solid lines). Three regions in the diagrams are homogeneous (I), metastable (II), and unstable (III) regions. ....	81
<b>Figure 5.4</b> Surface morphology of as-spun PAN nanofibers electrospun at 20°C under various RH conditions. ....	84
<b>Figure 5.5</b> Surface morphology of as-spun PAN nanofibers electrospun at 40°C under (a) 30% RH and (b) 40% RH. ....	86
<b>Figure 5.6</b> Surface morphology of annealed PAN nanofibers electrospun at 20°C under various RH conditions. ....	87
<b>Figure 5.7</b> Cross-sectional micrographs of as-spun PAN nanofibers electrospun under various environmental conditions.....	88
<b>Figure 5.8</b> Cross-sectional micrographs of annealed PAN nanofibers electrospun at 20°C under various RH conditions.....	90
<b>Figure 5.9</b> Surface morphology (at low magnification) of as-spun PAN nanofibers electrospun at 20°C (a-f) and 40°C (g, h). Circles in (a): beads.....	90
<b>Figure 5.10</b> (a) Surface characteristics of large beads formed during electrospinning of 10% PAN/DMF solution at 20°C and 14% RH. (b) Possible composition paths for fibers (arrow 1) and beads (arrow 2) shown in (a). Dashed line: binodal curve, solid	

line: spinodal curves. I, II, and III are indicating homogeneous, metastable, and unstable regions, respectively. ....	92
<b>Figure 5.11</b> Influence of RH, temperature and annealing on the average nanofiber diameter of nanofibers electrospun from 10% PAN/DMF solution. ....	94
<b>Figure 5.12</b> Influence of RH on volumetric charge density of electrospinning jet. ....	95
<b>Figure 5.13</b> A graphical representation of difference between expected nanofiber diameter based on volumetric charged density (shown by straight line) and experimental diameter. ....	97
<b>Figure 5.14</b> Representative stress-strain curves for PAN nanofiber yarns electrospun at (a) 20°C and (b) 40°C under various RH conditions. ....	98
<b>Figure 5.15</b> Integrated WAXD plots and calculated percentage crystallinity of as-spun PAN nanofiber yarns electrospun at (a) 40°C-30% RH, (b) 20°C-22% RH, (c) 20°C-30% RH, and (d) 20°C-60% RH. Intensity profiles of integrated scans are shifted upward for clear comparison. ....	100
<b>Figure 5.16</b> Effect of annealing on tensile strength and strain at break for electrospun PAN nanofiber yarns produced at 20°C under various RH conditions. Numbers showing on histograms are percentage change in strength and strain at break due to annealing. ....	101
<b>Figure 5.17</b> Integrated WAXD plots and calculated percentage crystallinity of annealed PAN nanofiber yarns electrospun at 20°C and various RH conditions. Intensity profiles of integrated scans are shifted upward for clear comparison. ....	102
<b>Figure 6.1</b> Cyclization reaction (I- intramolecular, II- intermolecular).....	107
<b>Figure 6.2</b> Oxidation reaction (I- initial PAN, II- cyclized PAN). ....	108
<b>Figure 6.3</b> Dehydrogenation reaction (I-initial PAN, II-cyclized PAN). ....	108
<b>Figure 6.4</b> Cross-linking reaction. ....	109
<b>Figure 6.5</b> Volatile byproducts produced during stabilization of PAN homopolymer [165]. ....	110
<b>Figure 6.6</b> Effect of co-monomer on stabilization of PAN [165]. ....	111
<b>Figure 7.1</b> Exothermic heat evolution during DSC runs of electrospun PAN nanofibers in different gas environments at 5°C/min heating rates. ....	117

<b>Figure 7.2</b> Weight loss during TGA runs of electrospun PAN nanofibers in different gas environments at 5°C/min heating rates. (a) in nitrogen, (b) sample ‘a’ rerun in air, (c) in air only, (d) derivative of plot ‘a’, and (e) derivative of plot ‘c’.	118
<b>Figure 7.3</b> DSC plots of electrospun PAN nanofibers in different gas environments at different heating rates. (a) in air, (b) in nitrogen, and (c) rerun in air after running in nitrogen.	119
<b>Figure 7.4</b> Plots according to (a) Kissinger’s method and (b) Ozawa’s method. A. PAN nanofiber in air, B. cyclization peak of PAN nanofibers in nitrogen, C and D. oxidation and crosslinking peak of PAN nanofiber rerun in air after running in nitrogen, respectively.	122
<b>Figure 7.5</b> Change in PAN nanofiber yarn length under a tension of 0.5 MPa in air at a heating rate of 5°C/min.	125
<b>Figure 7.6</b> Reaction shrinkage behavior of PAN nanofiber yarn isothermally stabilized at various final temperatures under a tension of 0.5 MPa in air. (a) Shrinkage along with temperature profile, and (b) derivative of strain. Heating rate was 5°C/min.	127
<b>Figure 7.7</b> (a) Curve fitting of the shrinkage of PAN nanofiber yarn isothermally stabilized in air at various final temperature after heating at 5°C/min. (b) An example of curve fitting showing the fast decay (radical cyclization) and the slow decay (ionic cyclization).	129
<b>Figure 7.8</b> Arrhenius plots of parameters $k_1$ and $k_2$ .	130
<b>Figure 7.9</b> Change in storage modulus, loss modulus, and $\tan(\delta)$ during stabilization of PAN nanofiber yarn in air at a heating rate of 5°C/min.	131
<b>Figure 7.10</b> Dynamic mechanical behavior of PAN nanofiber yarn isothermally stabilized in air at various final temperatures after heating at 5°C/min. (a) Storage modulus, and (b) loss modulus.	132
<b>Figure 8.1</b> A schematic of cross-sectional view of sample arrangement inside the furnace. Insets are showing gas flow direction during vacuum (a) – purge (b) cycles.	135
<b>Figure 8.2</b> A schematic of paper window frames for tensile test of carbonized yarn. (a) Old design, (b) new design (d) new design modified for clamp geometry.	137
<b>Figure 8.3</b> Finite element analysis of the tensile test window frames. (a) old design, (b) new design.	138
<b>Figure 8.4</b> A photograph of few paper window frames.	139

**Figure 8.5** WAXD pattern of PAN precursor nanofiber yarn and nanofiber yarns isothermally stabilized at 260°C in air for various times. .... 140

**Figure 8.6** Representative tensile stress-strain curves of carbonized nanofiber yarns after stabilization at 260°C for various times. .... 142

**Figure 8.7** Representative tensile stress-strain curves of carbonized nanofiber yarns after constant length stabilization at 260°C for various times..... 143

**Figure 8.8** Morphology of yarns stabilized at constant length at 260°C for (a) 120 min, (b) 150 min, and (c) 180 min, and morphology of yarns showed (d) in a and (e) in c after carbonization. Arrows showing the defects on the surface..... 145

## ABSTRACT

Carbon nanofibers produced by electrospinning brings many advantages over carbon fibers made from conventional spinning methods as they are expected to possess less structural defects, superior mechanical performance, and higher surface area per unit volume. In this dissertation, an electrospinning setup is developed to fabricate aligned nanofibrous yarns from polyacrylonitrile (PAN) polymer using a rotating circular disk. The PAN-dimethylformamide (DMF) solution is fed using a vertical syringe, and nanofibers are collected from the grounded copper foil (width 1.27 cm) glued on the surface of a 25 cm diameter plastic disc. Various process parameters such as applied voltage, flow rate, and rotational speed are investigated. The alignment of the nanofibers is found to improve with increasing the rotation of the circular disc. The influence of electric field and flow rate on the fiber diameter and tensile properties of nanofibrous yarns is correlated with the Taylor cone half-angle at the tip of the needle and the fiber current. It is observed that a set of electric field and flow rate conditions favor producing thinnest, strongest, and toughest nanofibers. Other conditions may lead to instability of the Taylor cone, and as a result, discontinuous jet, larger diameter fiber, and lower mechanical properties are observed. A simple dynamic whipping model is adopted to correlate the fiber diameter with volumetric charge density and is found to be excellent validating the experimental results.

The influence of relative humidity (RH) and temperature on the morphology, structure, and mechanical properties of nanofibers is also investigated. It is observed that fibers show smooth surface and solid core to irregular surface and porous core depending on



the RH and temperature. The resulting morphology is explained by the means of ternary phase diagram of water/DMF/PAN. At higher RH conditions, the water diffusion into the polymer-solution jet brings thermodynamic instability into the system leading to separation of two phases such as polymer-rich phase and polymer-lean phase, where the later contributes to the rough surface and porosity of the structure. Higher process temperature leads to porous morphology at higher RH owing to larger miscibility area in the ternary phase diagram. It is found that the tensile properties of nanofibrous yarns depend mostly on the amount of porosity, although both diameter and crystallinity play important role. Annealing is found to alleviate surface roughness, reduce internal porosity, and improve mechanical performance of porous nanofibers.

Various stabilization reactions of electrospun PAN nanofibers such as cyclization, oxidation, dehydrogenation, and crosslinking are studied by in-situ characterization techniques using differential scanning calorimetry (DSC) and thermal gravimetric analysis (TGA). In-situ shrinkage of the PAN nanofiber yarn is monitored to study the extent of the cyclization reaction, while the crosslinking reaction is evaluated from the dynamic mechanical analysis (DMA). It is found that complete cyclization occurs at 260°C for 189 minutes, while the crosslinking reaction becomes prominent after 132 minutes. Wide angle X-ray diffraction of the stabilized yarns and tensile property of the carbonized yarns reveal that the optimum stabilization time should be in between 132 and 189 minutes. It is also found that application of tension load during stabilization helps to improve the properties of carbonized yarn; however the tension load should be controlled to avoid any defects in the structure.

## **Chapter 1: INTRODUCTION**

The increasing demands on nanotechnology in every aspect of modern manufacturing lead to pioneering scientific research. The reduction of particle size from micrometers to nanometers brings several amazing characteristics such as high surface area, high surface energy, superior strength, and stiffness. Electrospun carbon nanofibers (ECNFs) are considered as one dimensional (1-D) form of carbon. However, there are other types of 1-D carbon materials such as carbon fibers, vapor grown carbon fibers and nanofibers, and carbon nanotubes, which are closely related to ECNFs. Thus, it is important to know those 1-D carbon materials in terms of structures, processing, and properties along with their current technological challenges before addressing the advantages associated with ECNFs.

### **1.1 Carbon Fibers**

Carbon fibers (CFs) can be defined as 1-D filamentary form of carbon, in which carbon atoms are bonded together in microscopic crystals that are somewhat aligned parallel to the longitudinal axis of the fiber. The alignment of these crystals makes the fiber very strong for its size, compared to other traditional materials made for reinforcement. The diameters of single carbon fibers are between 4-10  $\mu\text{m}$ , and their aspect ratio (length/diameter) is greater than 100. They possess high strengths (3-7 GPa), high moduli (200-500 GPa), and low densities (1.75-2.00 g/cc). Their high specific strength and stiffness combined with retention of properties at high temperature have made them

the materials of choice for high performance composite structures in aerospace, automotive, structural, sporting goods, and many other industries [1].

The history of carbon fiber dates back to late 1800s when Sir J. Swan in the UK and Thomas Edison in the USA, used carbon fibers as filament materials in their incandescent light bulb experiments. They found that cellulose based materials such as cotton and bamboo fibers can be converted to carbon fibers by treating them in the absence of air in a heated gas furnace. Carbon fibers' considerable tolerance to heat made them ideal for conducting electricity. However, with time carbon fibers were replaced with more robust tungsten filaments in light bulb applications, and consequently the research and development of carbon fibers vanished at that early time. It was late 1950s, shortly after World War II, when carbon fibers again became important due to the aggressive demand of light weight but strong materials from aircraft industries [2]. In 1958, Roger Bacon created first high-performance carbon fibers at the Union Carbide Parma Technical Center by heating strands of rayon until they carbonized [3]. The carbon content in the resulting fibers was only about 20%, and as a result the fibers had lower strength and stiffness. In the early 1960s, a process was developed in Japan to produce carbon fibers, using polyacrylonitrile (PAN) as the raw material, which contained about 55% carbon and had much better properties [1]. In 1963, the pitch-derived carbon fibers containing almost 85% carbon, with high-modulus, were invented [4].

Since the required temperature and pressure to prepare a carbon fiber from the liquid phase is at the triple point ( $T=4100$  K,  $P=123$  bar), it would be near to impossible to

prepare carbon fibers from the melt under industrial processing conditions [5]. Carbon fibers are therefore prepared from organic precursors. There are many precursor materials that can be used to produce carbon fibers, but only two are considered suitable for commercial processes: pitch (coal tar and petroleum products) and PAN. Although the processing of carbon fibers from different precursors requires different conditions to obtain satisfactory quality end products, the essential features of the processing paths are similar and involve (a) spinning (and stretching), (b) a stabilizing heat treatment usually in air (at 200°C ~ 400°C) to prevent the precursor fibers from melting or fusing together in the subsequent heat treatment, (c) a carbonizing heat treatment (at 700°C ~ 1700°C) in oxygen free environment to drive off the majority of non-carbon elements, and (d) an optional high temperature ( up to 3000°C) treatment, called graphitization, to improve the stiffness of the fiber [1, 5]. After carbonizing and/or graphitizing, additional surface treatment and epoxy coating (also called sizing) are applied to give the fibers better bonding properties with the epoxies or other materials used in composites, as well as to protect the fibers from damage during winding and weaving [5]. A schematic representation of carbon fiber production from two different precursors is shown in Figure 1.1. Pitch- and PAN-based CFs have properties that suit different applications. PAN-based CFs are primarily used for structural reinforcement because of their high tensile strength, while pitch-based CFs offer higher modulus and higher thermal and electrical conductivities [1]. Figure 1.2 shows scanning electron microscopy images along with schematic structural models of a high strength PAN-based and a mesophase pitch-based CFs. The PAN-based CFs consist of  $sp^2$  carbon

structural units preferentially aligned with the carbon hexagonal segments parallel to the fiber axis which is responsible for their high strength. On the other hand, well-aligned graphitic layers arranged nearly parallel to the fiber axis are responsible for the high modulus and stiffness of the mesophase pitch-based CFs.

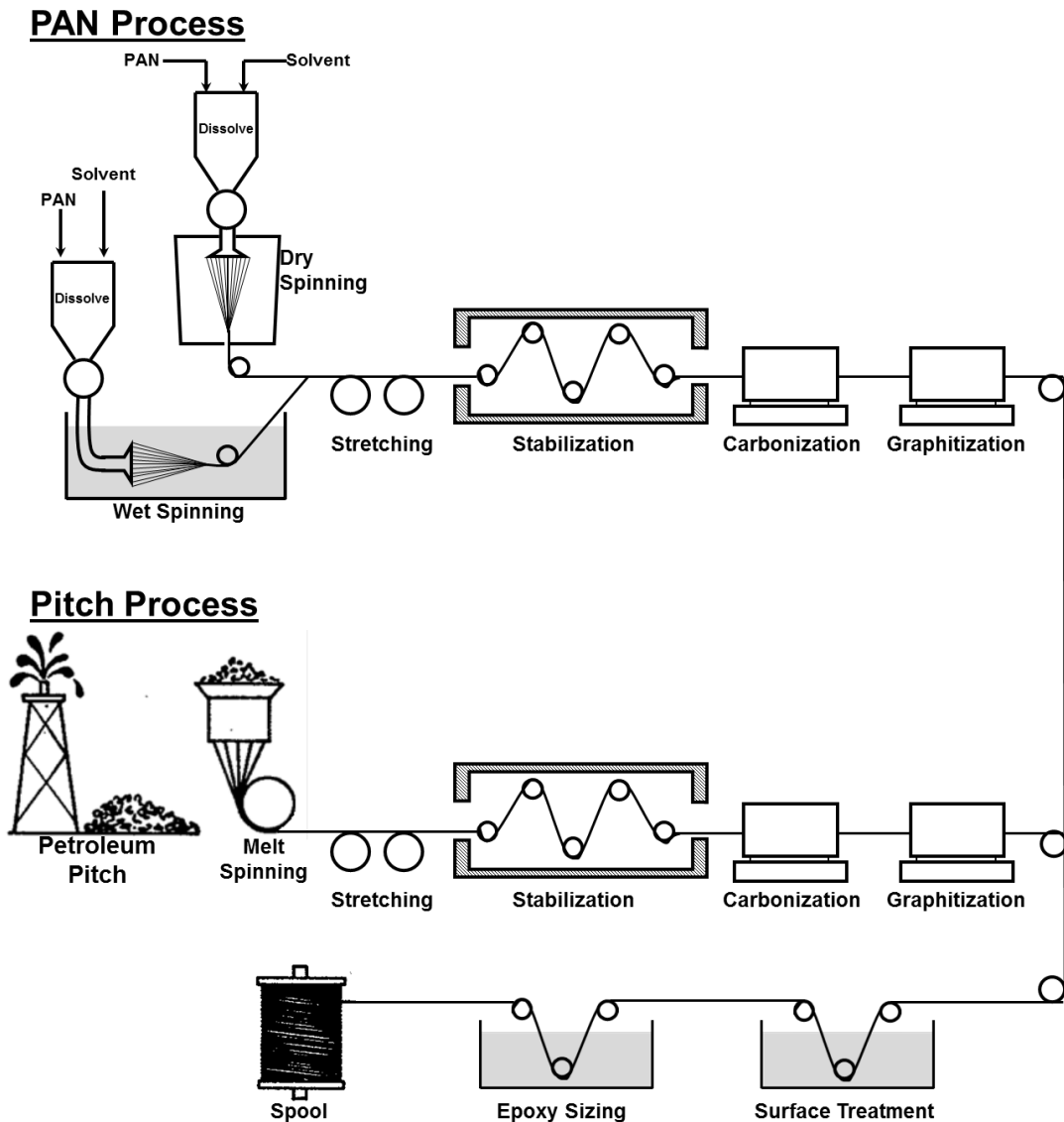


**Figure 1.1** Schematic of CF productions from PAN and pitch precursors.

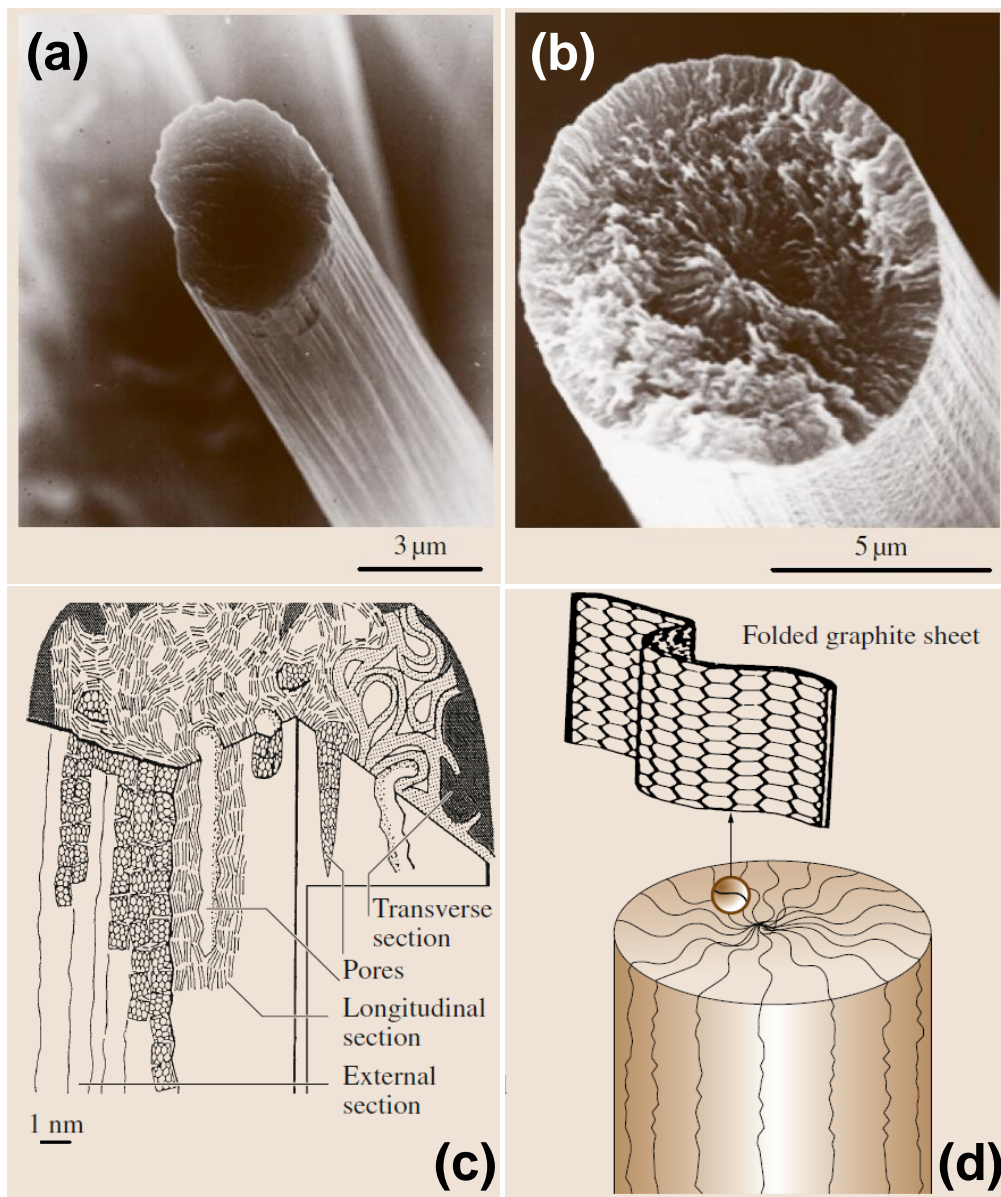


**Figure 1.2** SEM micrographs (top) and corresponding structural models (bottom) of PAN-based (a, c) and mesophase pitch-based (b, d) CFs [6].

## **1.2 Challenges with Conventional Spinning Methods for Further Improving the Mechanical Strength of Carbon Fibers**

Shortly after the discovery of CF production, by late 1970s, the tensile strength of AS4 carbon fiber made by Hexcel Corporation reached 4.6 GPa. However, after almost 4 decades of research, the strongest carbon fibers that can be produced today have a tensile strength of only 7.02 GPa (e.g. Toray T1000® ), merely 4% of the theoretical value of over 180 GPa [7]. Numerous research endeavors have revealed that (1) the amount, size, and distribution of structural imperfections in carbon fibers primarily determine the strength; and (2) many types of structural imperfections in precursor fibers are likely to be retained by the resulting carbon fibers [8-10]. Hence, the fundamental approach to further improve the strength of carbon fibers is to reduce numerous types of structural imperfections including (1) surface defects such as nicks, cracks, punctures, as well as diametrical bulges, (2) bulk defects such as large cavities, small holes, cracks/flaws induced by internal stress, refractory inclusions, as well as other voids, entanglements, and/or dis-ordered structures, and (3) structural inhomogeneities such as sheath–core structures. A schematic representation of various types of structural imperfections in CFs is shown in Figure 1.3. Research efforts have also indicated that the significant improvement on mechanical strength of carbon fibers is unlikely to be achieved with current PAN co-polymer fibers as precursors [9]. This is because the degree of structural perfection of the current precursor fibers is limited by the conventional spinning methods such as wet spinning and air gap spinning (also known as “dry-jet wet spinning”) [9]. During spinning the rapid removal of solvent

from jets in the coagulation bath introduces large amount of defects. Although post-spinning stretching can substantially improve the macromolecular orientation, the reduction of these defects is limited; consequently, voids/flaws with sizes ranging from a few to tens of nanometers are frequently observed in precursor fibers and in the resulting carbon fibers. The existence of these defects is an important reason that the strength of presently produced carbon fibers only reaches a small percentage of theoretically predicted value. Additionally, the large diameter of the precursor fibers is also responsible for the formation of structural inhomogeneities (particularly sheath–core structures) during stabilization and carbonization [8]. It has been revealed that the strength of carbon fibers generally increases with decrease of fiber diameter. This is well-known as the “Size Effect”; for example, the Toray T300® carbon fibers with diameters of  $\sim 7 \mu\text{m}$  have the tensile strength of  $\sim 3.5 \text{ GPa}$ , whereas the Toray T1000® carbon fibers with diameters of  $\sim 5 \mu\text{m}$  have the tensile strength of  $\sim 7 \text{ GPa}$ . Nevertheless, the conventional spinning methods make it difficult, if not impossible, to prepare the precursor fibers with diameters that are orders of magnitude smaller than  $10 \mu\text{m}$ .



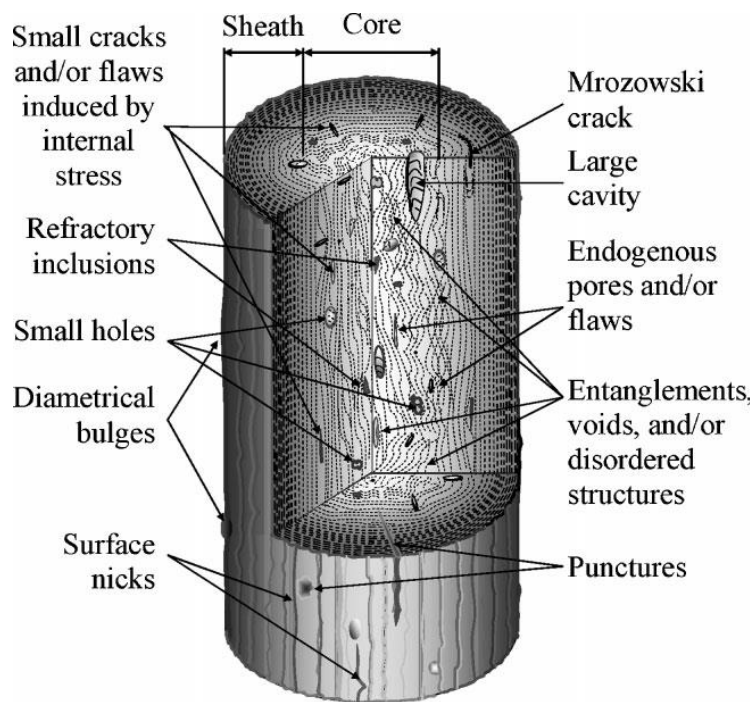


**Figure 1.3** Schematic representation of various types of structural imperfections in CFs [8].

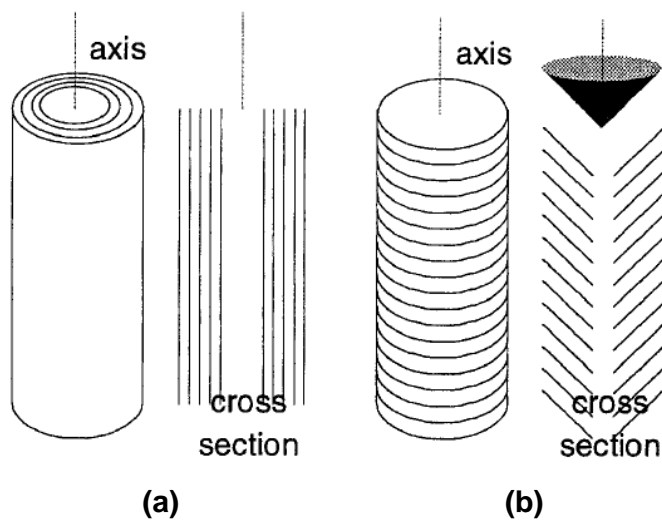


**Figure 1.4** Schematic of (a) platelet and (b) staked cup type VGCFs and VGCNFs [11].

### 1.3 Vapor Grown Carbon Fibers and Nanofibers

Vapor grown carbon fibers (VGCFs) and vapor grown carbon nanofibers (VGCNFs) are cylindrical carbon nanostructures with graphene layers arranged as staked cups or platelets (Figure 1.4). The diameter of the fibers can vary from ~50 nm to several tens of  $\mu\text{m}$ . These fibers are synthesized by a somewhat different formation process than that used to produce PAN-based and mesophase pitch-based CFs. They are not prepared from a fibrous precursor, but rather by decomposing a hydrocarbon gas (methane, ethylene, acetylene, or benzene or ethanol vapor) on a metal catalyst at 500~1500°C [12]. The process is known as catalytic chemical vapor deposition (CCVD) or simply CVD. The process is performed by one of the two methods whereby fibers are grown either on a substrate or in a gas flow. In the method for growing fibers on a substrate, a catalyst (usually iron) is applied on a graphite or ceramic substrate by either spraying a suspension of fine catalyst powder in an organic solvent or spraying an catalyst containing solution or organic compound that would decompose to catalyst particles onto the substrate beforehand and then a mixture of hydrocarbon/hydrogen/helium is passed on the substrate. While in the method for growing fibers in a gas flow, the catalyst compound is directly mixed with the hydrocarbon gas beforehand or directly injected into the reactor. In all of the cases, a catalyst particle is trapped by a growing fiber, and eventually each fiber ends with a metal microcrystal cap. The schematic of two CVD methods are shown in Figure 1.5. The diameter and length of the fibers depend on the size of the catalyst particles and the treatment temperature. The strength

and modulus of VGCNF of  $\sim 150$  nm have been reported 3.34 GPa and 245 GPa, respectively [13].

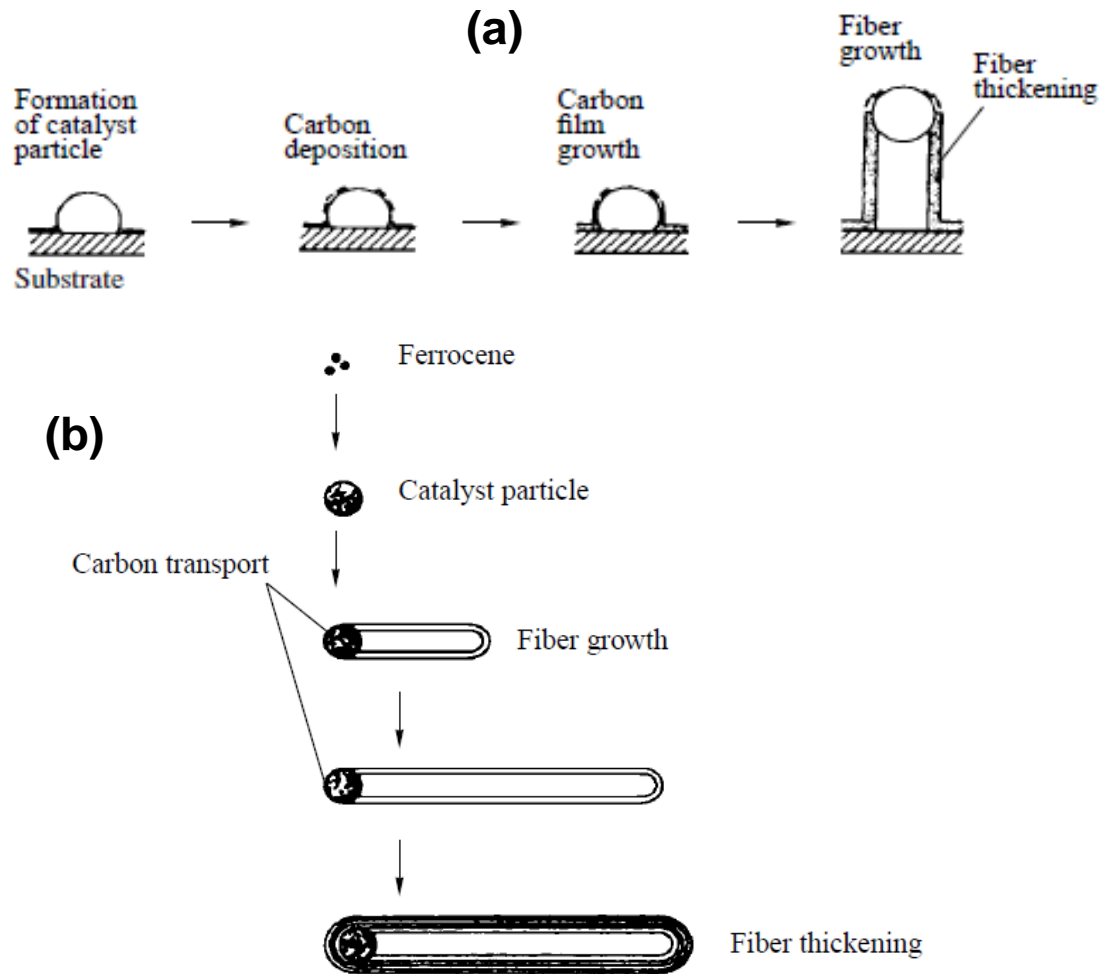


**Figure 1.5** Schematic of the growth of VGCFs and VGCNFs (a) on a substrate and (b) in a gas flow [12].

## 1.4 Carbon Nanotubes

Carbon nanotubes (CNTs) are another form of 1-D carbon materials and are considered as the strongest and stiffest materials yet to be discovered in terms of tensile strength and elastic modulus, up to 100 GPa and 1 TP, respectively [14]. CNTs can be defined as rolled up graphene sheets in hollow cylindrical form. One distinguishes single-walled CNTs (SWNTs), consisting of only one rolled-up layer of graphite with a diameter up to 3 nm, and multi-walled CNTs (MWNTs), consisting of several concentric interlinked graphite tubes with a diameter up to 100 nm (Figure 1.6) [15]. The roll up direction (i.e. chiral vector) determines different modifications of the structures which will then have different physical properties [16].

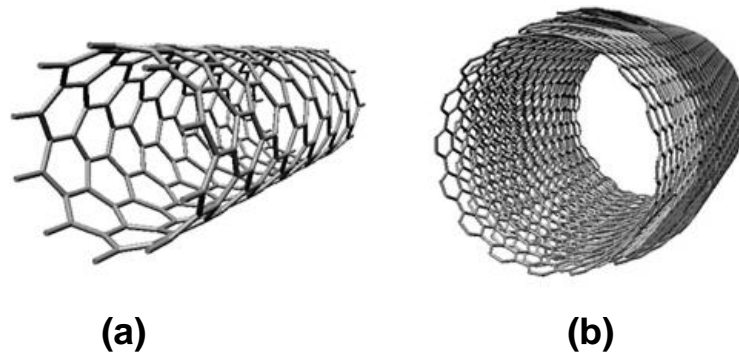


**Figure 1.6** Schematic showing (a) SWNT and (b) MWNT.

Three methods such as arc discharge, laser ablation of graphite and CVD are commonly used for the production of CNTs [17]. In the first two processes, graphite is combusted

electrically or by means of a laser, and the CNTs developing in the gaseous phase are separated, while CVD is similar to that employed for VGCNF production. All three methods (except arc discharge method in MWNTs production) require the use of metals (e.g. iron, cobalt, nickel) as catalysts [17]. The CVD process currently holds the greatest promise, since it allows the production of larger quantities of CNTs under more easily controllable conditions and at lower cost [18].

### **1.5 Current Challenges with VGCNFs and CNTs**

Although VGCNFs and CNTs possess unique mechanical, electrical, and thermal properties which are expected to result in revolutionary new materials and devices, there are many challenges to process them into applications. These nanomaterials, produced by synthetic bottom up methods, are discontinuous in nature which leads to difficulties with their alignment, assembly, and processing into application. Their inherent nature makes them to stick together in bundles which needs further processing to disperse them [19, 20]. Various techniques such as ultrasonication, high shear mixing, treating with surfactant etc. are used to disperse them, but none are end-all solutions [19-21]. Moreover, the carbon nanomaterials produced by bottom up methods are often coated with soot such as amorphous carbon, metal catalyst, and fullerenes. These unwanted materials need to be removed because they can interfere with the properties of the CNFs and CNTs. Several techniques such as oxidation, nitric acid reflux, HCl reflux, organic functionalization, filtration, mechanical purification, and chromatographic purification have been developed that separate the amorphous carbons and catalyst nanoparticles

from the CNFs and CNTs, however a significant amount of them are also destroyed during these purification processes [19, 21].

Researchers have fabricated CNT fibers through solid state spinning from CNT forest or reaction zone and wet spinning from CNT solution [22]. Although CNT fibers have exhibited higher specific modulus and specific strength than those of commercial carbon fibers, many challenges must be addressed before commercialization of CNT fibers. A few challenges include (a) synthesis of CNTs with high and consistent quality as well as controllable nano-structure, (b) scaling-up the synthesis of high-quality spinnable CNT arrays, and (c) effective transference of properties of individual CNTs to the micro- and macro-structural levels [23].

### **1.6 Electrospinning: An Innovative Technique to Produce Continuous Carbon Nanofiber with a High Degree of Morphological and Structural Perfection**

The rapidly developing electrospinning technology enables the production of continuous polymer nanofibers from polymer solutions or melts [24-26]. Unlike conventional spinning methods electrospinning utilizes electric forces to produce fibers. During electrospinning a high-voltage is applied to a viscous polymer solution or polymer melt at the tip of an electrode/needle. At sufficient voltage the electric force on the induced charges on the polymer liquid overcomes surface tension and a thin polymer jet is ejected [24, 25]. The charged jet is elongated and accelerated by the electric field, undergoes a variety of instabilities, dries, and is deposited on a substrate. PAN based co-polymer and Pitch can be used to prepare the precursor nanofibers by

using electrospinning technique which can be converted to CNFs by the processes of stabilization, carbonization, and/or graphitization as it is done for conventional microscale CFs [27, 28].

Electrospinning brings many advantages over the tradition spinning method of CF production. The crucial factors that determine the strength of CFs are the diameter, the size and distribution of the structural defects, the macromolecular orientation and crystalline structure, and the morphological and structural homogeneity [1, 8, 9]. The diameters of the electrospun nanofibers are ~300 nm, whereas the diameters of as-spun (before stretching) conventional fibers are tens of micrometers. During electrospinning solvent is removed through evaporation, while it is removed through coagulation in the conventional spinning methods. Evaporation causes fewer defects as compared to coagulation. Moreover, less number of defects would form during removal of solvent from much smaller diameter nanofibers. The conventional spun fibers have almost no macromolecular orientation before stretching, whereas in the as-electrospun nanofibers, the macromolecular chains are oriented due to the huge elongation (draw) rate involved in the electrospinning process, particularly during bending instability [29]. Therefore, it is envisaged that after undergoing a similar post-spinning stretching process, the stretched electrospun nanofibers will possess much higher degree of macromolecular orientation than the conventional spun fibers [30, 31]. For instance, Zong et al. found the molecular chains in the electrospun poly-L-lactic acid (PLLA) fibers to be highly oriented compared to the random-coil shape chains in the PLLA film [32]. Moreover, due to their much lower diameter (Figure 1.7a), the nanofibers prepared by

electrospinning are less likely to form structural inhomogeneities, particularly sheath/core structures during stabilization and carbonization [8, 33]. Furthermore, the bulk production cost incurred during carbon fiber production is due to the prolonged heating required for the thermal conversion of the precursor fibers into structural CFs [1, 34]. The heating time i.e. the production cost is expected to be reduced due to the lower diameter of the electrospun nanofibers.

Unlike VGCNFs and CNTs, which are produced by bottom up methods, the ECNFs are produced through top down manufacturing process, which results in low cost. The resulting ECNFs are often uniform (Figure 1.7b, c) and do not require expensive purification [26]. Unlike VGCNFs and CNTs, the electrospun nanofibers are continuous and also easy to align, assemble, and process for many applications.

Due to their small dimension, excellent physicochemical properties, and relatively low production cost, ECNFs are considered to be potential candidates for various applications ranging from multifunctional composites, materials for energy conversion and storage, catalysis support, sensor, adsorption/separation, to biomedical.



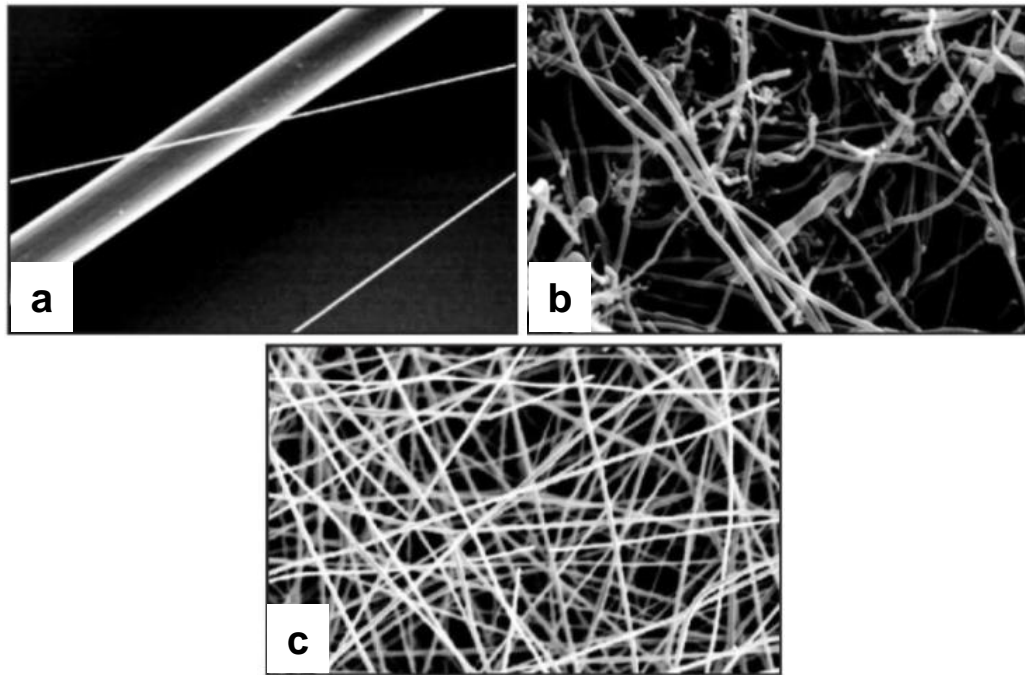


**Figure 1.7** (a) Comparison of CF and ECNF. Comparison of (b) VGCNFs and (c) ECNFs showing significantly better nanofiber uniformity and sample purity [26].

### 1.7 Fabrication of ECNFs from PAN Nanofibers

PAN homo- and co-polymers have been found to be the most suitable precursors for high performance CFs (compared to pitch, rayon, etc.) generally because of their higher melting point and greater carbon yield (>50% of the original precursor mass) [35-37]. PAN fiber is also preferred to be the precursor because of its faster rate in pyrolysis without changing its basic structure [38]. Currently, the PAN solution spinning process is the standard commercial method used for manufacturing of the majority of industrial CFs [39].

Similar as conventional carbon fiber production, PAN is the most often used precursor polymer for producing carbon nanofibers from electrospinning. CNFs have been successfully prepared from electrospun PAN nanofibers by a series of heat treatment steps in different environments at progressively increasing temperatures, as it is for conventional CFs [28].

### ***1.7.1 PAN***

Polyacrylonitrile (PAN) is a linear polymer containing approximately 68% carbon [40]. The commonly accepted chemical structure of PAN molecules is shown in Figure 1.8. It is generally believed that PAN forms relatively stiff, rod-like molecules due to the intramolecular dipole repulsion of its nitriles [41]. Due to these strong interactions, PAN is insoluble except in highly ionizing solvents and it has a high melting point. Also, these strong dipole-dipole interactions prevent rearrangements necessary for the development of crystallinity and cause shrinkage of the fiber during heat treatment. Shrinkage is a disadvantage to carbon fiber manufacture because it disturbs the orientation of the fiber and produces carbon fibers with poor mechanical properties. If shrinkage is prevented, by stretching during stabilization, carbon fibers with improved mechanical properties can be prepared [42].

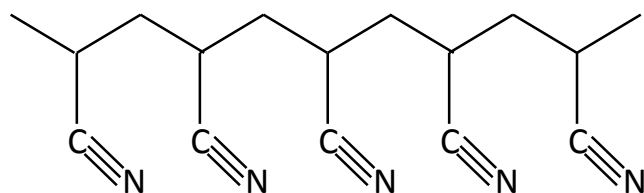


**Figure 1.8** Schematic figure of PAN molecule.

Two theories have been proposed to illustrate the crystal structure of PAN fibers. One group describes the structure of PAN as a single-phase structure with paracrystalline order [43], while another group believes in a two-phase structure of PAN with distinct pseudocrystalline (ordered) and amorphous (disordered) phases [44]. The paracrystal theory describes PAN structures with ideal crystal positions and position derivations, thus, it can describe all XRD patterns from perfect crystals to totally amorphous materials, like gas. The two phase structure theory proposes that PAN structures contain both crystal regions (ordered) and amorphous regions (disordered). Figure 1.9a shows how PAN molecules form an irregular helix, and Figure 1.9b shows how these helices pack into laterally ordered domains or “crystals”.

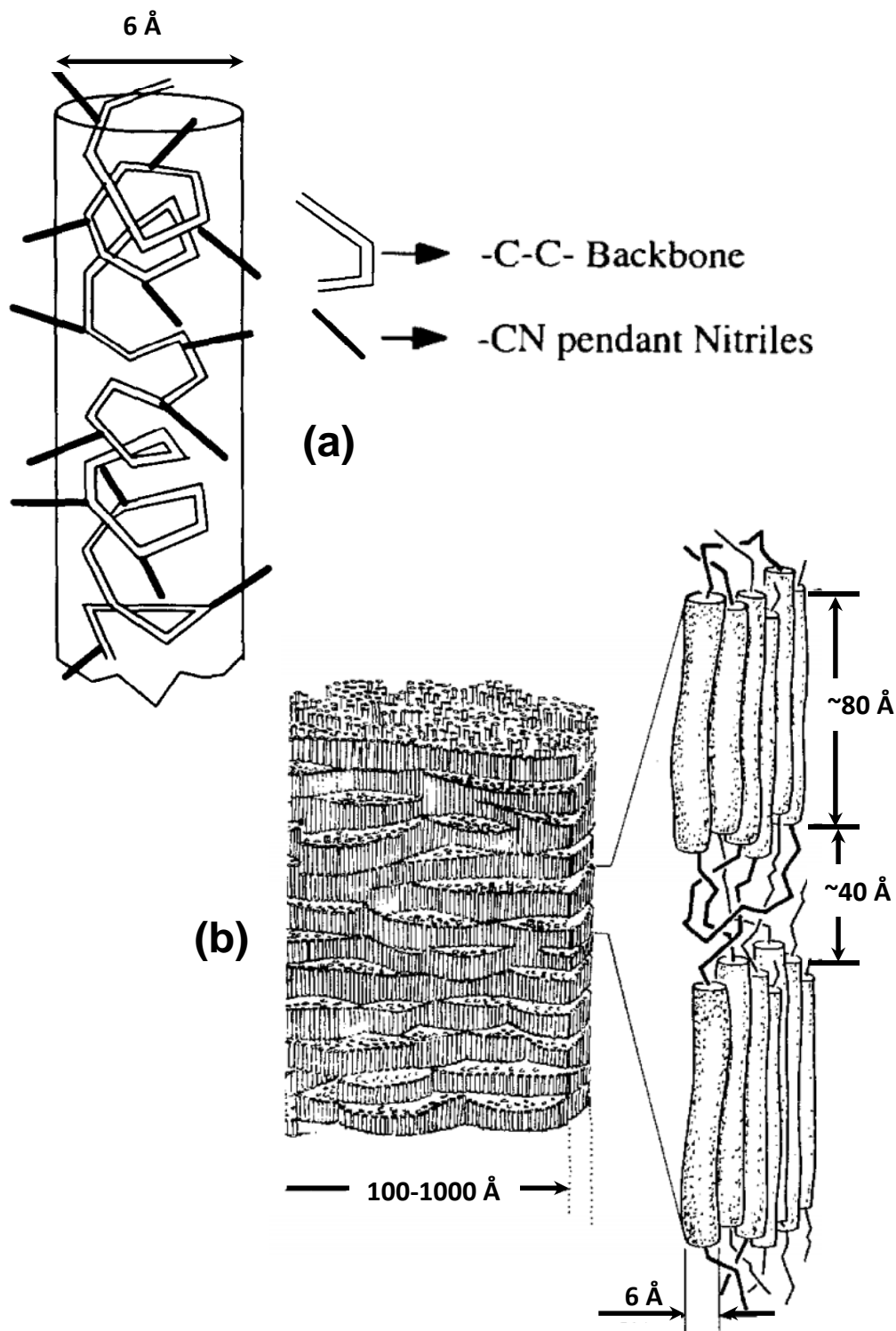


**Figure 1.9** (a) Helical structure of PAN chains. (b) Morphological model of PAN fiber showing ordered and disordered regions [44].

PAN is soluble in polar solvents like DMF, DMSO, DMAc, dimethylsulfone, tetramethylsulfide and aqueous solutions of ethylene carbonate, as well as some mineral salts [45]. PAN forms saturated solution with 25% dissolved in DMF at 50°C, which is high solubility compared to other solvents.

### ***1.7.2 Heat Treatment of electrospun PAN Nanofiber***

In general, the heat treatment process of electrospun PAN nanofibers to convert into ECNFs can be divided into three stages by processing temperatures and gas environments which are as follows [28]:

i) Stabilization, which forms ladder structure to enable them to undergo subsequent processing at higher temperatures and increases carbon yield. The temperature range of this step is from 200°C to 400°C, and an oxidative gas, typically air, is used as the environment.

ii) Carbonization, which eliminates most of the noncarbon elements from the fiber and converts the stabilized fibers into carbon fibers. Carbonization is conducted in an inert atmosphere at temperatures ranging from 700°C to 1700°C. The ladder polymer formed during stabilization further cross-links and forms a turbo-static carbon structure in this stage.

iii) Further heat up to 3000°C to improve the orientation of the basal planes and the stiffness of the fibers, called graphitization.

## **1.8 Scope of the Work**

Although ECNFs have shown great promise in non-mechanical applications, they have not made their way to composite reinforcement applications due to their low mechanical strength. The mechanical properties of ECNFs depend on the quality of the as spun nanofibers as well as the optimization of the heat treatment conditions. Among various steps of the heat treatment, stabilization is considered as most influential step as many complex physical and chemical changes occur in this step. Therefore, the focus of this dissertation research has been on understanding various electrospinning process parameters to fabricate high quality electrospun nanofibers and understanding the mechanisms of various chemical and physical changes during stabilization.

This dissertation work has been divided into two parts. In PART I, a thorough literature review of the influence of various process parameters on the morphology, diameter, and structure of the electrospun nanofibers has been provided, and then based on the previous research findings few parameters have been selected for further investigation. For composite reinforcement application the nanofibers should be aligned and collected in the form of yarn, therefore an electrospinning set up has also been developed to produce aligned electrospun nanofiber yarns. In PART II, various in situ characterization techniques have been utilized to monitor various physical and chemical changes during stabilization of the as spun nanofibers. The influence of the various stabilization conditions on the mechanical property of the final ECNF yarns has also been investigated.

Pointed research questions have been posted at the end of chapter 2 and chapter 6 for part 1 and part 2, respectively. All of the works have been performed to obtain specific answers to these questions.

# **PART I: INVESTIGATION OF THE GOVERNING PARAMETERS IN THE ELECTROSPINNING OF POLYACRYLONITRILE NANOFIBERS**

## **Chapter 2: ELECTROSPINNING**

### **2.1 History**

The utilization of electrostatic forces to deform materials in liquid state was first reported by William Gilbert, an English physician, in the sixteenth century [46]. When he brought a suitably electrically charged piece of rubbed amber near a droplet of water he observed the formation of a cone and then small droplets were ejected from the tip of the cone. In 1745, the German scientist Bose wrote about his observations of liquids with an electrical potential applied to a glass capillary. In the 19th century, the development and understanding of the science and technology of electricity generation had reached a sufficient level to provide inductive generation of high voltages. Throughout the 20th century, there have been a number of studies [47-49] focused on electrohydrodynamic atomization (also called electrospraying) of low viscous liquids. In electrospray, small droplets of particles are formed as a result of the varicose breakup of the electrified jet. Electrospinning is an extension of this technology applied to higher viscosity fluids. The process of electrospinning was first patented [50] by J.F Cooley in February 1902. Further developments toward commercialization were made by Anton Formhals, and described in a sequence of patents [51-54] from 1934 to 1944 for the fabrication of textile yarns. His spinning process consisted of a movable thread collecting device to collect threads in a stretched condition, like that of a spinning drum



in conventional spinning. Meanwhile, electrospinning from a melt rather than a solution was patented [55] by C. L. Norton in 1936 using an air blast to assist fiber formation. However, none of these early patents could be finalized by actual industrial application, likely because of the lack of characterization equipment suitable to investigate the sub-micron features of the physical processes involved and of the fibrous structures generated.

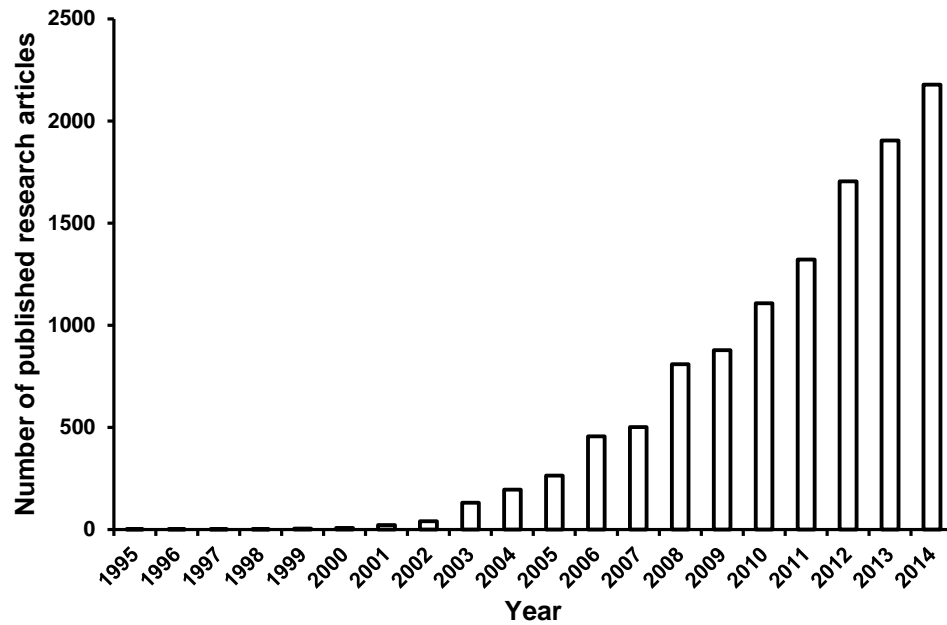


**Figure 2.1** Statistics of published research articles about electrospinning (Source: Web of Science Database, keyword: “electrospinning”).

In the 1960s, fundamental studies [49, 56, 57] on the jet forming process were initiated by Taylor. Taylor’s work contributed to electrospinning by mathematically modeling the shape of the cone formed by the fluid droplet under the effect of an electric field;

this characteristic droplet shape is now known as the “Taylor Cone”. In 1971, electrospun acrylic nanofibers with diameters ranging from 500 to 1100 nm were produced by Baumgarten [58]. However, it was not until 1990s that the great potential of electrospun nanofibers’ applications in various areas has been realized. Research on nanofibers gained a milestone with the work of Doshi and Reneker [24]. Since then, the number of publications about electrospinning has been increasing rapidly every year (Figure 2.1). To date, it is generally believed that nearly one hundred different polymers, mostly dissolved in solvents, have been successfully spun into ultrafine fibers using this technique. Although the electrospinning process has shown promising potential and has existed for several decades in the literature, the process has remained essentially unchanged and its understanding is still limited.

## **2.2 Fundamental Theory**

In a typical electrospinning system, a high-voltage is applied to a polymer solution or polymer melt at the tip of an electrode and at sufficient voltage the electrostatic repulsion force prevails over the surface tension of the solution and triggers the formation of a jet in the form of a Taylor cone at the end of the solution droplet [20, 59]. The polymer solution jet is expelled from the apex of the Taylor cone and accelerated toward the collector, which is usually grounded. The emitted charged jet usually travels few centimeters in a straight path due to a longitudinal stress caused by the external field. Then a lateral perturbation grows in response to the repulsive forces between adjacent elements of charge carried by the jet and initiates a whipping

instability resulting in enormous stretching of the jet and formation of nanofiber [20]. During the flight, the polymer solution jet also experiences solvent evaporation and eventually deposits onto the collector as solid (or mostly solid) nanofiber, as shown in Figure 2.2. The collector can be designed for producing nonwoven mats, random and aligned structures.

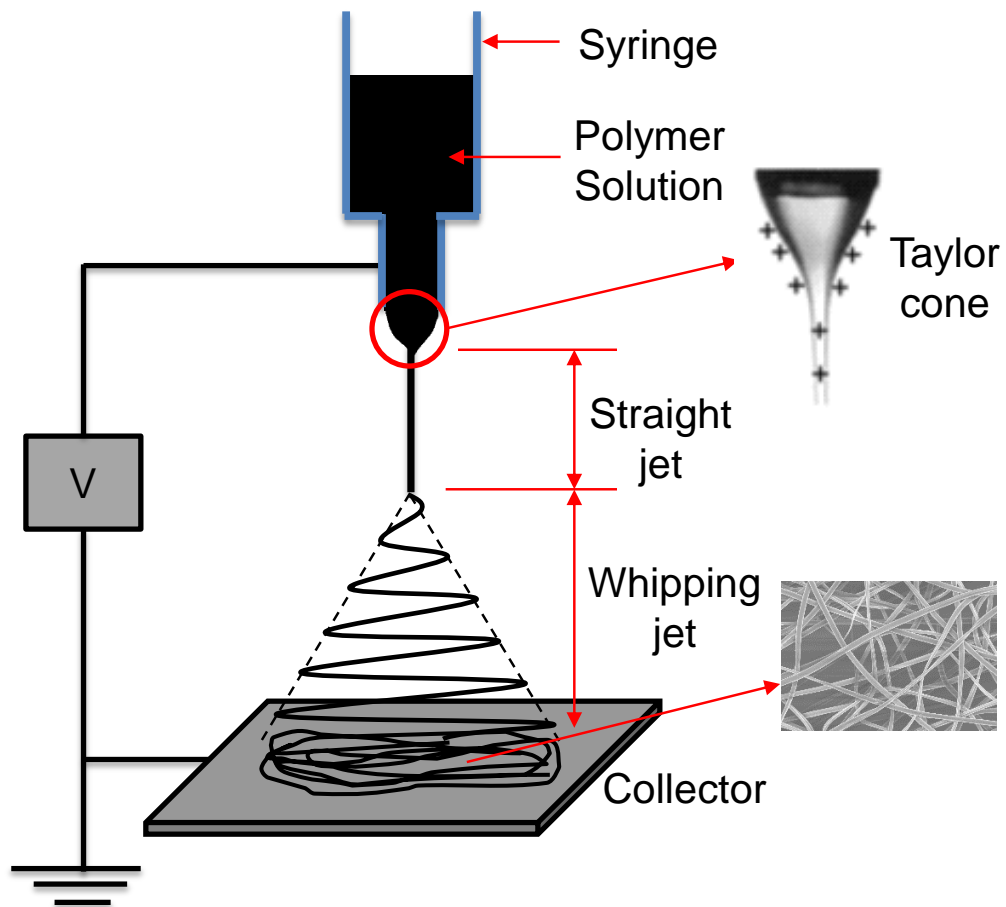


**Figure 2.2** A schematic representation of electrospinning technique.

### **2.3 Applications of Electrospun Nanofibers**

The simplicity of the fabrication process, the diversity of materials suitable for use with electrospinning, as well as the unique features such as large surface area and porous structure, associated with electrospun nanofibers; all make this technique and the resultant structures attractive for a broad variety of applications. The followings are some examples of their potential applications in various fields.

- Medical: Tissue engineering scaffolds [60, 61], blood vessels, muscles, skins [62], wound healing, drug delivery [61, 63] and release control [64], medical textile materials [65].
- Environmental protection: Filtration [66, 67], metal ion adsorption and recovery [68], carbon capture.
- Protective materials: Sound absorption materials [[69], chemical and biological protective clothing [70].
- Catalysis: Chemical catalysts [71], photocatalysis [72], enzymes [73].
- Energy harvest and storage: Solar cells [74], fuel cells [75], mechanical energy harvesters [76], lithium ion batteries [77], supercapacitors [78], hydrogen storage [79], photovoltaic device [80].
- Electronic devices: Field effect transistor [81], chemical sensors [82].

## **2.4 Electrospinning Processing Parameters**

Despite the apparent simplicity of the electrospinning process, the process itself is quite complicated owing to many parameters that influence the morphology, structure, and diameter of electrospun fibers. The processing parameters include: a) the intrinsic properties of the solution such as polymer concentration [83, 84], molecular weight [83, 85], conductivity [86], and surface tension [87]; b) the operational conditions such as electrospinning voltage [88, 89], distance between spinneret and collector [88, 89], and solution flow rate [90]; and c) the environmental conditions such as relative humidity (RH) and temperature [91, 92]. However, the effect of some of the solution properties can be difficult to isolate since one parameter can generally affect other properties. For example, changing the viscosity of the solution can also change the conductivity [93]. Investigation of the influence of these parameters on electrospinning process is important to control the morphology and tailoring the properties of the electrospun fibers.

### ***2.4.1 Solution Parameters***

Among all the parameters, polymer concentration has been mostly investigated and also found to be the main factor for controlling fiber diameter and morphology. At low polymer concentration, beading and droplets on the fiber surface have been reported [94, 95]; the process under these conditions is predominantly characterized as electro spraying [96]. The increasing of the polymer concentration to a critical point leads to uniform and bead free fibers [83, 97]. An example can be seen in Figure 2.3 for

electrospun Polystyrene (PS) fibers [98]. Moreover, the diameter of fibers from high concentration (30% by wt.) was one order of magnitude larger than that of fibers from low concentration (5% by wt.), which indicates significant increase of fiber diameter due to the concentration increase. Similar results have also been found for other polymer fibers such as polyurethane (PU), polylactide (PLA), polyvinyl chloride (PVC), polyamide6 (PA6), and chitosan (CS) [32, 85, 96, 99-100]. Therefore, there seems to be a general agreement that the increase in the polymer concentration leads to increase in the fiber diameter due to higher number of entanglements between polymer chains, which oppose jet stretching under electric field.

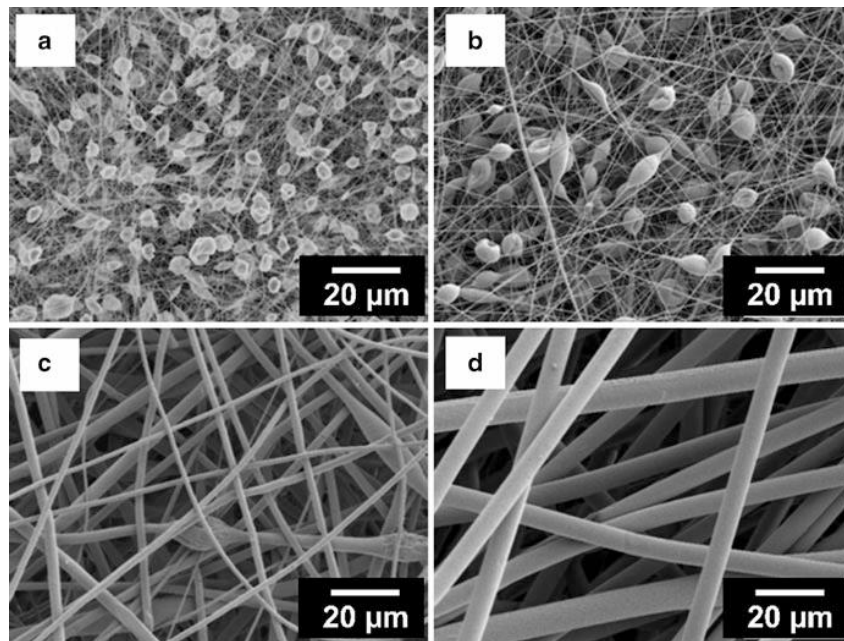


**Figure 2.3** SEM images of electrospun PS fibers from various concentrations of (a) 5 wt%, (b) 10 wt%, (c) 20 wt%, and (d) 30 wt% [98].

Conductivity [101, 102] of polymer solution has also been reported as influential parameters for electrospinning process. For an electrospinning process to be initiated, the polymer solution must gain sufficient charges so that the generated repulsive forces within the solution are able to overcome the surface tension of the solution. Subsequent stretching of the electrospinning jet also depends on the ability of the solution to carry charges. Thus, the increase of electrical conductivity of the solution results in significant decrease in diameter. Solution with low conductivity results in insufficient elongation and often beads are formed.

As the solution jet accelerates from the tip of the source to the collector, the solution is stretched, while surface tension of the solution may cause the solution to break up and form beads. Therefore, bead formation can be minimized by lowering surface tension of the solution [103, 104].

#### ***2.4.2 Operational Parameters***

Although the effects of solution parameters on diameter of the electrospun nanofiber are well established, the influence of the operational conditions such as electrospinning voltage and flow rate shows inconsistent results. Some studies showed that the diameter of the fiber decreased with increasing electrospinning voltage or field strength [18, 105, 106], while others showed opposite trend [32, 90, 107]. In some studies, the relationship between nanofiber diameter and field strength was found ambiguous. For example, Yordem et al. [108] found that depending on the solution concentration and needle to collector distance nanofiber diameter can increase, decrease, and initial decrease

followed by increase with increasing electrospinning voltage. Careful observation of the data reported by Buchko et al. [109] revealed that the average diameter of electrospun nylon nanofibers decreased to a minimum value and then increased with increasing field strength. It is also noticed that the standard deviation was lower when the nanofiber diameter reached to the minimum value. Similarly, several authors showed that the diameter of the nanofiber increased with increasing the flow rate [107, 110], while others found no significant influence of the flow rate [58, 111].

The effect of collector distance has not been reported to be significant [85, 112], although a minimum distance is required to ensure that the electrospun fibers have sufficient time to dry before reaching the collector [112].

#### ***2.4.3 Environmental Parameters***

Relative humidity (RH) has been found to affect the diameter of the fibers, and how it affects the diameter of fiber depends on the type of solvent is used. For water and acidic solvent, the diameter of electrospun fibers was found to decrease with the increase of RH, while opposite trend was observed for organic solvent. For instance, Tripatanasuwan et al. [113] and Cai et al. [114] observed for electrospun fibers from polyethylene oxide (PEO) aqueous solution that the fiber diameter decreased with increasing humidity. They suggested that evaporation and solidification rates decrease for higher RH which provides longer stretching time for the electrospinning jet and consequently, smaller diameter fibers are formed. Similar trend was observed by Jan et al. [91] for a variety of polymer/aqueous or acidic solvent systems such as polyvinyl



alcohol (PVA)/water, PVA/hyaluronic acid (HA)/water, PEO/acetic acid, and PEO/chitosan (CS) /water. Conversely, De Vrieze et al. [92] observed that the diameter of electrospun nanofibers from cellulose acetate (CA)/ Dimethylacetamide (DMAc) solution increased as RH increased. To find an explanation they added water into CA/DMAc solution and found fast precipitation of the polymer. Thus, at higher RH, precipitation of the polymer occurs fast as more water is absorbed into the polymer jet which prohibits the elongation of the jet and consequently, higher diameter fibers are produced. Similar observation can also be found in the work of Fashandi et al. [115] for electrospun nanofiber from polyetherimide (PEI) solutions of three organic solvents such as DMF, DMAc, and N-Methyl-2-pyrrolidone (NMP).

RH has also been found to affect the surface morphology and internal structure of electrospun fibers. Lu et al. [116] investigated the influence of RH on surface morphology and internal pore on electrospun nanofiber from polystyrene (PS) solution of a high volatile solvent, tetrahydrofuran (THF) and a low volatile solvent, DMF. They observed fibers with smooth surface and solid cross-section at low (2%) RH, while pores were formed at high (22% and more) RH. However, they found pores only on the fiber surface for PS/THF solution, while pores contribute to the structure of the fibers from PS/DMF solution.

Recently, Vrieze et al. [92] investigated the effect of ambient temperature on the diameter of CA and PVP nanofibers electrospun from CA/DMAc and PVP/ethanol solutions, respectively. In both cases, they observed an initial increase in nanofiber fiber diameter when temperature was increased from 10°C to 20°C. Further increase in

temperature to 30°C reduces the diameter of the nanofibers. They mentioned two factors, i.e., evaporation rate and viscosity of the solution, that vary differently with the temperature decide the diameter of the nanofibers.

## **2.5 Key Research Questions – Part I**

Research Question 1: *How can one obtain uniaxially aligned electrospun nanofiber yarn for composite reinforcement application?*

The deposition of electrospun fibers onto a stationary collector is essentially random due to the chaotic motion of the electrospinning jet as it travels to the collector [117]. The small pore size obtained by the random morphology of the nonwoven electrospun mat is particularly advantageous for membrane and filter applications. However, this random morphology limits the use of the electrospun nanofibers in composite reinforcement applications where alignment of the nanofibers and collection of the nanofibers in the form of yarn are important for optimum utilization of the strength of the fibers. Thus, the electrospinning apparatus should be design such a way that the collection of the fibers is in the form of uniaxial aligned arrays, and long yarns can be made from those aligned nanofibers.

Research Question 2: *How do electrospinning voltage and flow rate affect the fiber diameter and mechanical properties of electrospun PAN nanofibers?*

Many researchers have worked on the electrospinning of PAN/DMF solution and obtained electrospun PAN fibers with diameters in the range of 100–2700 nm

depending on various electrospinning parameters [108, 118-120]. While significant insights have been achieved, there is still inconsistency in the findings of the influence of electrospinning voltage and flow rate on the diameter of the PAN nanofiber as discussed in section 2.4.2. Thus, the investigation of the influence of the electrospinning voltage and flow rate on the fiber diameter and mechanical properties is important.

Research Question 3: *How do RH and temperature influence the diameter, surface morphology, internal structure, and mechanical properties of the electrospun PAN nanofibers? What is the mechanism of pore formation during electrospinning? How does heat treatment (i.e. annealing) of the fibers further affect those properties?*

RH and temperature influence not only the fiber diameter but also the surface morphology and internal structure of the electrospun nanofibers. By controlling these parameters porous and nonporous fibers can be obtained. Porosity in the structure of electrospun PAN nanofibers is preferred for some applications such as energy storage and filtration. However, porosity is not desired for the application of electrospun PAN nanofibers as precursor fibers for ECNFs. Hence, investigation of the impact of RH and temperature on fiber diameter, surface and internal morphologies, and mechanical properties of the electrospun PAN nanofibers is critical. Moreover, understanding the mechanisms of the formation of various structures during electrospinning is vital for better controlling of these parameters.

Annealing has been found to reduce the porosity of electrospun fibers [121] and increase the crystallinity of polymer [122]. Increasing crystallinity often increases the

strength of polymer, but reduces the strain at break. On the other hand, reduction of internal porosity may increase both strength and strain at break. Thus, a study on the impact of annealing is essential for further maneuvering of the structural properties of the electrospun nanofibers.

## **Chapter 3: ALIGNMENT OF ELECTROSPUN NANOFIBERS**

### **3.1 Introduction**

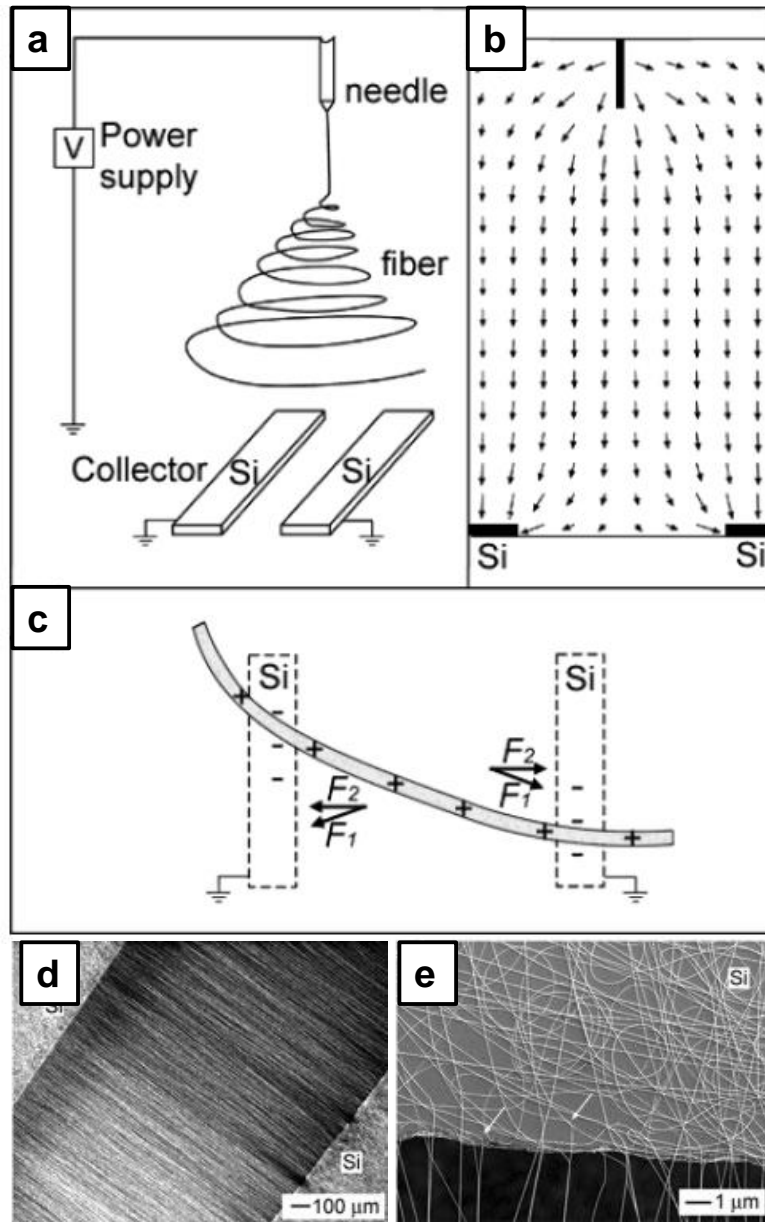
Due to the bending instabilities associated with spinning jet, the electrospun fibers are often deposited on the surface of the collector as randomly oriented nonwoven mats [117, 123]. However, uniaxial alignment of the nanofibers within ordered array is important for many applications. For example, in the field of tissue regeneration addressed to muscles, bone and cartilage meniscus, and neural cells, it has been demonstrated that cell cultures on uniaxially aligned nanofibrous scaffolds preferentially elongate along the fiber longitudinal axis [124]. Well-aligned and highly ordered architectures are often required in the fabrication of electronic and photonic devices [125]. Composite samples containing aligned sulfonated polyimide nanofibers can be employed in proton-exchange membrane fuel cells for converting chemical energy to electrical energy with high efficiency and low emission of pollutants [126]. Similarly, it is critical to control the alignment of fibers for fiber-based reinforcement application for the optimum utilization of the strength of fibers.

### **3.2 Review on Electrospinning Designs and Nanofiber Assemblies**

Due to such high added value of uniaxially aligned nanofiber yarns, many modifications of the electrospinning collector geometry have been carried out to directly collect the electrospun nanofibers as uniaxial aligned arrays. Innovative alignment experiments have been demonstrated by using two conductive collecting strips separated by a well-

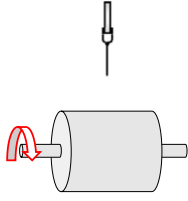
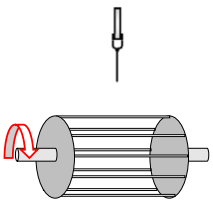
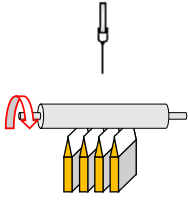
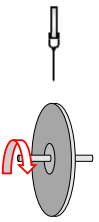
defined gap (up to several centimeters) [127]. The introduction of an insulating gap to the collector alters the configuration of the electrostatic forces acting on the fibers spanning across the gap. Due to the action of such electrostatic forces in opposite directions, the charged fibers are stretched across the gap to form a parallel array. Polyvinyl pyrrolidone (PVP) nanofibers were aligned in this way. As shown in Figure 3.1, optical and scanning electron microscopy (SEM) micrographs indicate that the nanofibers across the gap have their longitudinal axes oriented perpendicular to the conductive edges (Figure 3.1d), very differently from nonwovens collected on continuous conductive planar surfaces (Figure 3.1e). Although the principle behind this approach is elegant and the setup is simple, unfortunately the ability to scale up this technique to produce large quantity of sample is poor. Moreover, the fabricated yarn is of limited length which also limits the application for composite reinforcement.

To produce aligned nanofiber with higher scalability and flexibility, researchers have used rotating collector. Table 3.1 depicts some examples of the electrospinning setups with rotating collectors along with their advantages and limitations [128]. Among all the setups metal disc collector is the promising one to make uniaxially aligned nanofiber yarns. However, it needs little modification as fiber deposition can occur on the flat surface of the disc as well as on the shaft, and those fibers will not be aligned. While forming yarn from the deposited fibers, it will be very difficult to separate the aligned fibers from the random ones. The modification of the design of the disc collector will be discussed in section 3.3.



**Figure 3.1** (a) Schematic diagram of parallel auxiliary electrode arrangement. (b) Electric field profile from the spinneret to the parallel auxiliary electrodes. (c) Analysis of the electrostatic force on a charged nanofiber spanning across the gap. (d) Dark field optical micrograph of the nanofibers collected across the gap between two silicon strips. (e) SEM image of the nanofibers taken from the region close to the edge of silicon strip [127].

**Table 3.1** Schematic of various electrospinning setups with rotating collectors, and their advantages and disadvantages.

Setup	Schematic	Advantages	Limitations
Rotating metal drum		<ul style="list-style-type: none"> <li>• Simple setup</li> <li>• Large area of aligned fibers can be fabricated</li> </ul>	<ul style="list-style-type: none"> <li>• Highly aligned fibrous assemblies are difficult to fabricate</li> <li>• Fiber breakage may occur if rotating speed is too high</li> </ul>
Rotating wire drum		<ul style="list-style-type: none"> <li>• Simple set-up</li> <li>• Highly aligned fibers are possible</li> </ul>	<ul style="list-style-type: none"> <li>• Thicker layer of aligned fibers are not possible</li> <li>• Fibers may not be aligned throughout the whole assembly</li> </ul>
Rotating non-conductive tube collector with knife-edge electrodes below		<ul style="list-style-type: none"> <li>• Highly aligned fibers are possible</li> <li>• Aligned fibers covered the whole tube</li> </ul>	<ul style="list-style-type: none"> <li>• Set-up requires a negative electrode to be effective</li> <li>• Only possible for small diameter tube</li> </ul>
Metal disc collector		<ul style="list-style-type: none"> <li>• Simple set-up</li> <li>• Highly aligned fiber deposition is possible on the disc edge</li> <li>• Long yarn can be made</li> </ul>	<ul style="list-style-type: none"> <li>• Random fiber deposition may occur on the disc flat surface</li> </ul>



### 3.3 Design of Electrospinning Setup

The basic components of an electrospinning apparatus are an electrospinning chamber, a high voltage power supply, a polymer reservoir, and a collector. The electrospinning chamber should be electrically insulated so that no interruption in the electric field between the needle and the collector occurs. The chamber should also be closed to control the environment inside the chamber. The surface of the collector where fiber will be deposited should be grounded. A schematic of the electrospinning setup is shown in Figure 3.2. As seen in the figure, a rotating disc type collector was used. According to the discussion on various electrospinning designs in section 3.2, highly aligned nanofiber can be deposited on the edge of a metal disc collector. However, there is a possibility of random fiber deposition on the flat surface of the metal disc and on the shaft, and those random fibers will be difficult to separate while making yarn from the deposited aligned fibers. Thus, the material for the disc and the shaft was chosen as plastic. A copper foil (width: 1.27 cm) glued on the surface of the outer edge of the plastic disc (diameter: 25 cm) was used as collector. A tiny slot was cut on the disc to facilitate the electrical connection between the collector and ground. A grounded copper wire was passed through the shaft and the slot to the copper foil. Extra caution was taken by coating the copper wire with electrically insulated material so that no electric field was developed between the needle and the copper wire which might have weakened the electric field between needle and the copper foil. A motor was used to control the rpm of the disc. A photograph of the electrospinning setup is shown in Figure 3.3.

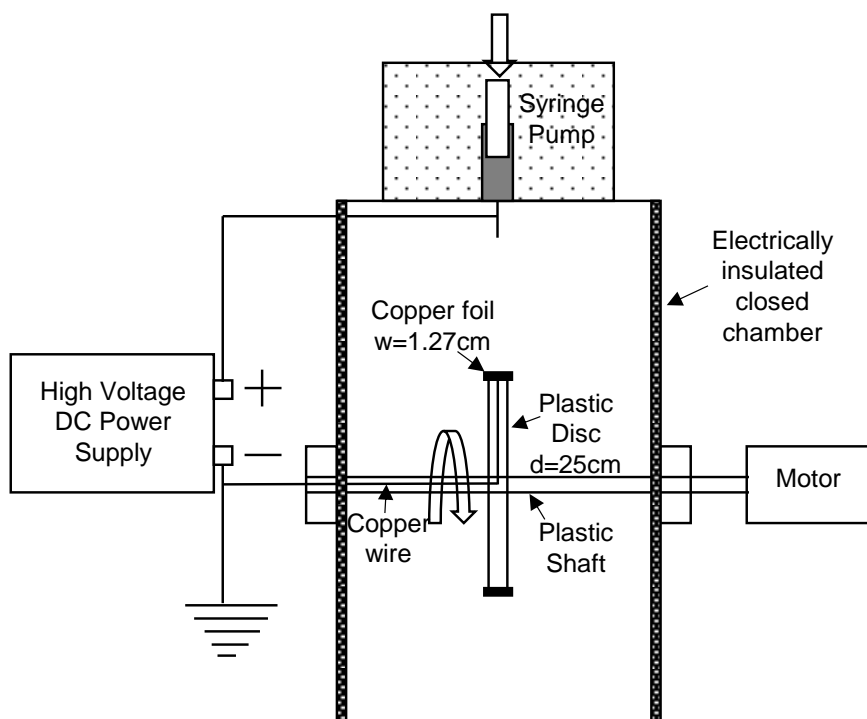


**Figure 3.2** A schematic of the electrospinning setup.

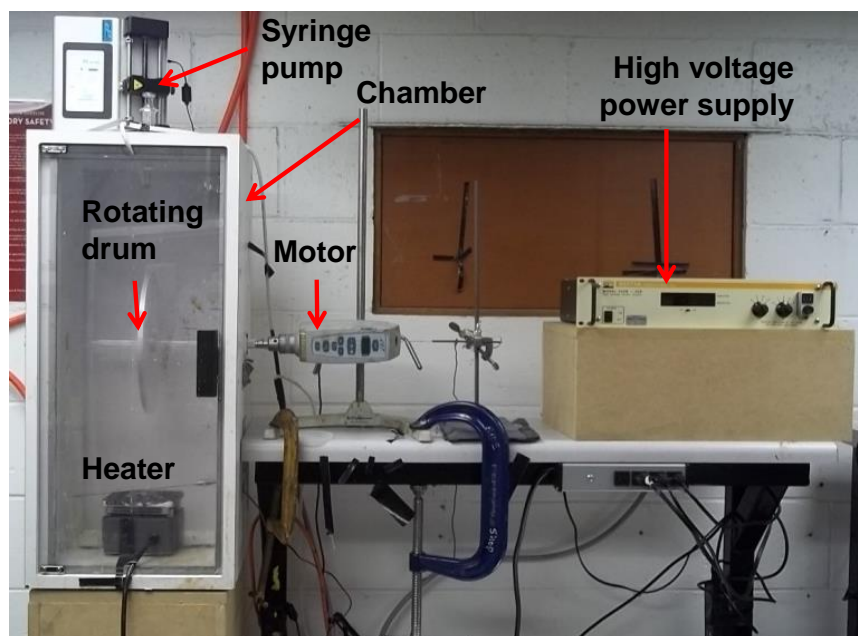


**Figure 3.3** A photograph of the electrospinning setup.

### 3.4 Effect of Collector Surface Velocity on Fiber Alignment

The rotation of the target surface affects the trajectory of the electrospinning jet. When a fiber is collected onto the target surface, it is electrostatically attached to the surface and can be used to align the landed fibers in the direction of the target [34]. Thus with increasing the surface velocity the effective draw can be increased resulting in less deviation between fiber and rotation direction and better alignment of the collected fiber. Figure 3.4 shows the SEM images of the electrospun PAN nanofibers collected on the copper foil of the collector disc rotating at different rpm. As seen from the images, the alignment of the nanofibers increased with the increase of the surface velocity of the collector disc. However, there is no significant difference in the alignment between 600 rpm and 800 rpm. Thus, for the rest of the studies all the nanofibers were produced at 600 rpm.

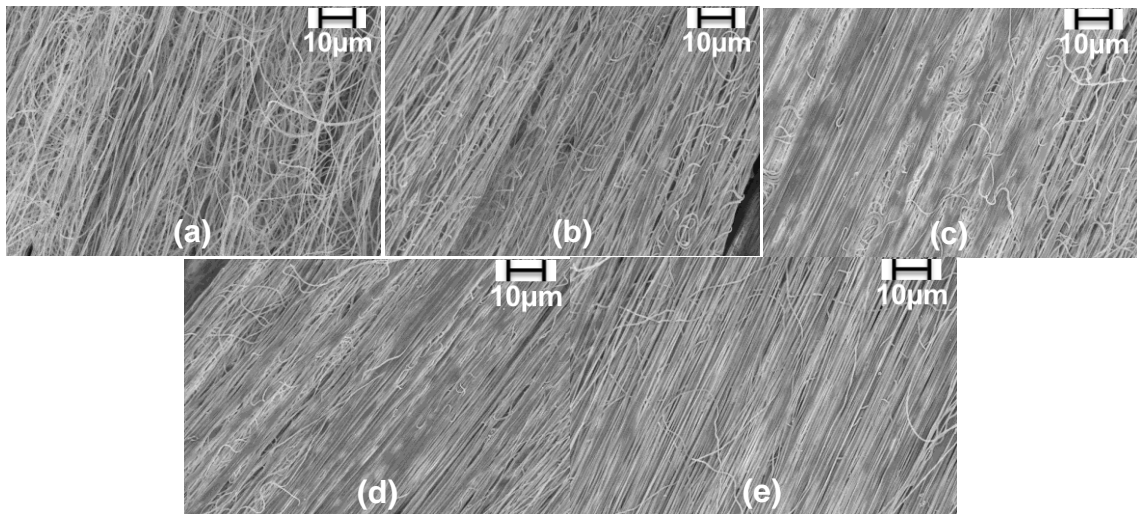


**Figure 3.4** SEM images of electrospun PAN nanofibers collected onto the collector disc rotating at (a) 50 rpm, (b) 200 rpm, (c) 400 rpm, (d) 600 rpm, and (e) 800 rpm.

### **3.5 Chapter Conclusions**

Alignment of electrospun nanofibers is important for many applications. A review of various designs of the collector is presented along with their advantages and disadvantages. Among all the designs, metal disc was found to be the best; however it had some limitations which were eliminated in the new design of the collector. The complete design of the electrospinning chamber is also presented. The alignment of the deposited fibers was improved with increasing the rotation of the disc.

## **Chapter 4: INVESTIGATION OF ELECTRIC FIELD AND FLOW RATE**

### **4.1 Introduction**

Reneker and Yarin [129] investigated the effect of flow rate and electric voltage on the Taylor cone for stable electrospinning process. They found that the rate at which solution flows into the Taylor cone must be equal to the rate at which fluid is carried away by the jet to achieve a stable electrospinning process. They defined this condition as quasi-stable point which can be achieved by investigating the Taylor cone at the tip of the needle by adjusting either the applied voltage or the flow rate or both. Thus, higher flow rate is required at higher applied voltage for a stable electrospinning process. Recently, Cai and Geveler [114] have shown that a minimum fluctuation in the volume of the Taylor cone is required to maintain the electrospinning process stable for a long time.

In this chapter, the influence of solution flow rate and applied voltage on the diameter of electrospun polyacrylonitrile (PAN) nanofibers are investigated. The Taylor cone at the tip of the needle is studied and the fiber current is monitored to identify different flow regimes at different applied voltages. The influence of different flow regimes on the stability of Taylor cone and the resultant average fiber diameter and tensile properties of the PAN nanofiber yarns are also investigated.

## **4.2 Experimental**

### ***4.2.1 Polyacrylonitrile (PAN)/DMF Solution Preparation***

Polyacrylonitrile (PAN) with an average molecular weight of about 150,000 g/mol was used as polymer and N,N-dimethylformamide (DMF) was used as solvent to make 10% PAN (by wt.) in DMF polymer solution. Both polymer and solvent were purchased from Sigma-Aldrich. PAN polymer powder was dried at 100°C under vacuum for 2 hrs to remove any access moisture and then dissolved in DMF at 80°C using a magnetic stirrer to obtain the spinning solution. Any air bubbles entrapped into the solution were carefully purged prior to electrospinning.

### ***4.2.2 Electrospinning Process***

The spinning solution was fed using a vertical syringe pump via a stainless steel needle having 0.41 mm inner diameter. The needle was electrically connected to a positive high voltage DC power supply purchased from Spellman High Voltage Electronics Corporation. The distance between the tip of the needle and the upper surface of the disk was kept constant at 18 cm. Electrospinning was carried out by applying a positive high voltage to the needle while the disc was rotating at 600 rpm to produce aligned fibers in the direction of rotation. The solution flow rate was maintained using a positive displacement syringe pump (KDS 200) purchased from KD Scientific Inc. About 200  $\mu$ l solution was deposited on the disc. All electrospun nanofibers were collected at 20°C and 30% RH.

### 4.2.3 Yarn Preparation

The electrospun nanofibers were peeled off from the copper foil in the form of yarn after immersing in distilled water. The yarns were then mounted on a drying rack to keep them in tension and dried at 95°C for 5 h. Photographs of the PAN nanofiber yarns showing peeling off the disc and drying rack with nanofiber yarn mounted are shown in Figure 4.1.

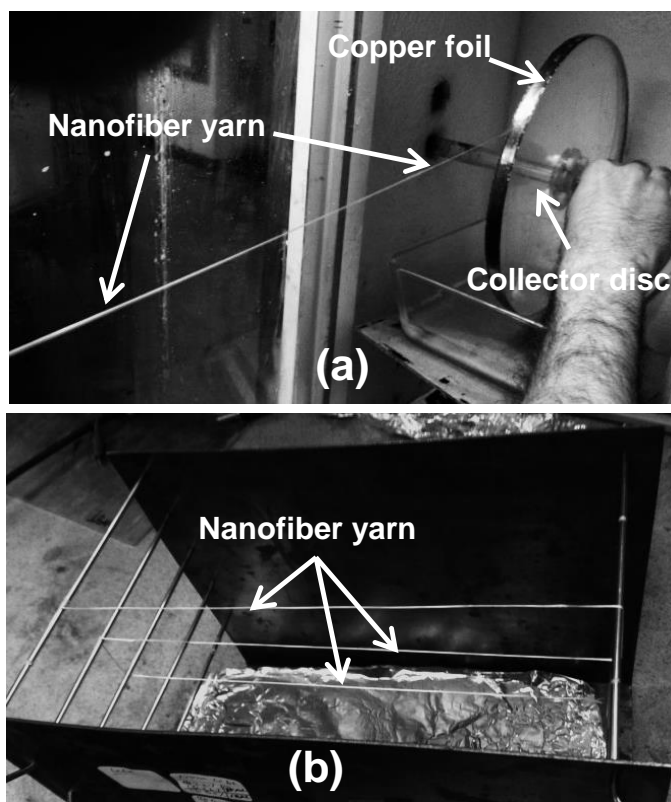


**Figure 4.1** Photographs showing (a) peeling off the PAN nanofiber yarn from the copper foil on the rotating disc and (b) drying rack with nanofiber yarns mounted.

#### ***4.2.4 Taylor Cone Analysis***

An optical camera was used to visually observe the Taylor cone region during the electrospinning process. ImageJ, an image processing and analysis software, was used to process and convert the optical images to binary images. An example of optical image and its binary image of Taylor cone is depicted in Figure 4.2.

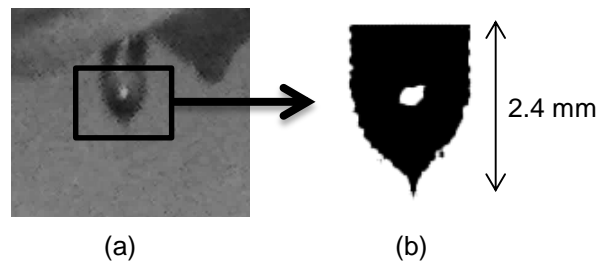


**Figure 4.2** Optical image of the Taylor cone region (a) and its binary image (b) after processing using ImageJ software.

#### ***4.2.5 Fiber Current Measurement***

The charge carried by the polymer solution jet, defined as fiber current, was measured by a multimeter placed between the collector and the ground (Figure 4.3). A RS232 cable connected to a computer along with a data logger software was used to read the current signal. The accuracy of the current measurement was validated by adding a simple circuit of a known voltage (1.56 V) and a known resistance in series (Figure 4.4).



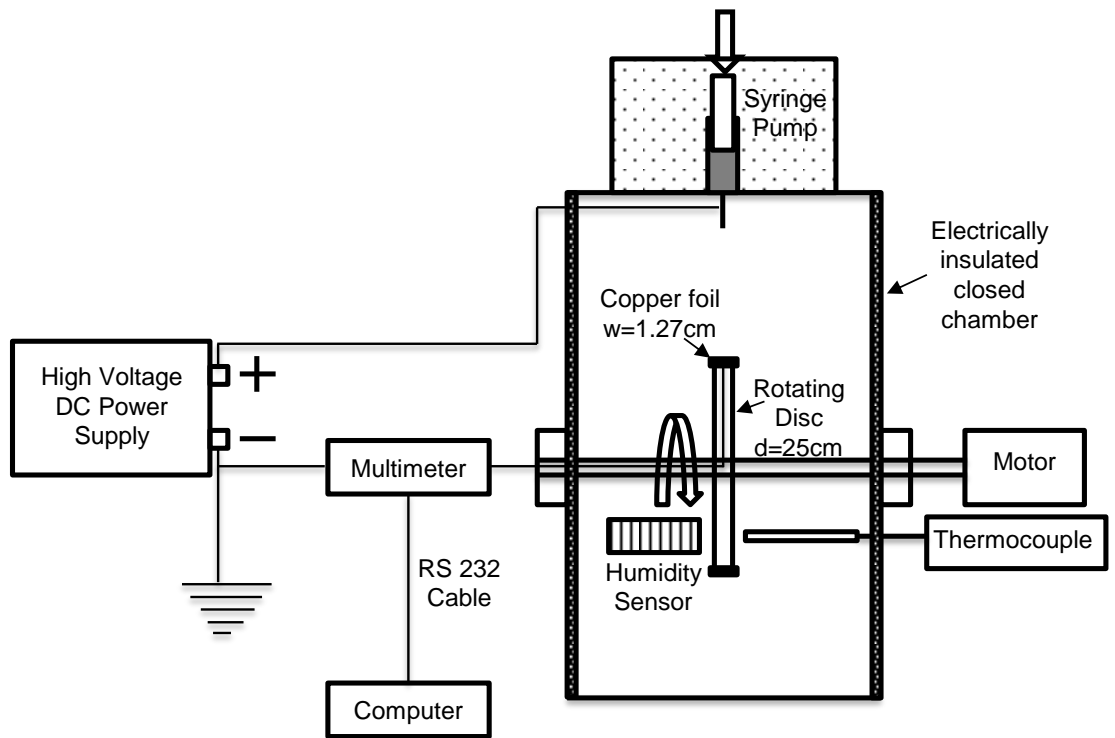


**Figure 4.3** Schematic representation of electrospinning process along with fiber current measurement technique.

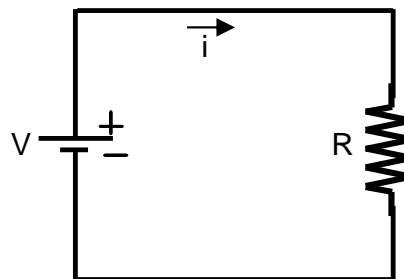


**Figure 4.4** Circuit with known voltage and resistance for validation of the nA current measurement.

By changing the resistance ( $2\sim 24\text{ M}\Omega$ ) various theoretical current can be estimated. The actual current in the circuit was then measured using the multimeter via RS232 cable.

Figure 4.5 shows the variation in multimeter current readings as a function of time during an open circuit and a 163.8 nA theoretical current measurement. During the open circuit measurement, the multimeter readings vary within  $\pm 50$  nA (Figure 4.5, bottom curve) which is due to the accuracy limitation of the multimeter. Since multimeter reading accuracy is specified on a “per measurement point” the average value of the current readings for a range of time represent the actual current value. However, a normality test should be done for a range of time to verify the multimeter readings. Figure 4.6 shows the Anderson-darling normality test results, using a statistical analysis software Minitab, of the current readings shown in Figure 4.5. In both cases P-value is greater than 0.05 which means the data is normal. The corresponding average current readings from the multimeter are compared with the theoretical values for all three external resistances as shown in Table 4.1. Both theoretical and percent errors are also indicated. As seen from Table 4.1, all measurement errors are less than 2% of the theoretical current value which indicates that the average current value of the multimeter readings for any range of time represents the actual measured current.

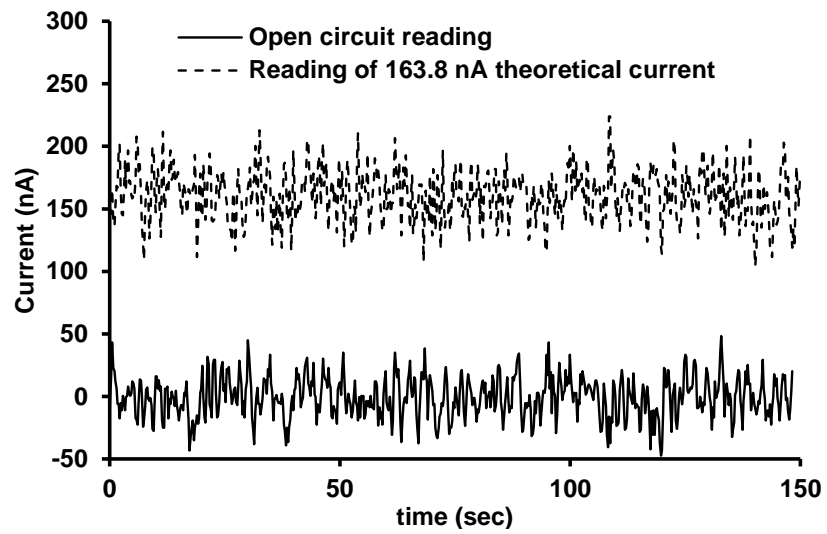


**Figure 4.5** Open circuit and 163.8 nA theoretical current reading of the multimeter.

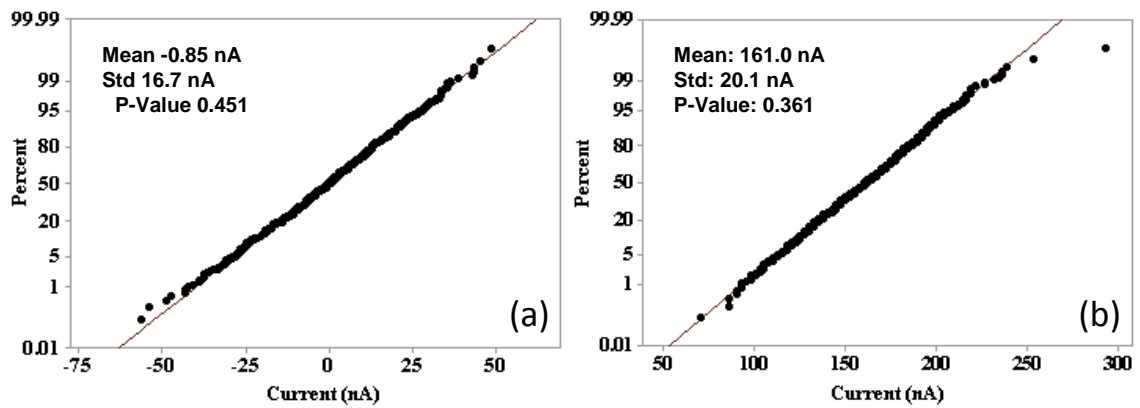


**Figure 4.6** Anderson-darling normality test for the data shown in Fig. 4. (a) Open circuit reading, (b) 163.8 nA theoretical current reading.

**Table 4.1** Comparison between estimated theoretical current and experimentally determined current.

Theoretical current (nA)	Experimental current (nA)	Deviation (%)
0 (open circuit)	-0.9	-
80.2	81.3	1.3
163.8	161.0	1.7
688.7	701.8	1.9

#### ***4.2.6 Diameter Distribution Characterization***

The morphology of the electrospun nanofibers were observed by SEM. Nanofiber yarns were mounted on the SEM sample holder, sputter coated with Iridium, and examined using a Zeiss Neon high resolution SEM. ImageJ was utilized to measure the diameter of the fibers. More than 70 fibers were measured to obtain the mean and standard deviation values of the diameter.

#### ***4.2.7 Mechanical Testing***

Dynamic mechanical analyzer (DMA) Q800 from TA Instruments was utilized to perform the tensile experiments. Nanofiber yarns were directly mounted on the DMA grip and aligned before applying any load. All tensile tests were performed at room temperature with a sample gauge length of 9-10 mm and at constant strain rate of  $0.001 \text{ s}^{-1}$ . The cross-sectional area of the yarn sample was calculated by dividing the mass of the yarn by its length and density of PAN. The density of PAN was assumed to be  $1.18 \text{ g/cc}$ .

## 4.3 Results and Discussion

### 4.3.1 Investigation on Taylor cone Morphology

During electrospinning process the polymer solution near the Taylor cone may appear in many forms depending on the process conditions. In this study, the Taylor cone at the tip of the needle was investigated at different flow rates and field strengths using an optical camera. Figure 4.7 shows various Taylor cone morphologies observed at different flow rates at 15 kV electric field. Based on the morphologies shown, jets are characterized as (a) dripping, (b) jet with intermittent drops, (c) continuous jet, and (d) discontinuous jet. Each Taylor cone morphology is also classified into a regime. At high flow rate (i.e., 32  $\mu\text{L}/\text{min}$ ), the electric field is not sufficient enough to overcome the surface tension of the fluid, hence fluid accumulates at the tip of the needle and eventually falls in drops (regime 1: dripping). With decreasing the flow rate, an emerged liquid jet can be found, however the electric field strength and charge density is still low at which the rate of fluid removal can't match with the rate of supply. Thus the nanofiber deposition is accompanied by intermittent droplets as shown in regime 2: jet with intermittent drops. Decreasing the flow rate below a critical value results in a continuous jet, however there is a large variation of the Taylor cone morphology observed in this region (i.e. regime 3) of flow rate. In this region a slight variation of the flow rate can significantly affect the Taylor cone morphology and the spinning jet. The flow rate corresponds to regime 4 leads to stable operation for a long period of time with minimal deviation. A slight decrease in the flow rate makes the Taylor cone region

narrower and variable jet (continuous jet - regime 5), and eventually reach to a point where the jet is no more continuous (discontinuous jet - regime 6).

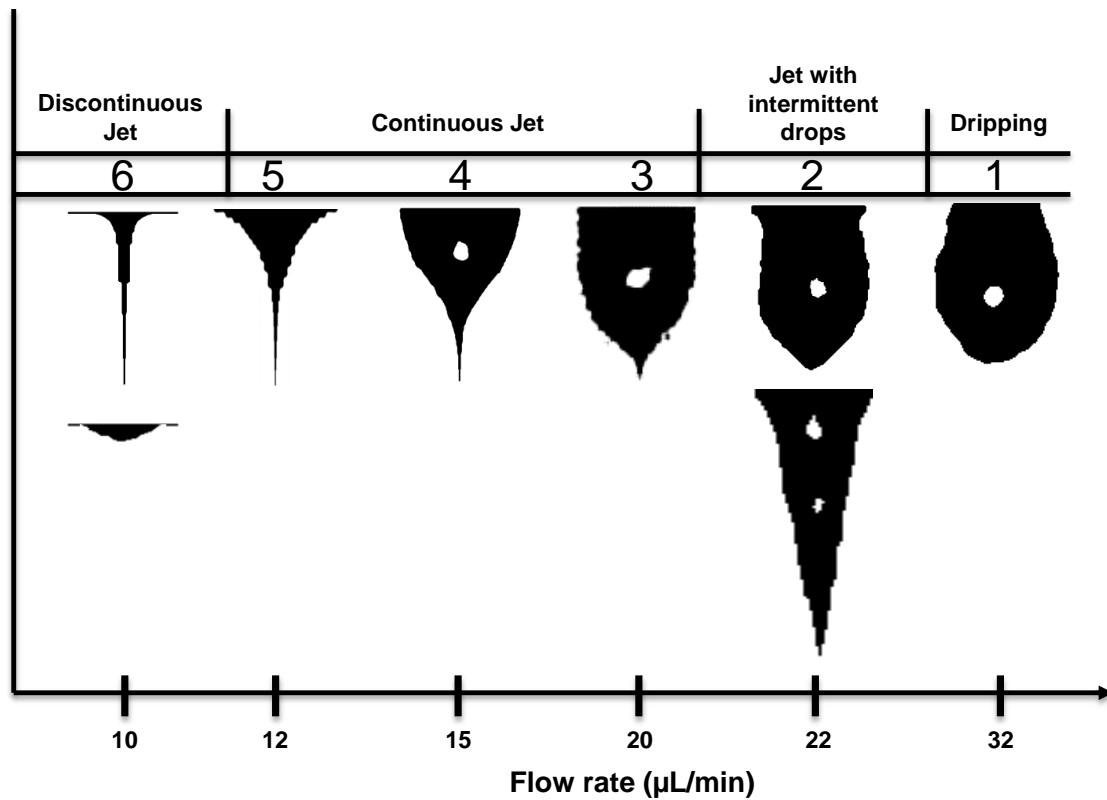


**Figure 4.7** Various Taylor cone morphologies observed at different flow rates operating at 15 kV electric field. 1- Dripping, 2- Jet with intermittent drops (bottom: change in Taylor cone shape right at the time of drop falling), 3 - continuous jet with large, bounded variations, 4 - continuous jet with minimal fluctuations, 5 - narrow, variable continuous jet, 6 - discontinuous jet (top), no jet (bottom).

The half angle of the Taylor cone, i.e. the sharpness of the hyperboloid shape was also studied to analyze the stability of the jet at various regimes. It has been reported in the literature that the half-angle ( $\alpha$ ) often lies in the range of  $32^\circ < \alpha < 46^\circ$  [130, 131] for

stable Taylor cone. However, Yarin et al. [132] theoretically predicted that the droplet approaches a conical asymptotic with a half angle of  $33.5^\circ$  when the electric field reaches its critical value. The experimental value of their half-angle for stable Taylor cone was  $37^\circ$ , very close to the predicted value. The measured half-angles of the Taylor cone for selected flow regimes such as regimes 2, 3, 4, and 5 and the values are shown in Figure 4.8. The corresponding half-angles were found to be about  $47^\circ$ ,  $45.5^\circ$ ,  $35.5^\circ$ , and  $23.5^\circ$  for regime 2, regime 3, regime 4, and regime 5, respectively. The half-angles for regime 2 and 5 are outside the stability range according to the reported values in the literature ( $32^\circ < \alpha < 46^\circ$ ) [130, 131] and ( $\alpha = 33.5^\circ$ ) [132]. Higher value of the half-angle in regime 2 indicates that the electrical potential is not high enough to keep up with the flow rate and eventually, falling into drops. Although regime 5 yielded continuous jet, the half-angle was found ( $\sim 23.5^\circ$ ) much lower than the predicted value of  $33.5^\circ$  which also made the Taylor cone unstable. With decreasing the flow rate the intermittent falling of the drops was prevented (regime 3), and half angle of the Taylor cone was reduced (around  $45.5^\circ$ ) and fall in the range of  $32^\circ < \alpha < 46^\circ$ . However, this angle is much higher than the predicted value of  $33.5^\circ$ , which is believed to be the reason for Taylor cone instability. The half-angle in regime 4 was found to be around  $35.5^\circ$  which is very close to the predicted and experimentally determined values by Yarin et al. [132] for stable electrospinning process. The half-angle value should maintain close to this number as long as the solution flow rate to the Taylor cone match with the solution leaving the Taylor cone as electrospinning jet, and it is believed that

the corresponding flow rate in regime 4 makes the electrospinning process more stable compared to other flow rates.

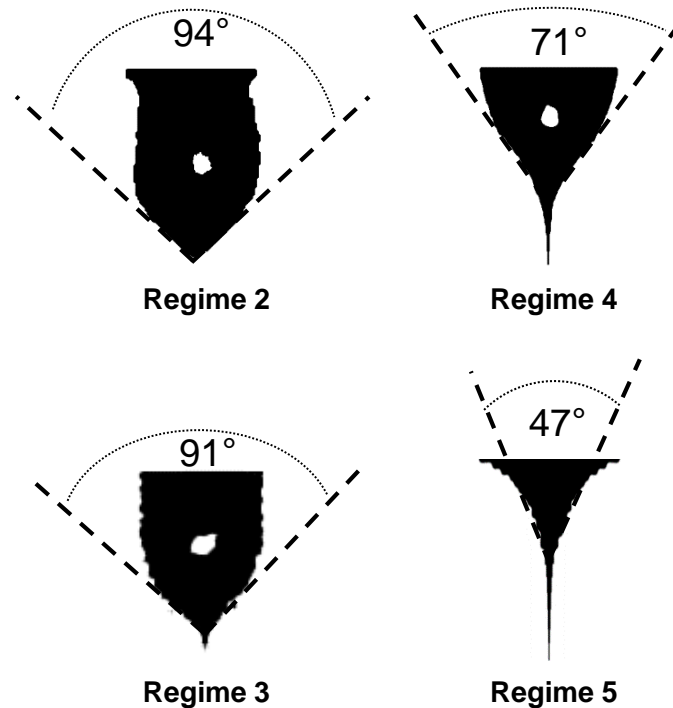


**Figure 4.8** Taylor cone angles for various regimes of interest (regime 2-5).

#### ***4.3.2 Upper and Lower Bounds of Flow Rate for Continuous Jet***

Analysis of the Taylor cone morphology, as described in section 4.3.1, was performed at three different electric fields (12, 15, and 18 kV) to determine the upper and lower bound of flow rates for continuous jet operation as shown in Figure 4.9. The flow rate for continuous jet operation was found to increase with increasing field strength. However, the slope of the upper bound flow rate curve is much higher compared to the



lower bound flow rate resulting in increase in operational window of the flow rate with increase of electrospinning voltage.

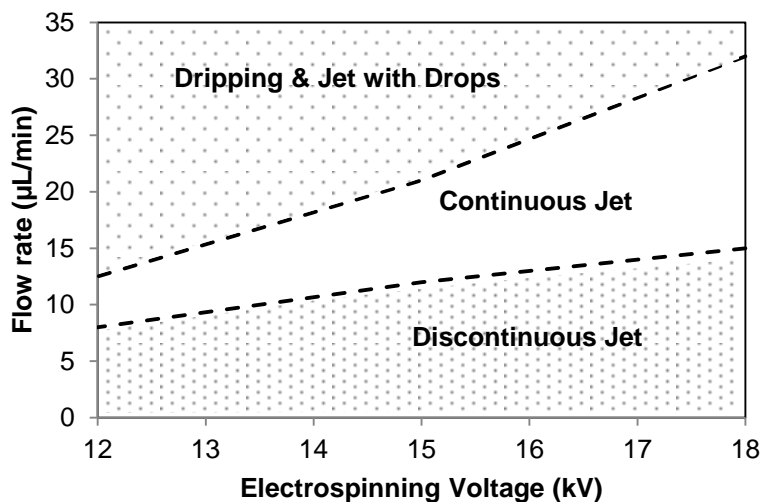


**Figure 4.9** Dependence of upper and lower bounds of flow rate on electric field for continuous jet operation.

#### 4.3.3 Investigation on Fiber Current

It was reported in the literature that the fiber current measurement can provide useful information about the deposition during the electrospinning process [120, 133]. In this study, the fiber current was measured to investigate fiber deposition state at different flow rates and applied voltages. Fig. 4.10 shows the variation of the instantaneous fiber current measured at different flow rates at 15 kV electric field. As shown, at 1 µL/min flow rate (Figure 4.10a), the fiber current was mostly zero except some intermittent sharp peaks. Due to a very low flow rate there was not enough solution at the tip of the

needle to eject a jet, resulting in no fiber deposition. Once enough solution accumulates at the tip of the needle, the liquid jet ejects from the needle in the form of fiber and deposit on the collector surface. At 5  $\mu\text{L}/\text{min}$  flow rate, an intermittent continuous jet condition was achieved, as seen from Figure 4.10b, where the electrospinning jet stayed continuous for about 20 s. The inset pictures show zero fiber current when there is no jet ejection and about 160 nA current when jet is ejected from the needle. At 10  $\mu\text{L}/\text{min}$  (Figure 4.10c), the fiber current with very sharp intermittent peaks (150 nA to zero) indicates that the electrospinning jet was in the verge of getting continuous. At 12  $\mu\text{L}/\text{min}$  flow rate, a continuous jet was achieved with fiber current not dropping to zero, as shown in Figure 4.10d. A few minor drops in fiber current from 150 nA to 50 nA is an indication of narrow and variable Taylor cone, as shown in Figure 4.7. No fluctuation in fiber current was observed at 15  $\mu\text{L}/\text{min}$  (Figure 4.10e) as expected from visual observation of the Taylor cone (Figure 4.7). Although there was fluctuation in the Taylor cone volume (Figure 4.7) at 20  $\mu\text{L}/\text{min}$ , no sharp peaks in the fiber current was observed (Figure 4.10f). Sharp downward peaks in the fiber current at low flow rates are indication of huge drop in the amount of fiber deposition rate. At higher flow rate, the fiber deposition rate may vary as the volume of the Taylor cone changes; however the total charge carried by the liquid jet did not cause any significant variation in the fiber current.

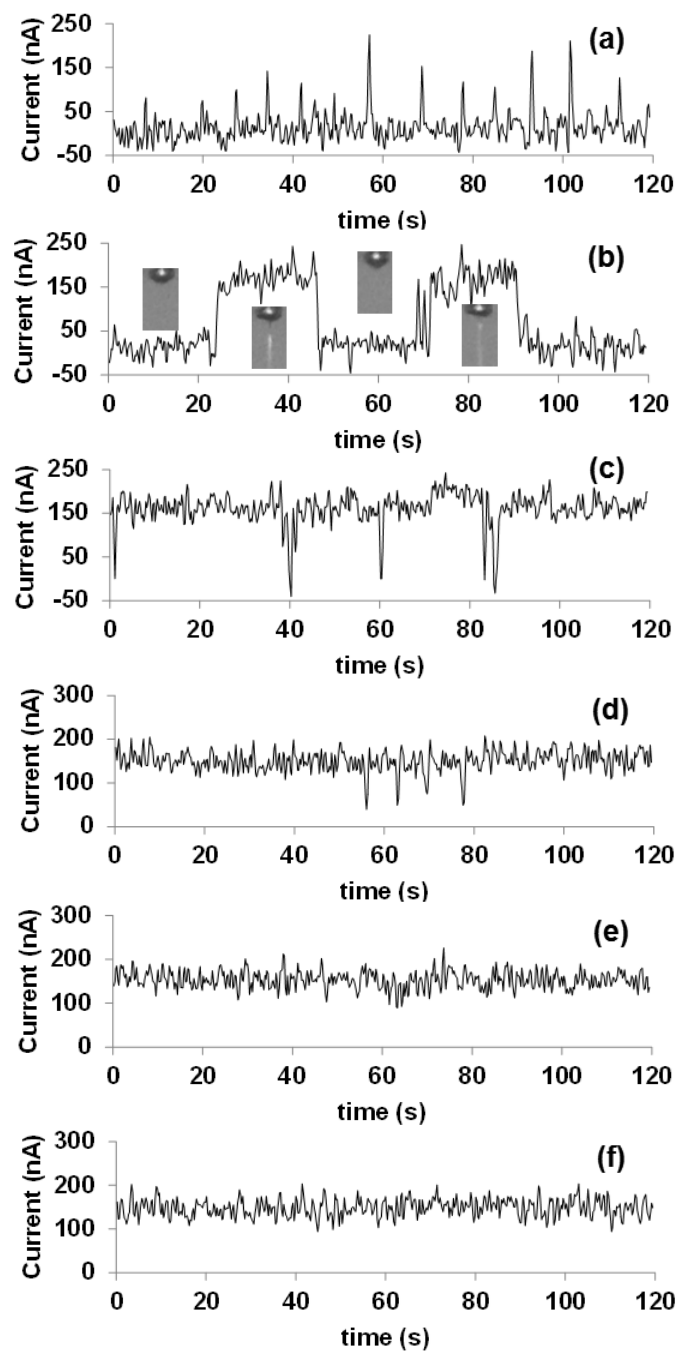


**Figure 4.10** Instantaneous fiber current at different flow rates operating at 15 kV electric field: (a) 1  $\mu\text{L}/\text{min}$ , (b) 5  $\mu\text{L}/\text{min}$  (inset pictures show intermittent jet ejection), (c) 10  $\mu\text{L}/\text{min}$ , (d) 12  $\mu\text{L}/\text{min}$ , (e) 15  $\mu\text{L}/\text{min}$ , and (f) 20  $\mu\text{L}/\text{min}$ .

#### ***4.3.4 Diameter Distribution of Electrospun Nanofibers***

PAN nanofibers were fabricated at different electric fields (12 kV, 15 kV, and 18 kV) and flow rates (5  $\mu\text{L}/\text{min}$  to 28  $\mu\text{L}/\text{min}$ ) covering both continuous and discontinuous jet regimes. A few SEM images and corresponding diameter distributions of PAN nanofibers produced at 15 kV electric field are shown in Figure 4.11 for continuous jet conditions and in Figure 4.12 for discontinuous jet conditions. As shown at 15  $\mu\text{L}/\text{min}$  and 17  $\mu\text{L}/\text{min}$  flow rates, the fibers were found to have smaller average diameter and narrower diameter distribution. Similar observations were also found at 20  $\mu\text{L}/\text{min}$  flow rate for 18 kV and at 10  $\mu\text{L}/\text{min}$  flow rate for 12 kV. For other conditions (continuous and discontinuous jet regimes), the nanofibers show larger average diameter and wider diameter distribution. It is believed that the electrospinning parameters that yield a stable Taylor cone produces uniform and smaller diameter fibers.

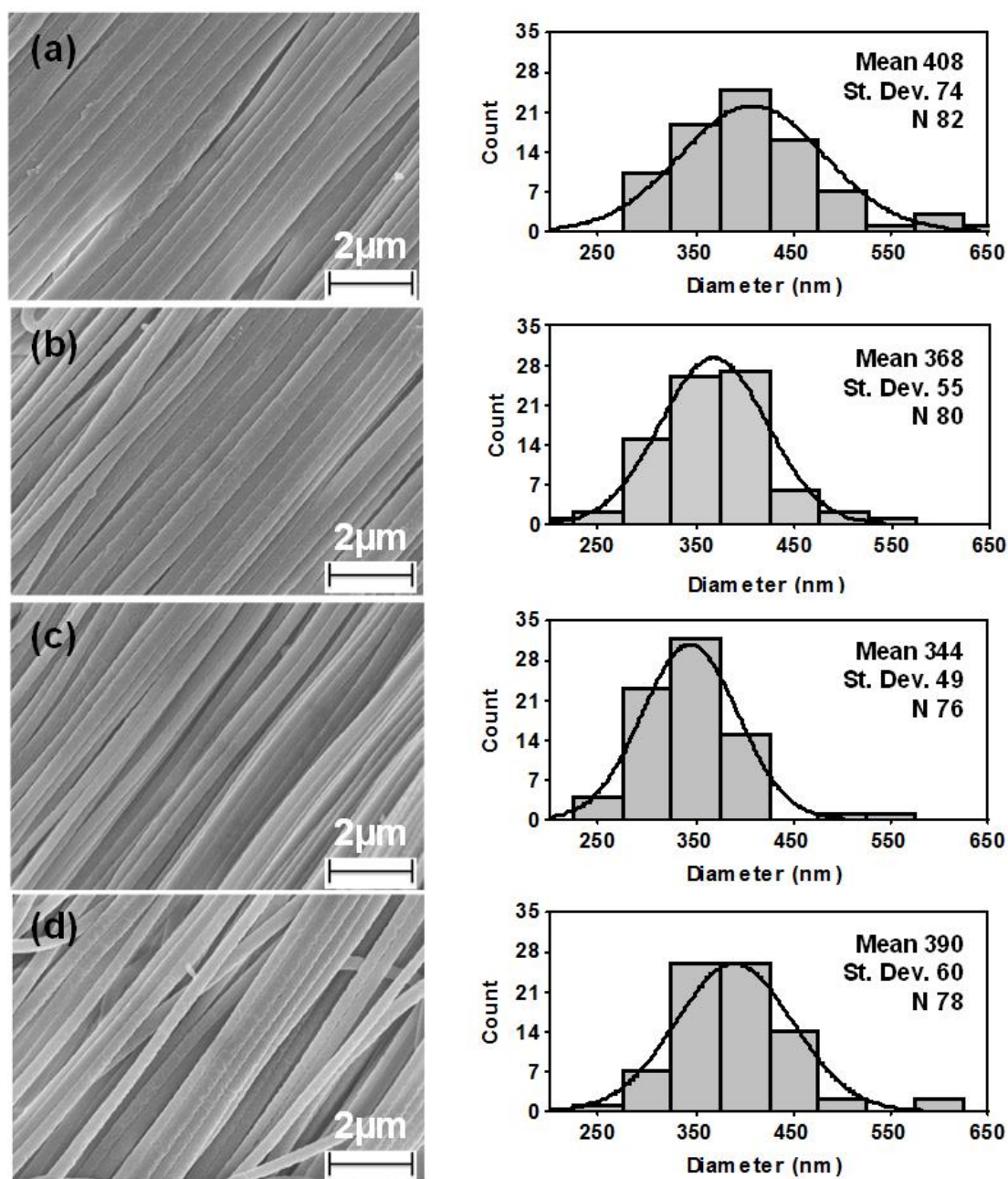


**Figure 4.11** SEM micrographs of PAN nanofibers and corresponding diameter distribution for 15 kV and at various flow rates in the regime of continuous jet. (a) 20  $\mu\text{L}/\text{min}$ , (b) 17  $\mu\text{L}/\text{min}$ , (c) 15  $\mu\text{L}/\text{min}$ , and (d) 12  $\mu\text{L}/\text{min}$ .

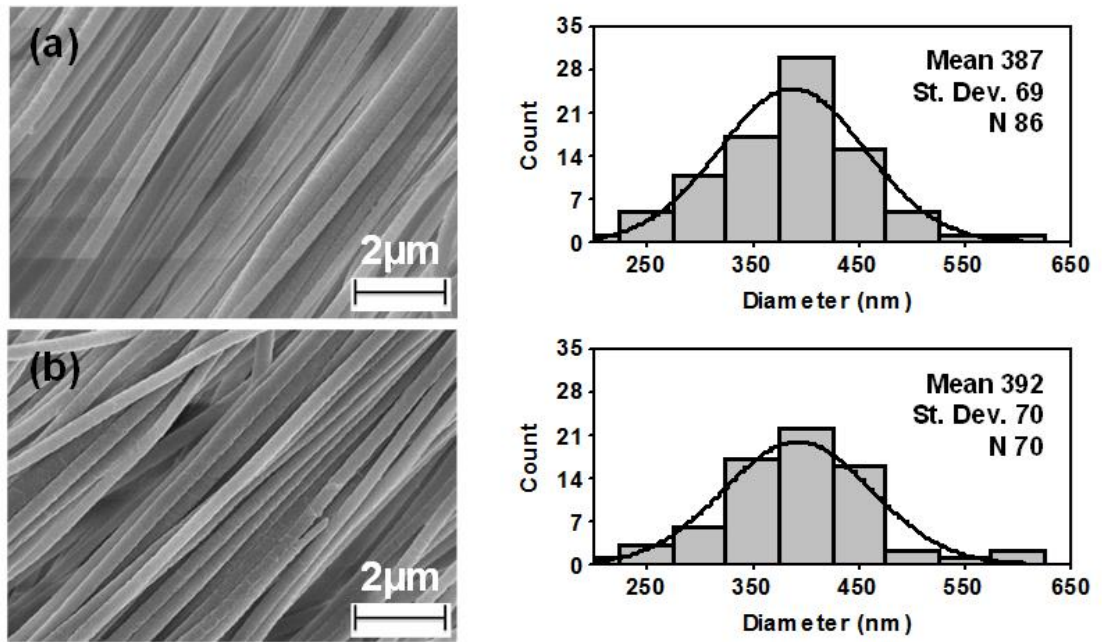


**Figure 4.12** SEM micrographs of PAN nanofibers and corresponding diameter distribution for 15 kV and at various flow rates in the regime of discontinuous jet. (a) 10  $\mu\text{L}/\text{min}$ , and (b) 5  $\mu\text{L}/\text{min}$ .

#### 4.3.5 Effect of Electric Field and Flow Rate on Nanofiber Diameter

Figure 4.13 shows the variation of average nanofiber diameter as a function of flow rate for 15 kV and 18 kV electric fields. It can be seen that at both electric fields, the fiber diameter reaches to a minimum value before increasing with further increase in the flow rate. The condition at which the fiber diameter reaches to a minimum value can be called as “favorable flow rate”. As seen from figure, the favorable flow rate is about 15  $\mu\text{L}/\text{min}$  at 15 kV and is about 20  $\mu\text{L}/\text{min}$  at 18 kV. Thus, it can be stated that the favorable flow rate is higher at higher applied voltage which has a physical significance.

For example, higher production rate of nanofibers can be achieved by adopting higher favorable flow rate corresponds to higher electrospinning voltage.

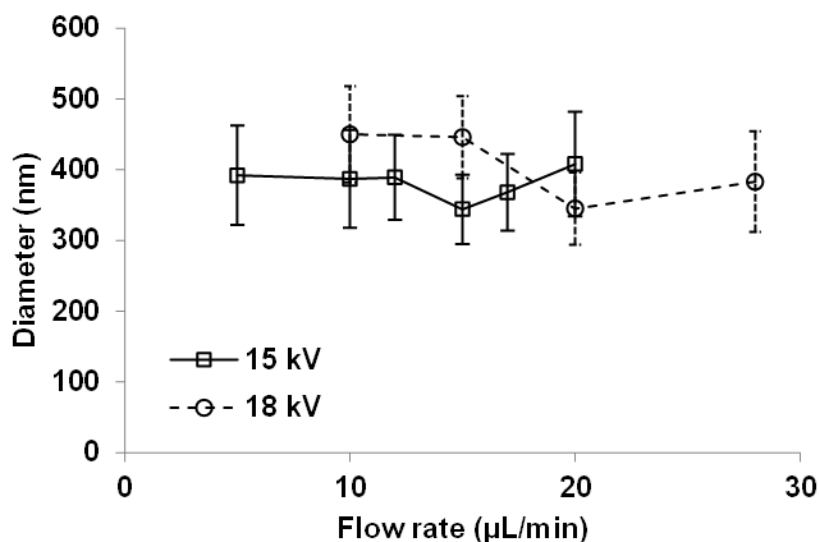


**Figure 4.13** Variations in average nanofiber diameter as a function of flow rates for 15 kV and 18 kV electric fields.

### 4.3.6 Mechanical Properties of Electrospun Nanofiber Yarns

#### 4.3.6.1 Effect of Filament Diameter

In this study, three PAN nanofiber yarns with different average filament diameter were selected. All PAN nanofiber yarns were fabricated using flow rates and electric voltages within the continuous flow regime. Typical tensile stress vs strain plots of selected PAN nanofiber yarns with different average filament diameter are shown in Figure 4.14. As seen, both tensile strength and modulus increased as the filament diameter decreases in the yarn. It is expected that the alignment of the polymer chains/molecules increases

with diameter decreases due to stretching of the fiber during the electrospinning process. However, interestingly, the strain at break and toughness were found to increase with decrease in filament diameter. Based on the classical behavior of the structural materials, one would expect strain at failure and toughness to decrease as strength and modulus increase. The unusual behavior of electrospun nanofibers was also observed by Papkov et al. [134]. They found that the degree of crystallinity of the nanofiber decreased with decrease of nanofiber diameter. According to them, low crystallinity of electrospun nanofiber may be the result of fast solvent evaporation from electrospun jets leading to rapid jet solidification. As smaller jets lose more solvent and solidify quicker, the degree of crystallinity is lower for yarns with lower nanofiber diameter resulting in higher strain at break and toughness. Higher diameter nanofibers need more time for solvent evaporation, and hence polymer molecules have enough time to crystallize. Moreover, exhaustion of solvent may not occur completely and some solvent molecule may be trapped under the solidified skin which may result in more voids in the larger diameter fiber and therefore, lower strength and strain in break were observed.



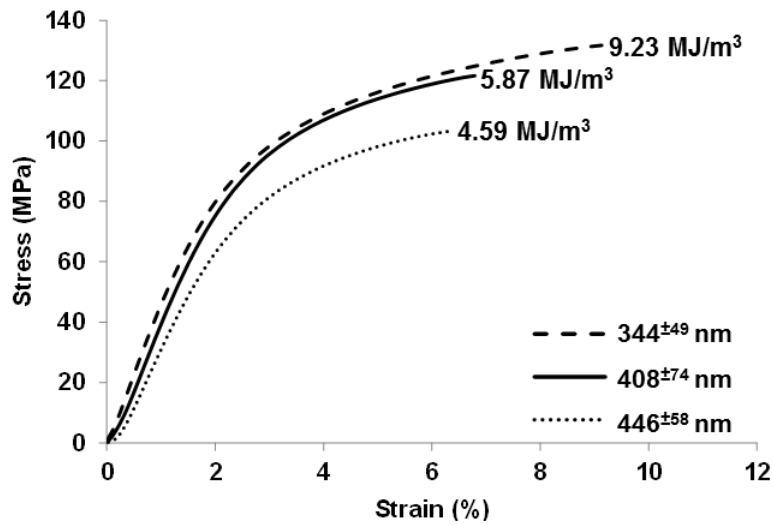


**Figure 4.14** Effect of filament diameter on tensile stress-strain behavior of PAN nanofiber yarns made from continuous jet conditions. Toughness was calculated from the area under the stress-strain curve.

#### 4.3.6.2 Continuous Jet vs Discontinuous Jet

In this study, a few nanofiber yarns with similar filament diameter fabricated using both continuous and discontinuous jet conditions were selected, and their typical tensile stress-strain plots are shown in Figure 4.15. Toughness values for each type of yarns are also included in the figure. As seen, yarns produced from discontinuous jet exhibited lower tensile properties (strength, strain, and toughness) compared to yarns produced from continuous jet. It is believed that the nanofiber yarns made from discontinuous jet consist of filaments with shorter in length and as a result they are less effective in transferring load from filament to filament. Yarns with longer filament are more effective in load transferring, and as a result show higher tensile properties.

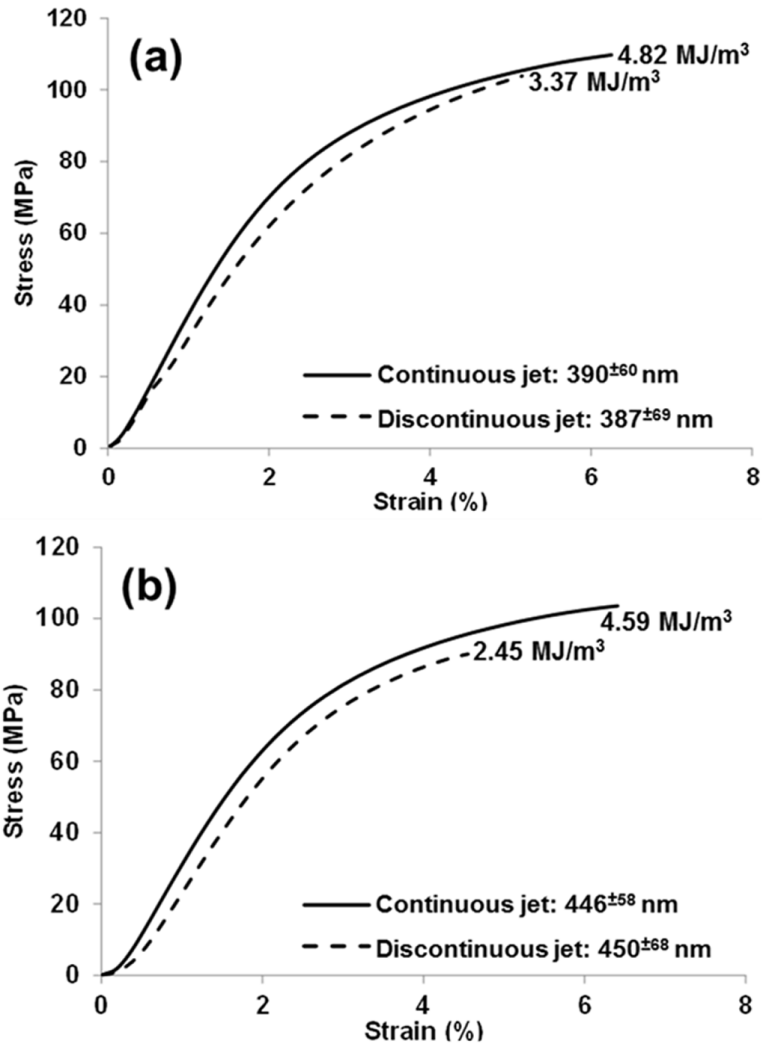


**Figure 4.15** Stress-strain plots of PAN nanofiber yarns having similar filament diameter produced from continuous and discontinuous jet conditions. Toughness was calculated from the area under the stress-strain curve.

#### 4.3.6.3 Effect of Flow Rate

Figure 4.16 shows the variation of tensile strength of PAN nanofiber yarns as a function of flow rate at different electric fields. Filled and non-filled symbols correspond to nanofiber produced using continuous jet and discontinuous jet, respectively. Their corresponding average filament diameters are also included in the figure. As shown in

Figure 4.16, PAN yarns made at flow rates in the discontinuous jet regime exhibited lower tensile strength. With increasing flow rate the jet condition becomes continuous and yarns show higher tensile strength up to a point beyond further increase in the flow rate decreases the tensile strength. The highest tensile strengths were found at 15  $\mu\text{L}/\text{min}$  for 15 kV and at 20  $\mu\text{L}/\text{min}$  for 18 kV. These conditions also yield PAN yarns with lowest filament diameter and other conditions result in larger diameter fibers due to excessive pooling of PAN solution and hence lower tensile properties.

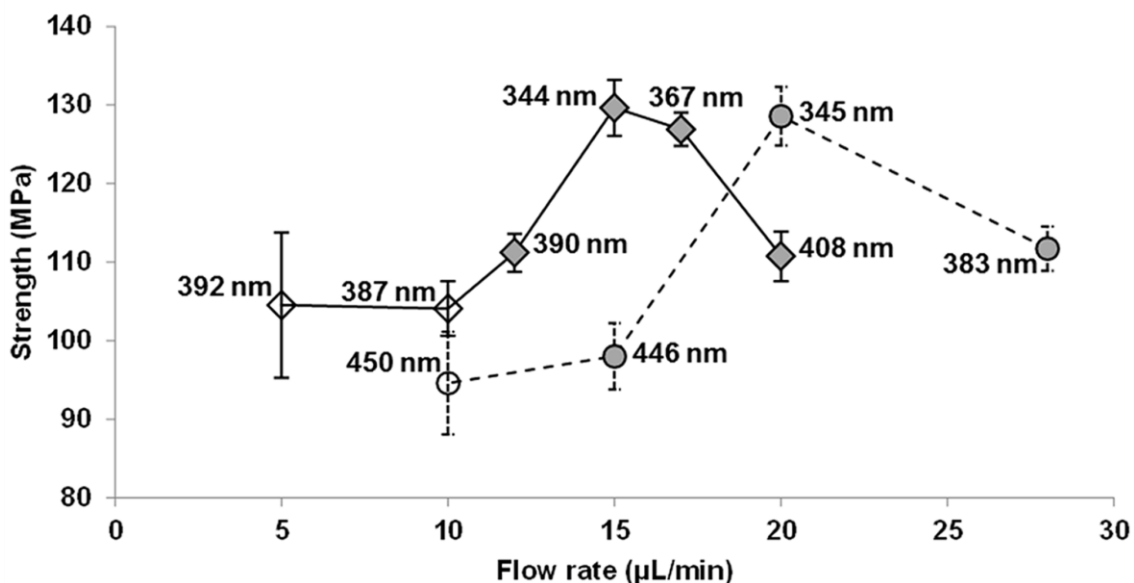


**Figure 4.16** Variation of tensile strength of PAN nanofiber yarns as a function of flow rate at different electrospinning voltage. Filled: Continuous jet, Non-filled: Discontinuous jet.

#### 4.3.7 Modeling of the Nanofiber Diameter

The dependences of nanofiber diameter on electrospinning voltage and flow rate cannot be isolated, rather they are unified and their combined effect can be defined in terms of volume charge density ( $I/Q$ ). Fridrikh et al. [135] developed a simple model to correlate the fiber diameter with the volume charge density by analyzing the dynamic equations, describing the motion of whipping jet of Hohman [136, 136]. Evaluating the asymptotic balance between normal stresses due to surface tension and surface charge repulsion, the relationship can be written as:

$$d_{\text{fiber}} = c^{1/2} \left( \gamma \varepsilon \frac{Q^2}{I^2} \frac{2}{\pi(2 \ln \chi - 3)} \right)^{1/3}$$

where  $c$  is the polymer concentration;  $\gamma$  is the surface tension (N/m);  $\varepsilon$  is the dielectric constant of ambient air;  $Q$  is the flow rate ( $\text{m}^3/\text{s}$ );  $I$  is the measured fiber current (A);  $\chi$  is the dimensionless wavelength of the instability response for the normal displacements. Volume charge density ( $I/Q$ ) has a unit of  $\text{C}/\text{m}^3$  and hence it means the strength of the electrostatic force acting on the jet. It is expected that the fiber diameter is proportional to  $(I/Q)^{-2/3}$  as other parameters remain constant. Thus, the average nanofiber diameter expected to decrease with increase in the volume charge density. Cai et al. [114] confirmed this analysis for Polyethylene oxide (PEO) aqueous solution; however, it is to be mentioned that this relationship holds true only if the flow rate represents stable regime of the Taylor cone and the relative humidity and temperature remain constant. It should also be noted here that  $d_{\text{fiber}}$  is only a limiting diameter arising from a balance between normal stresses due to surface tension and surface

charge repulsion; diffusion of nonsolvent molecule from the electrospinning environment into the solution jet may cause phase separation leading to arrest the jet prematurely with larger diameter.

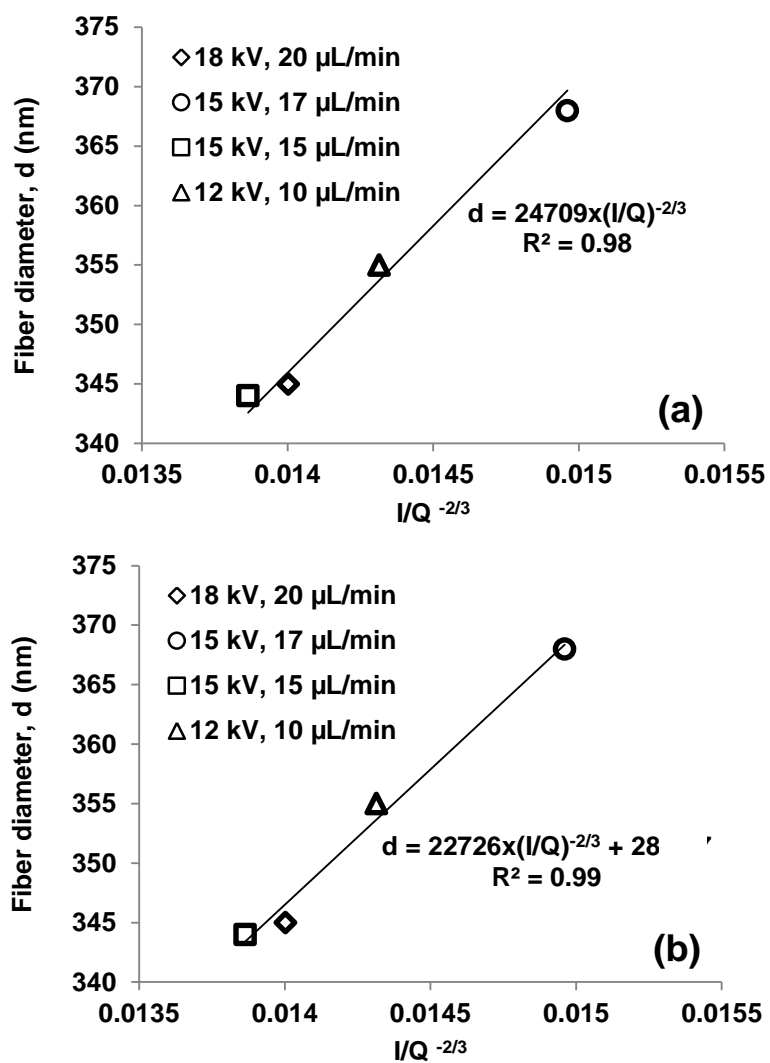


**Figure 4.17** Correlation between the average nanofiber diameter,  $d$  and volumetric charge density,  $(I/Q)^{-2/3}$ . (a)  $y=mx$  fit, (b)  $y=mx+c$  fit.

For verification, the average nanofiber diameter was plotted against the volume charge density ( $I/Q$ ) for four electrospinning conditions, where spinning jet was continuous and Taylor cone was stable. As seen from the Figure 4.17, the relationship between the fiber diameter and  $(I/Q)^{-2/3}$  is very linear. However,  $y = mx+c$  seems better fit the experimental data than  $y = mx$ , and the value of  $c$  being positive hints premature solidification of the fiber due to phase separation which will be discussed in details in Chapter 5. Nevertheless, it can be concluded that the electrospinning voltage and the flow rate affect the nanofiber diameter as a combined effect and can be used as a predicting tool for design of electrospinning process for nanofiber fabrication with improved mechanical performance.

#### **4.4 Chapter Conclusions**

This chapter investigates the effects of the electric field and flow rate on the diameter of electrospun PAN nanofibers and tensile properties of nanofiber yarns. By investigating the Taylor cone morphology at the tip of the needle, a favorable flow regime with minimal jet fluctuation can be determined. Yarns made using favorable flow conditions yield uniform and thinner nanofibers exhibiting higher tensile strength, modulus, and toughness. A simple model that combines the effect of voltage and flow rate in terms of volume charge density ( $I/Q$ ) was adopted, and a linear relationship between the mean nanofiber diameter and  $(I/Q)^{-2/3}$  was found. Using this relationship the electrospinning process can be designed to produce uniform nanofibers with superior mechanical performance for achieving higher production rate of the nanofibers.

## **Chapter 5: INVESTIGATION OF RELATIVE HUMIDITY (RH) AND TEMPERATURE**

### **5.1 Introduction**

In literature various mechanisms have been envisaged to explain the formation of pores during electrospinning which could be classified into 6 main categories: (1) rapid solvent drying and breath figure formation, [110, 138] (2) temperature induced phase separation which can be considered when a polymer is dissolved in a diluent at high temperature, and then the homogeneous polymer solution is cooled to induce the phase separation, [110, 139] (3) nonsolvent induced phase separation in which electrospinning is performed with a ternary system of nonsolvent/solvent/polymer, [140, 141] (4) vapor induced phase separation [110, 121], (5) polymer/polymer phase separation in which electrospinning is performed with a solution composed of two miscible polymers and followed by leaching process to selectively remove one of components, [142] and (6) interaction of Lewis acid with the Lewis base and subsequent removal of Lewis acid component [143].

Among the above mentioned mechanisms, breath figure formation and vapor induced phase separation (VIPS) are the most relevant ones to explain the pore formation in electrospun fibers. Breath figure mechanism suggests that rapid solvent evaporation significantly cools the surface of the electrospun jet during its travel from needle to collector [144]. As the surface cools, water vapor molecules condense on the surface which grow in the form of droplets and act as hard spares. The water droplets leave imprints on the surface as the jet dries and those imprints are observed as pores. Breath

figure formations are usually found in the case of high volatile solvent. According to VIPS mechanism, when electrospinning is performed in humid condition the polymer jet is exposed to the nonsolvent, i.e. water, vapor atmosphere, which leads to diffusion of water vapor molecules into the solution, and a thermodynamic instability occurs [115, 121, 145, 146]. The thermodynamic instability is resolved by the separation of two phases such as polymer-rich phase and polymer-lean phase (Figure 5.1). Polymer-rich phase forms a solid fiber matrix, whereas polymer-lean phase creates pores. Dayal et al. [145] theoretically investigated the evolution of fiber morphology during electrospinning as a result of VIPS mechanism. According to them, nonsolvent/solvent/polymer ternary phase diagram can be used to postulate different morphologies of electrospun fiber. Pai et al. [121] demonstrated for electrospinning PS/DMF solution that the morphology of electrospun fiber is a direct consequence of competition between VIPS and two other processes such as solvent drying and bulking instability.

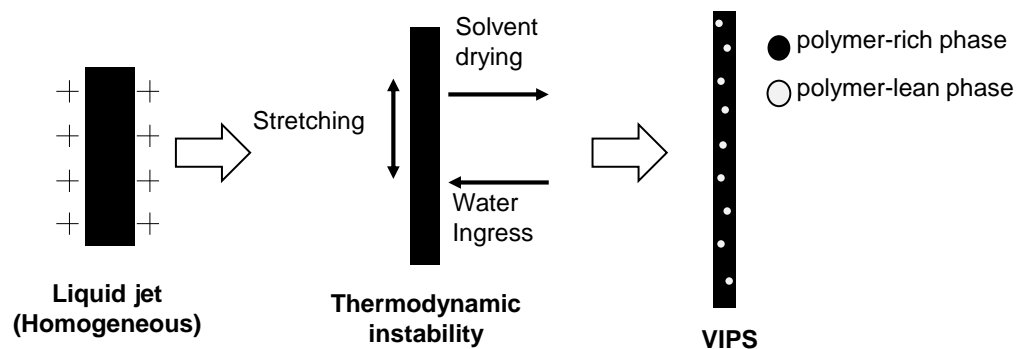


**Figure 5.1** Schematics illustrating VIPS mechanism during electrospinning.



In this study, the influence of RH and temperature on the morphology of PAN nanofibers electrospun from 10% PAN/DMF solution is investigated. The evolved morphologies are explained by the means of considering the ternary phase diagram of water/DMF/PAN. The mechanical properties of the as spun and annealed nanofiber yarns are also investigated and correlated with morphology of the internal structure and crystallinity of the nanofibers.

## 5.2 Ternary Phase Diagram

Phase diagram of ternary system water /DMF/PAN was determined by calculating the binodal and spinodal curves based on the Flory-Huggins (FH) theory for polymer solutions [147] extended to systems with three components by Tompa [148]. The Gibbs free energy of mixing ( $\Delta G_M$ ) for a ternary system is described as follows:

$$\frac{\Delta G_M}{RT} = n_1 \ln \phi_1 + n_2 \ln \phi_2 + n_3 \ln \phi_3 + n_1 \phi_2 g_{12} + n_2 \phi_3 g_{23} + n_1 \phi_3 g_{13} \quad (1)$$

where  $n_i$  and  $\phi_i$  stand for number of moles and volume fraction of the component  $i$ , respectively,  $R$  is the gas constant,  $T$  is the absolute temperature, and  $g_{ij}$  is the binary interaction parameter between component  $i$  and  $j$ . The subscripts 1, 2, and 3 refer to nonsolvent, solvent, and polymer, respectively. In this study, only binary interaction parameters were considered. Then, according to the definition of the chemical potential, three such equations hold for a ternary polymer solution as follows [148]:

$$\begin{aligned} \frac{\Delta\mu_1}{RT} = & \ln\phi_1 + 1 - \phi_1 - \frac{v_1}{v_2}\phi_2 - \frac{v_1}{v_3}\phi_3 + (g_{12}\phi_2 + g_{13}\phi_3)(\phi_2 + \phi_3) - g_{23}\frac{v_1}{v_2}\phi_2\phi_3 - \\ & u_1u_2\phi_2\left(\frac{dg_{12}}{du_2}\right) - \phi_1\phi_3^2\left(\frac{dg_{13}}{d\phi_3}\right) - \frac{v_1}{v_2}\phi_2\phi_3^2\left(\frac{dg_{23}}{d\phi_3}\right) \end{aligned} \quad (2)$$

$$\begin{aligned} \frac{\Delta\mu_2}{RT} = & \ln\phi_2 + 1 - \phi_2 - \frac{v_2}{v_1}\phi_1 - \frac{v_2}{v_3}\phi_3 + \left(g_{12}\frac{v_2}{v_1}\phi_1 + g_{23}\phi_3\right)(\phi_1 + \phi_3) - \\ & g_{13}\frac{v_2}{v_1}\phi_1\phi_3 + u_1u_2\frac{v_2}{v_1}\phi_1\left(\frac{dg_{12}}{du_2}\right) - \frac{v_2}{v_1}\phi_1\phi_3^2\left(\frac{dg_{13}}{d\phi_3}\right) - \phi_2\phi_3^2\left(\frac{dg_{23}}{d\phi_3}\right) \end{aligned} \quad (3)$$

$$\begin{aligned} \frac{\Delta\mu_3}{RT} = & \ln\phi_3 + 1 - \phi_3 - \frac{v_3}{v_1}\phi_1 - \frac{v_3}{v_2}\phi_2 + \left(g_{13}\frac{v_3}{v_1}\phi_1 + g_{23}\frac{v_3}{v_2}\phi_2\right)(\phi_1 + \phi_2) - \\ & g_{12}\frac{v_3}{v_1}\phi_1\phi_2 + \left[\frac{v_3}{v_1}\phi_1\left(\frac{dg_{13}}{d\phi_3}\right) + \frac{v_3}{v_2}\phi_2\left(\frac{dg_{23}}{d\phi_3}\right)\right]\phi_3(\phi_1 + \phi_2) \end{aligned} \quad (4)$$

where  $\Delta\mu_i$  denotes the difference between the chemical potential of component  $i$  in the mixture and pure state;  $v_i$  is the molar volume of component  $i$ ;  $u_1 = \phi_1/(\phi_1 + \phi_2)$ , and  $u_2 = \phi_2/(\phi_1 + \phi_2)$ . Based on the definition of the binodal curve, the chemical potential of the polymer-rich phase and that of the polymer-lean phase reach equilibrium, hence there exist equations as follows:

$$\Delta\mu_{i,A} = \Delta\mu_{i,B} ; i = 1,2,3 \quad (5)$$

where the subscript A and B stand for polymer-rich and polymer-lean phases, respectively. In addition, the components in the two phases obey the material conservation law:

$$\sum \phi_{i,A} = \sum \phi_{i,B} = 1 ; i = 1,2,3 \quad (6)$$

Eq. 5 and Eq. 6 include five coupled nonlinear equations with six unknowns:  $\emptyset_{1,A}$ ,  $\emptyset_{2,A}$ ,  $\emptyset_{3,A}$ ,  $\emptyset_{1,B}$ ,  $\emptyset_{2,B}$ ,  $\emptyset_{3,B}$ . By choosing one variable (in this study,  $\emptyset_{3,A}$  was chosen) independent, others can be determined with a set of interaction parameters.

The spinodal curve of a ternary system satisfies the following equation [148]:

$$G_{22} \cdot G_{33} = (G_{23})^2 \quad (7)$$

$$\text{where } G_{ij} = \frac{\partial^2 \Delta G_M}{\partial \emptyset_i \partial \emptyset_j}$$

It follows, using Eq. 1

$$G_{22} = \frac{1}{\emptyset_1} + \frac{v_1}{v_2 \emptyset_2} - 2g_{12} + 2 \left( \frac{dg_{12}}{du_2} \right) (u_1 - u_2) + \left( \frac{d^2 g_{12}}{du_2^2} \right) u_1 u_2 \quad (8)$$

$$G_{33} = \frac{1}{\emptyset_1} + \frac{v_1}{v_3 \emptyset_3} - 2g_{13} - 2 \left( \frac{dg_{12}}{du_2} \right) u_2^2 (1 - u_1) + \left( \frac{d^2 g_{12}}{du_2^2} \right) u_1 u_2^3 \quad (9)$$

$$G_{23} = \frac{1}{\emptyset_1} - (g_{12} + g_{13}) + \frac{v_1 g_{23}}{v_2} + \left( \frac{dg_{12}}{du_2} \right) u_2 (u_1 - 2u_2) + \left( \frac{d^2 g_{12}}{du_2^2} \right) u_1 u_2^2 \quad (10)$$

Still, the components of the ternary system obey the material conservation law:

$$\sum \emptyset_{i,A} = 1 \quad ; \quad i = 1,2,3 \quad (11)$$

Eq. 7 and Eq. 11 include two coupled nonlinear equations with three unknowns:  $\emptyset_1$ ,  $\emptyset_2$ ,  $\emptyset_3$ . Again, by choosing one variable (e.g.  $\emptyset_1$ ) independent, the spinodal curve can be obtained.

To construct a phase diagram numerically, binary interaction parameters of nonsolvent/solvent, solvent/polymer, and nonsolvent/polymer are necessary.  $g_{12}$  in Eq. 1 is a generalized nonsolvent/solvent interaction function depending on the volume fraction,  $u_2$  of a pseudo binary mixture [149, 150]. The data set of the binary interaction parameters of water /DMF binary systems at 20°C and 40°C were collected from literatures [151] and presented based on Koningsveld and Kleintjens model [152] (Eq. 12).

$$g_{12}(\phi_2) = \alpha + \frac{\beta}{1-\gamma\phi_2} \quad (12)$$

where  $\alpha$ ,  $\beta$ , and  $\gamma$  are temperature-dependent constants.

$g_{13}$  and  $g_{23}$  are the nonsolvent/polymer and solvent/polymer interaction parameters, respectively, often assumed to be temperature dependent but concentration independent [153-155]. The water/PAN interaction parameter ( $g_{13}$ ) can be evaluated by equilibrium swelling method [154, 155]. Dong et al. [155] determined water/PAN interaction parameter as a function of temperature, from where  $g_{13}$  were adopted for 20°C and 40°C. There are many approaches to determine the solvent/polymer (DMF/PAN) interaction parameter, such as light scattering, gas-liquid equilibrium, and osmotic pressure [156, 157]. The data set of binary interaction parameters ( $g_{23}$ ) of DMF/PAN binary system were collected from literature [158].

Knowing the interaction parameters between three components at 20°C and 40°C, the binodal and spinodal curves at respective temperatures were calculated with the help of

Lsqnonlin function in Matlab. More details of the mathematical/numerical treatment can be found elsewhere [150].

## **5.3 Experimental**

### ***5.3.1 Electrospinning Process***

The 10% PAN in DMF (by weight) solution was electrospun at 15 kV. The distance between the tip of the needle and the surface of the disk was constant at 18 cm. The flow rate of the solution to the needle tip was maintained so that a stable Taylor cone remains during electrospinning. The RH conditions and temperatures inside the chamber were regulated using dried silica and atomized water spray, and a heater along with a temperature controller, respectively. A fan was used inside the chamber to attain homogenous RH and temperature. However, the fan was turned off during electrospinning process to avoid any disturbance. Once the system reached to the desired condition, electrospinning was performed while the disc was rotating at 600 rpm. The RH level and temperature were closely monitored during the entire time of the electrospinning. Yarns were produced at 20<sup>±1</sup>°C under six humidity conditions such as 14<sup>±2</sup>%, 22<sup>±1</sup>%, 30<sup>±1</sup>%, 40<sup>±2</sup>%, 50<sup>±2</sup>%, and 60<sup>±2</sup>% RH, and at 40<sup>±2</sup>°C under two humidity conditions such as 30<sup>±2</sup>% and 40<sup>±3</sup>% RH. If the variation in RH level and temperature were higher than the tolerance limit mentioned above, the yarn was discarded and a new yarn was made. The total amount of solution electrospun was about 200 μL. The electrospun nanofiber bundles were peeled off the copper foil in the form of yarn and then mounted on a drying rack to keep them in tension. All the yarns were dried at 60°C

for 12 h under vacuum. For annealing purpose, yarns were heat treated at 95°C for 4 h while they are still mounted on the drying rack.

### ***5.3.2 Characterization Techniques***

The surface morphology along with the cross-section of the electrospun nanofiber was observed by Zeiss Neon high resolution SEM. Liquid nitrogen was used to freeze fracture the nanofiber to examine the cross-section. Samples were coated with 4 nm layer of Iridium before SEM. Based on the SEM images, diameter of electrospun nanofiber was determined by using Image J. At least 50 fibers were measured to obtain the mean and standard deviation values of the diameter. Fiber current (I) was measure by placing a multimeter between the collector and the ground. DMA Q800 from TA Instruments was utilized to perform the tensile experiments. All the tensile tests were performed at room temperature with a sample gauge length of 9-10 mm and a constant strain rate of 0.001 s<sup>-1</sup>. The cross-sectional area of the yarn was calculated by dividing the mass of the yarn by its length and the density of PAN (1.18 g/cc).

Wide angle X-ray diffraction (WAXD) patterns of the yarns were obtained by a Rigaku pinhole collimation SAXS system with scattering vector range between 0.07-1.59 nm<sup>-1</sup>. All the samples were initially mounted on rectangular plate sample holders with round holes in the center. The sample itself was held on the sample holder using scotch tape so that the sample went across the opening. The scattered radiation was gathered on a Kodak film. After baseline subtraction, the crystalline and the amorphous halo were fitted, using a program written in Excel VBA. The WAXD program can be found in ref.

159. Schematic illustrations of WAXD spectra analysis for as-spun and annealed nanofibers are shown in Figure 5.2. XRD crystallinity was calculated by dividing the area under the crystalline peaks by the total area under the curve:

$$\%_{crystallinity} = \frac{A_{c1} + A_{c2}}{A_{c1} + A_{c2} + A_a} * 100$$

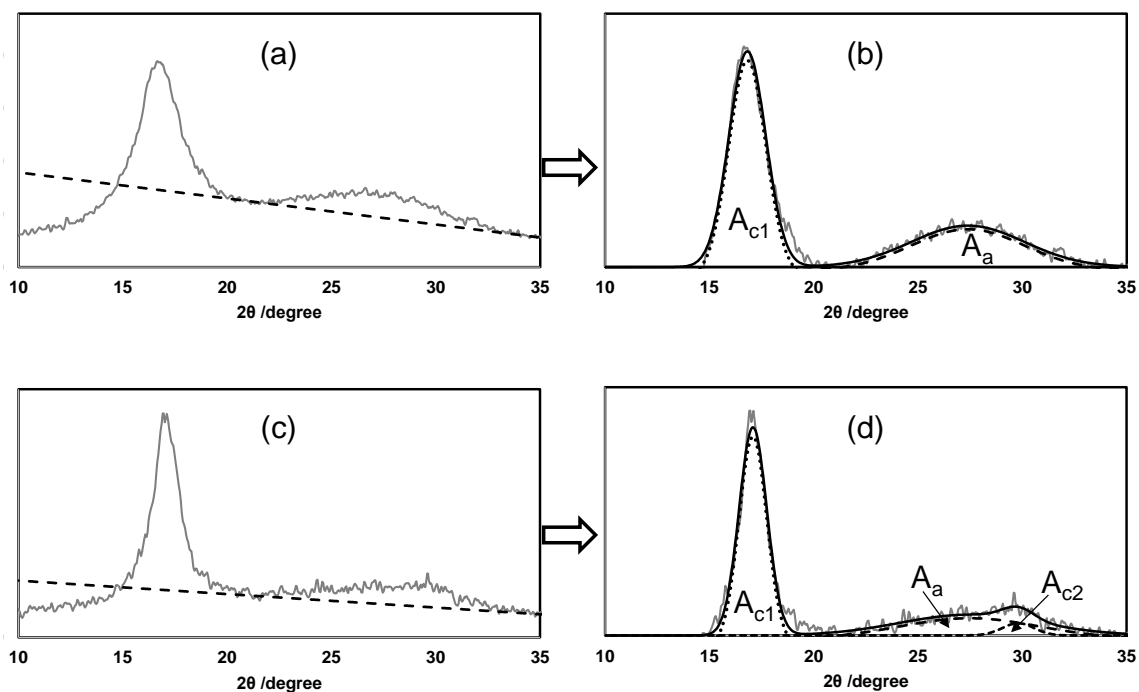


**Figure 5.2** Schematics illustrating WAXD spectra analysis for (a-b) as-spun and (c-d) annealed nanofibers.

## 5.4 Results and Discussion

In electrospinning, the liquid jet experiences continuous stretching force due to electrostatic force while travelling from needle to collector. During the travel, solvent drying as well as uptake of water vapor molecules from the surrounding environment occurs. Both of these phenomena contribute to increase the free energy of polymer solution jet which is not thermodynamically favorable and causes the system to be instable [115, 160]. However, this instability can be ceased by separation into two phases, such as, solvent-rich phase and polymer-rich phase. The polymer-rich phase makes the polymeric matrix in which the former is dispersed. Depending on the experimental conditions two possible mechanisms can be attributed to phase separation, such as nucleation and growth (NG) and spinodal decomposition (SD) [160]. NG leads to isolated pores whereas interconnected network of pores are created as a result of SD. The phase behavior of a homogenous polymer solution exposed to a nonsolvent vapor, called as VIPS, can be described in terms of thermodynamic interactions of the components which can be visualized by ternary phase diagram [115, 161].

**Table 5.1** Interaction parameters required to calculate ternary phase diagram of water/DMF/PAN system.

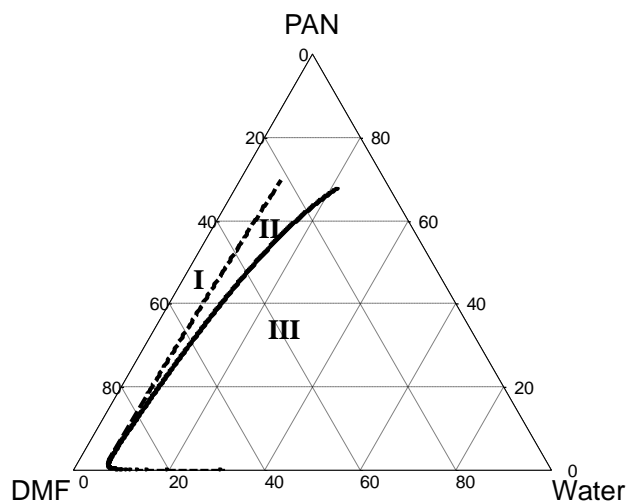
Temperature	$g_{12}(\phi_2) = \alpha + [\beta/(1 - \gamma\phi_2)]^a$	$g_{13}^b$	$g_{23}^c$
20°C	$0.218 + [0.276/(1 + 0.622\phi_2)]$	1.65	0.280
40°C	$0.425 + [0.0619/(1 - 0.9494\phi_2)]$	1.35	0.292

<sup>a</sup> Data taken from ref 151. <sup>b</sup> Data taken from ref 155. <sup>c</sup> Data taken from ref 158.

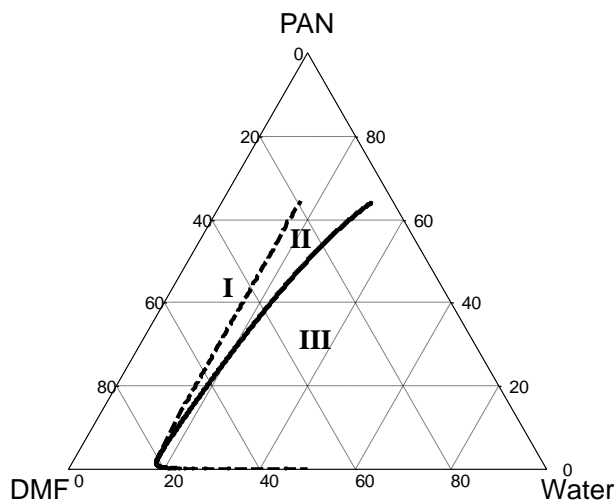


#### ***5.4.1 Construction of Ternary Phase Diagram for Water/DMF/PAN System***

Two sets of interaction parameters for water/DMF/PAN system at 20°C and 40°C, required for constructing the phase diagram, are tabulated in Table 5.1. Note that, DMF/PAN interaction parameter, ( $g_{23}$ ) at 40°C was interpolated between the reported values at 35°C and 50°C [158]. Figure 5.3 shows the theoretical ternary phase diagrams for water/DMF/PAN system at 20°C and 40°C.



(a)



(b)

**Figure 5.3** Ternary phase diagram of water/DMF/PAN system at (a) 20°C and (b) 40°C. Included in the diagrams are the binodal curves (dashed line) and spinodal curves (solid lines). Three regions in the diagrams are homogeneous (I), metastable (II), and unstable (III) regions.

As illustrated, the ternary phase diagram is divided into three regions by the binodal and spinodal curves, respectively. Region I is the homogenous domain, also called as miscible region. Regions II and III are the metastable and unstable regions, respectively.

The mechanisms through which phase separation proceeds are different for these regions. In the metastable region, liquid-liquid demixing is governed by NG, while SD is dominant in unstable region. Comparison of the phase diagrams at 20°C and 40°C reveals that they exhibit significant difference in miscibility area (region I). Higher temperature shifts the binodal curve toward the nonsolvent-polymer axis which is due to the differences in the binary interaction parameters of the components in the mixture.

#### ***5.4.2 Surface Morphology of Electrospun Nanofibers***

##### *5.4.2.1 Effect of RH*

Figure 5.4 shows the SEM images taken from the surface of nanofibers electrospun under atmospheres of temperature 20°C and varying RH. One can witness the impression of solvent on surface as well as variation in fiber diameter. Changing fiber diameter with RH will be discussed in section 5.4.4.3. At low RH (14% and 22%) electrospinning led to fiber of almost texture-less smooth surface (Figure 5.4a, b). Although no pores were formed on fiber surface at 14% RH, few isolated pores were observed on the surface of larger diameter fibers at 22% RH. By increasing RH, the smooth surface of electrospun fibers was replaced by irregular surface morphology which is an increasing function of RH. When electrospinning was performed at 14% RH, phase separation did not contribute to the morphology of resultant fibers and led to smooth surface (Figures 5.4a). This corresponds to the mass transfer path for 14% RH did not cross the binodal curve. At this condition, the morphology of fiber is dominantly determined by solvent drying phenomena. Increasing the RH reduces time of phase separation and creates small pores on the fiber surface due to the mass transfer path

crossing the binodal curve. At 22% RH, the mass transfer path of smaller diameter fibers did not cross the binodal curve, whereas it barely crossed the binodal curve for the larger diameter fibers and occasional small pores were formed on the surface due to phase separation. Larger fiber takes longer time to dry, hence, more water molecules can be absorbed which brings the mass transfer path cross the binodal curve. Fibers electrospun at 30% and higher RH (Figures 5.4c-f) experienced high asperities on their surfaces resembling bicontinuous structure which is characteristics feature of SD mechanism. It can be said that the track through which composition of these fibers changed, passed probably from the metastable region and ended in the unstable region of the phase diagram. Thus the isolated pores were replaced by cocontinuous interconnected network of pores on the surface of fibers. Considering non-volatile behavior of DMF and the starting composition of the spinning solution (10% PAN in DMF) being very close to the solvent-nonsolvent axis (Figure 5.3a), where the metastable region is very small, passing the spinodal curve is not wondering.

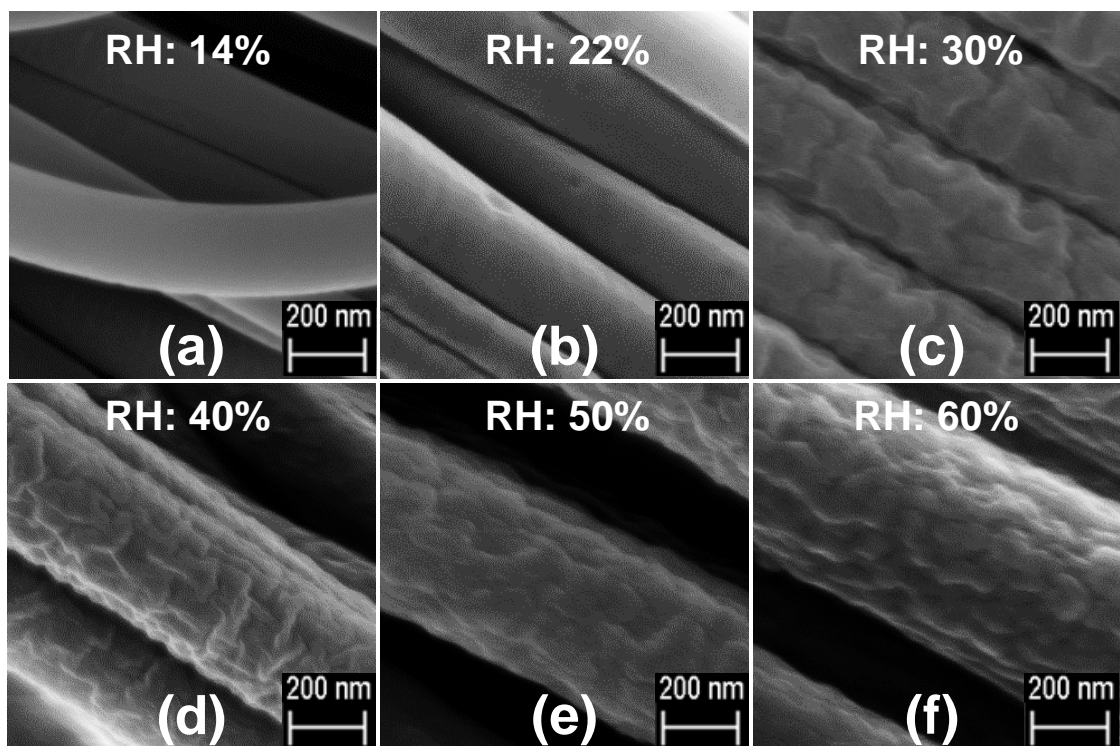


**Figure 5.4** Surface morphology of as-spun PAN nanofibers electrospun at 20°C under various RH conditions.

#### 5.4.2.2 Effect of Temperature

Temperature is believed to influence the morphology of electrospun fibers by affecting the electrospinning atmosphere, the miscibility area (Figure 5.3), and the rate of mass transfer across the interface between solution jet and gaseous phase. To study the effect of temperature on the surface morphology of the electrospun fiber, electrospinning were performed at 40°C under two humidity conditions such as 30% and 40% RH. Figure 5.5 shows the SEM images of surfaces of PAN nanofibers electrospun at 40°C. Neither isolated pores nor bicontinuous network of pores were found on the surface of fibers electrospun at 30% RH. However, little unevenness was observed on the surface which

is the impression left by solvent after drying. Thus, no phase separation occurred during electrospinning at 40°C-30% RH, whereas phase separation was observed under same humidity condition at 20°C (Figure 5.4c). However, phase separation did occur at 40°C when RH was increased to 40%. Thus it can be said that, morphology transition from smooth to rough surface occurs at certain RH, which shifts to higher value if the process temperature goes up. Increasing the temperature of the electrospinning process increases the amount of water can be dissolved into the polymer solution without phase separation meaning expansion of the miscibility area in phase diagram (Figure 5.3). Thus, a delayed phase separation can be adopted for the solution electrospinning at higher temperature. At 40°C-30% RH, water absorbed by the electrospinning jet was not high enough to induce phase separation, while at 20°C, such level of RH can produce cocontinuous interconnected network of pores on the surface of fibers, by bringing the mass transfer path passed the binodal and spinodal curves of the ternary phase diagram. By careful observation it can be noticed that the surface of fibers electrospun at 40°C-40% RH was much rougher than the surface of those electrospun at 20°C-40% RH. This could be due to longer wait time before the mass transfer path crosses the spinodal, owing to the larger miscibility area in ternary phase diagram at 40°C, which allows the fiber to absorb more water molecule and consequently brings more roughness after phase inversion takes place.

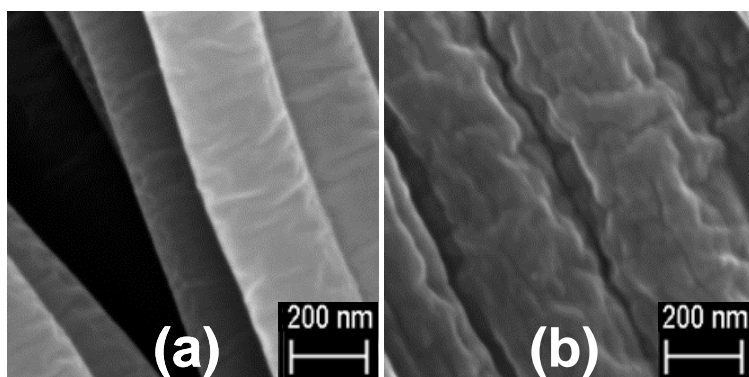


**Figure 5.5** Surface morphology of as-spun PAN nanofibers electrospun at 40°C under (a) 30% RH and (b) 40% RH.

#### *5.4.2.3 Effect of Annealing*

Figure 5.6 shows the surface morphology of PAN nanofibers electrospun under various environmental conditions, after annealing. It illustrates the diminishment of surface porosity and alleviation of the surface roughness when compared with as-spun fibers. The reduction in surface roughness also makes cocontinuous network more perceptible in annealed fibers. Annealing permits the fibers to reduce the surface energy by smoothing out the roughness and, as shown later in sections 5.4.3.2 and 5.4.4.3, also influences the internal morphology and diameter of fibers.

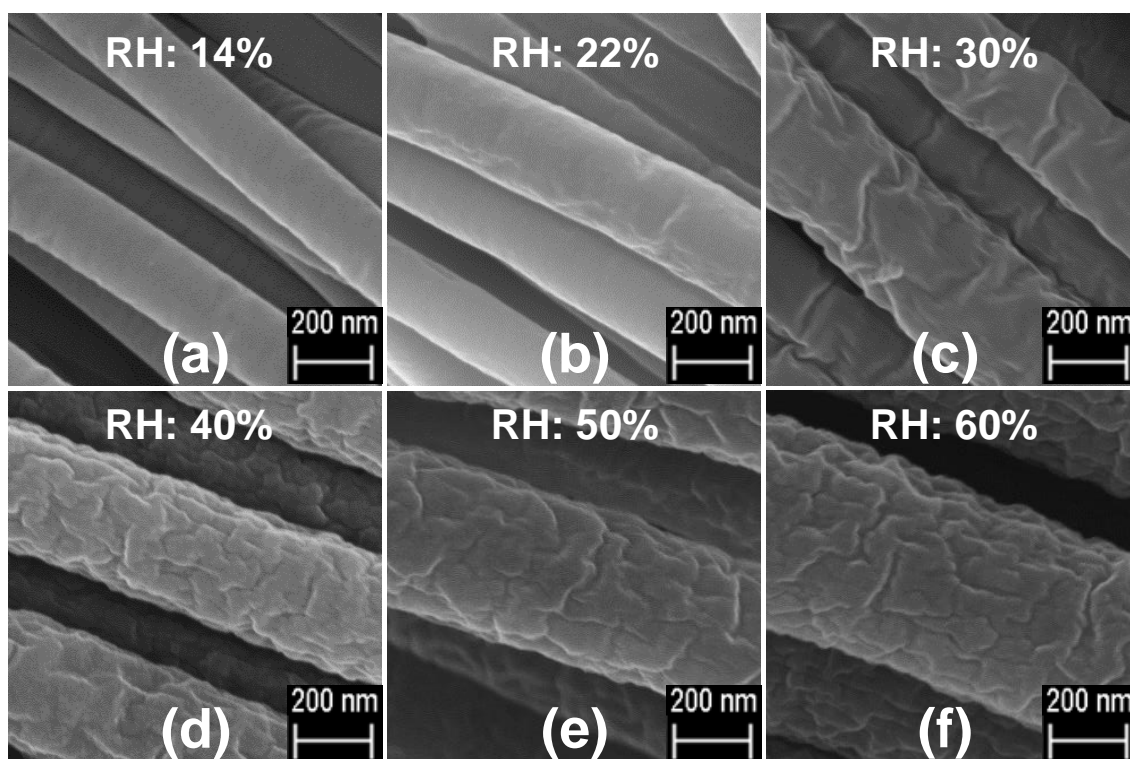


**Figure 5.6** Surface morphology of annealed PAN nanofibers electrospun at 20°C under various RH conditions.

### 5.4.3 Interior Structure of Electrospun Nanofibers

#### 5.4.3.1 Effect of RH and Temperature

Figure 5.7a-d represents the micrograph of the fractured cross-section of PAN nanofibers electrospun at 20°C under various RH conditions. Two types of interior morphology such as nonporous (Figure 5.7a) and porous (Figure 5.7b-d) can be distinguished from the figures. At 60% RH, the highest RH in this study, nanofibers exhibited porous structure with pore-connectivity. The interior porosity of the fibers decreased with the reduction of RH. The polymer phase also became coarse as the RH humidity decreased and eventually a dense interior structure was developed at 22% RH.



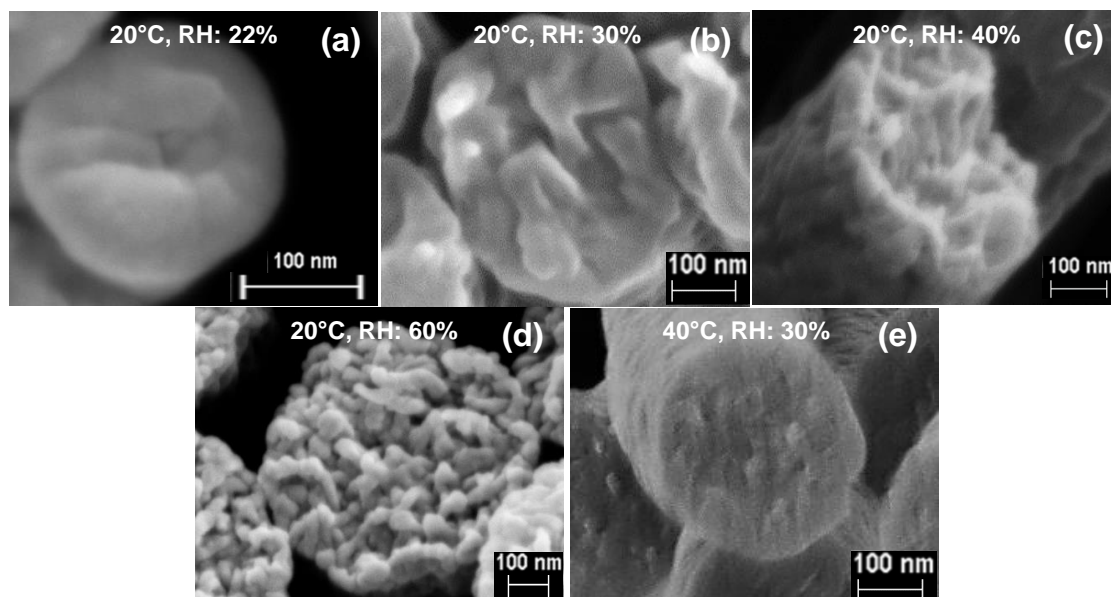


**Figure 5.7** Cross-sectional micrographs of as-spun PAN nanofibers electrospun under various environmental conditions.

Once the electrospinning jet flights from the needle, it is exposed to the humid air, and exchanging solvent and nonsolvent through the interface between polymer solution and humid air begins. With increasing the nonsolvent concentration in the polymer jet the mass transfer path moves away the polymer-solvent axis, while solvent drying makes it moves away the solvent-nonsolvent axis. Hence, depending on the nonsolvent concentration, which is RH, the mass transfer path crosses the binodal curve or not. If the mass transfer path does not cross the binodal curve and ends up into the miscibility region, the surface as well as the interior structure does not exhibit porosity. Once, the composition crosses the binodal curve, polymer solution becomes thermodynamically unstable, bringing the composition of the electrospinning jet into the metastable region

where polymer-rich and polymer-lean domains are emerged. The former makes the polymer matrix while the latter develops eventually into pores. However, the porosity is restricted to the surface or becomes a part of the interior skeleton depends on whether the composition path passes the spinodal curve or not. If the composition path ends up into the metastable region and does not cross the spinodal curve, the porosity can only be found on the surface and does not contribute to the interior structure. But once the composition path crosses the spinodal curve, phase inversion occurs by the means of SD mechanism which permits interior porosity. Thus, electrospinning at 20°C under RH condition of 30% or higher, the mass transfer path must have crossed the spinodal path of the ternary phase diagram which was also confirmed from surface morphology. Electrospinning at 40°C-30% RH also produced dense internal structure, as shown in Figure 5.7e, which is expected as no phase demixing occurred for these fibers, as discussed in section 5.4.2.2.

#### *5.4.3.2 Effect of Annealing*

The micrographs of the interior structure of the annealed fibers electrospun at two different environmental conditions are shown in Fig. 5.8. Annealing was found to affect the internal structure of the fibers when compared with the as-spun fibers (Fig. 5.7c, d). The internal porosity of the fibers decreased due to annealing.

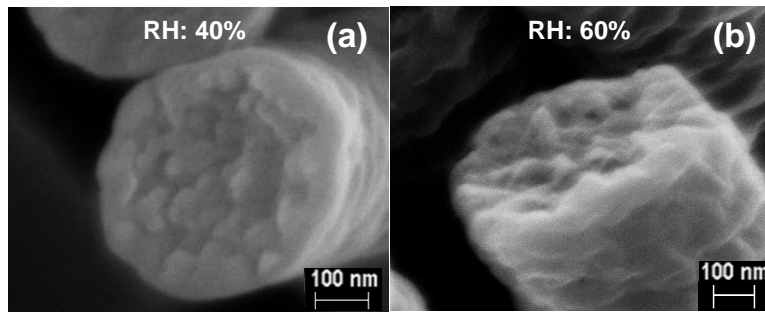


**Figure 5.8** Cross-sectional micrographs of annealed PAN nanofibers electrospun at 20°C under various RH conditions.

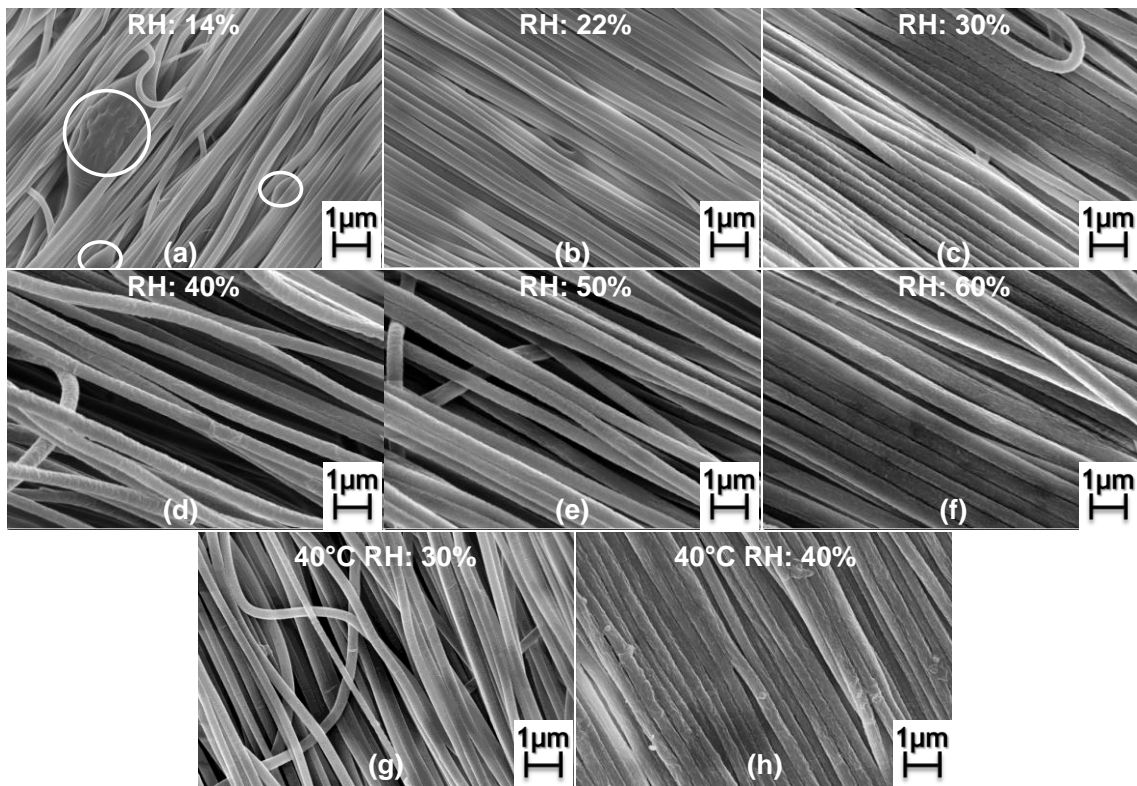


**Figure 5.9** Surface morphology (at low magnification) of as-spun PAN nanofibers electrospun at 20°C (a-f) and 40°C (g, h). Circles in (a): beads.

#### ***5.4.4 Bead Formation and Diameter Distribution of Electrospun Nanofibers***

SEM images of nanofibers at low magnification are shown in Figure 5.9. At low humidity (14% RH) elongated irregularly shaped beads as well as smaller diameter fibers were found. With increasing the RH value to 22% and more, beadless fibers were generated which varied in diameter.

##### ***5.4.4.1 Mechanism of Bead Formation***

Capillary instability has been demonstrated in literature [84, 94] as the dominating factor for bead evolution in electrospinning. This event emerges from surface tension of polymer solution and must be prevented to stabilize fiber formation. It has been demonstrated that this type of instability can be effectively suppressed by viscoelastic stress [115]. During electrospinning at higher humidity, penetration of water into the polymer solution jet raises the thermodynamic instability and evaporation of the solvent increases the polymer concentration of jet. Both events lead to increase in viscoelastic forces and eventually prevent the capillary instability which is responsible for bead formation. On the other hand, at low humidity (e.g. 14% RH), the amount of water diffuse into the polymer jet is very small, causing a delayed solidification and resulting in capillary instability to overcome the viscoelastic stress, which causes beads to form.

##### ***5.4.4.2 Mechanism of Pores on Beads***

A close observation of the beads (Figure 5.10a) produced at 14% RH reveals small pores on the surface of larger beads which means the composition path for these beads probably crossed the binodal curve and ended into the metastable region. The possible composition path for the fibers and beads are shown by solid line arrows 1 and 2 in

Figure 5.10b, respectively. Note that, showing composition paths by straight lines is just for the sake of argument. Once beads are formed large amount of solvent (DMF) is entrapped under the surface which makes it longer for the beads to completely dry. This allows enough time for sufficient water molecule precipitation on the surface which brings the composition path into the metastable state, and consequently, creates pores on the surface.

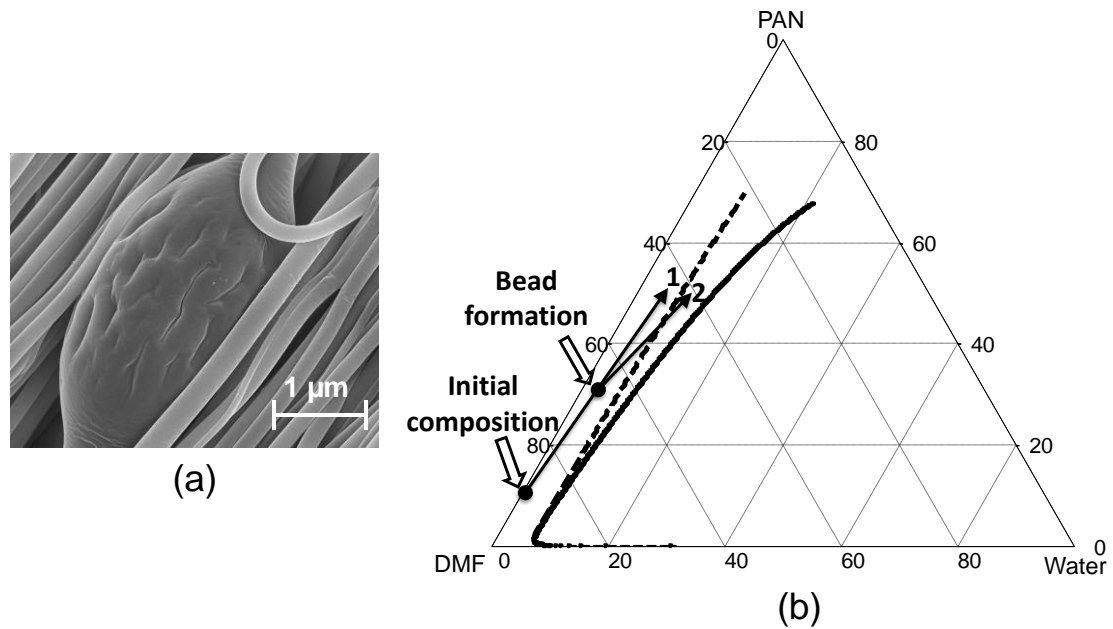


**Figure 5.10** (a) Surface characteristics of large beads formed during electrospinning of 10% PAN/DMF solution at 20°C and 14% RH. (b) Possible composition paths for fibers (arrow 1) and beads (arrow 2) shown in (a). Dashed line: binodal curve, solid line: spinodal curves. I, II, and III are indicating homogeneous, metastable, and unstable regions, respectively.

#### *5.4.4.3 Effect of RH, Temperature and Annealing on Fiber Diameter*

The variation in average nanofibers diameter with RH, temperature, and annealing is shown in Figure 5.11. It can be seen that increasing RH produced nanofibers with higher diameter. Increment of the nanofiber diameter can be explained by considering the rate of phase demixing. At higher humidity, more water is diffused into the polymer solution jet, causing the phase demixing to happen at a faster rate. This event accelerates the solidification of the fiber. Hence, further stretching of the electrospinning jet as a consequence of whipping instability is ceased and thick fibers are produced. Temperature has significant effect on the diameter of fibers which also depends on whether fibers experience phase demixing or not. At 40°C-30% RH, no phase demixing resulted in lower diameter fiber than those electrospun at 20°C-30% RH. In contrast, no significant difference was observed at 40% RH due to temperature difference. Effect of annealing was not observed at low humidity as no porosity was observed in the internal structure of the fibers. With increasing RH, diameter of the fibers appeared to be reduced at an increasing rate after annealing, as annealing reduce the porosity of the internal structure of the fiber.

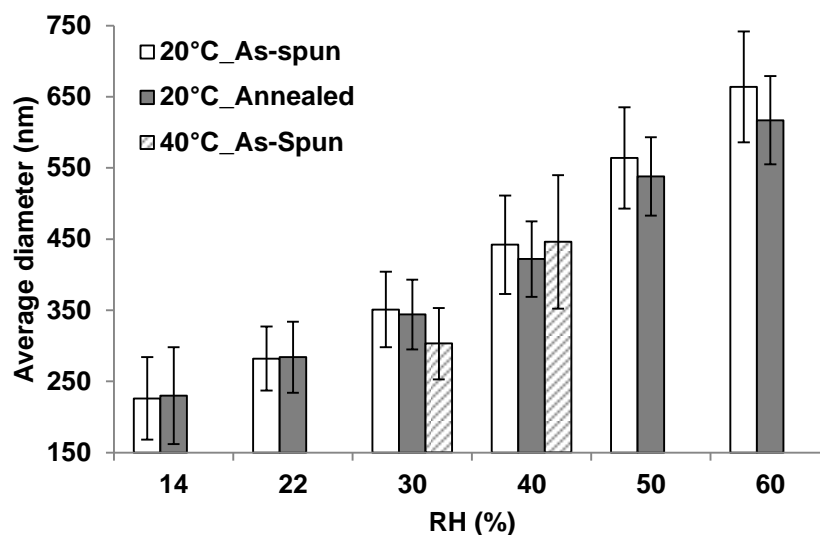


**Figure 5.11** Influence of RH, temperature and annealing on the average nanofiber diameter of nanofibers electrospun from 10% PAN/DMF solution.

#### 5.4.4.4 Isolation of Two Mechanisms for Diameter Variation

Although, phase demixing has great impact on the nanofiber diameter, another important factor, as discussed in Chapter 4, is volumetric charge density of the polymer solution jet. It is considered as the strength of the electrostatic force acting on the jet. The influence of RH on volumetric charge density of electrospinning jet at 20°C is shown in Figure 5.12. The volumetric charge density of the electrospun jet found to be decreased with increasing RH. Higher RH means presence of more water molecules in the electrospinning chamber, which reduces the excess charges on the electrospinning jet due to molecular polarization, consequently decreases the volumetric charge density of the electrospun jet.

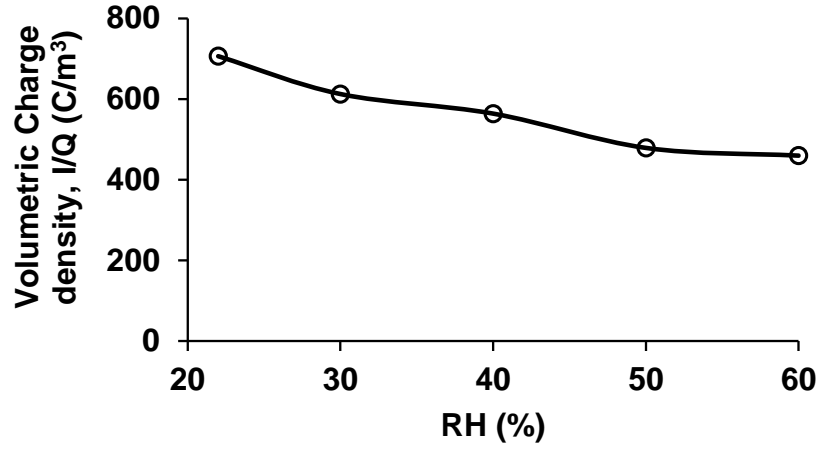


**Figure 5.12** Influence of RH on volumetric charge density of electrospinning jet.

Fridrikh et al. [135] developed a simple model to predict the fiber diameter by analyzing the dynamic equations, describing the motion of whipping jet, of Hohman [136, 137]. Evaluating the asymptotic balance between normal stresses due to surface tension and surface charge repulsion, they obtained:

$$d_{\text{fiber}} = c^{1/2} \left( \gamma \epsilon \frac{Q^2}{I^2} \frac{2}{\pi(2 \ln \chi - 3)} \right)^{1/3} \quad (13)$$

where  $c$  is the polymer concentration;  $\gamma$  is the surface tension (N/m);  $\epsilon$  is the dielectric constant of ambient air;  $Q$  is the flow rate ( $\text{m}^3/\text{s}$ );  $I$  is the measured fiber current (A);  $\chi$  is the dimensionless wavelength of the instability response for the normal displacements. Surface tension is a function of temperature and dielectric constant of air varies very slowly ( $2\sim 4 \times 10^{-4}\%$ ) with RH. Thus, at a constant temperature Eq. 13 can be reduced to,



$$d_{\text{fiber}} = \text{Constant} * \left(\frac{I}{Q}\right)^{-2/3} \quad (14)$$

In Eq. 14,  $d_{\text{fiber}}$  is a limiting (minimum) diameter which arises from the balance between normal stresses due to surface tension and surface charge repulsion; diffusion of nonsolvent (in our case water) molecule from the electrospinning environment into the solution jet may cause phase separation leading to arrest the jet prematurely with larger diameter. As discussed in section 5.4.2.1, fiber produced at 22% RH barely experienced phase separation; it can be assumed that 22% RH obey Eq. 14, and based on this the effect of volumetric charge density on nanofibers diameter alone can be predicted by considering no solidification takes place due to phase demixing. Table 5.2 represents the predicted nanofibers diameter based on volumetric charge density by keeping all the other parameters constant, actual nanofiber diameter, and difference between actual and predicted diameters for the fibers electrospun at 20°C. A graphical representation is also shown in Figure 5.13. The difference between actual diameter, and expected diameter based on volumetric charge density increased with increasing RH. This further confirms higher rate of phase demixing at higher RH which brings the electrospun jet to solidification stage much earlier, and consequently, thicker nanofibers are produced.

**Table 5.2** Isolating the effect of volumetric charge density and phase demixing on the average diameter of nanofibers electrospun at 20°C.

RH (%)	Expected average nanofiber diameter based on volumetric charge density, $d_{\text{predicted}}$ (nm)	Actual average nanofiber diameter, $d_{\text{actual}}$ (nm)	$d_{\text{actual}} - d_{\text{predicted}}$ (nm)
22	282	282	0
30	310	351	41
40	328	442	114
50	365	564	199
60	375	664	289

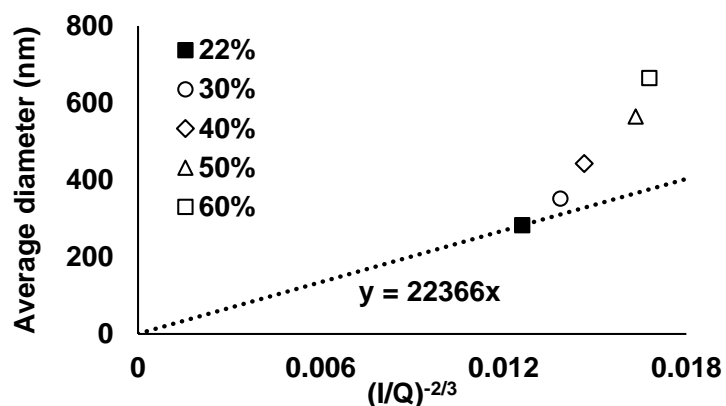


**Figure 5.13** A graphical representation of difference between expected nanofiber diameter based on volumetric charged density (shown by straight line) and experimental diameter.

It should be noted here that, at very high RH such as 20°C-70% RH, the deposited fibers did not stay on the surface of the collector and found to be coming off every few seconds. Fast solidification of the fiber slows down the drying process of the fiber by

reducing surface to volume ratio, which eventually causes the deposited fiber to still have a good amount of solvent and nonsolvent in the structure. Thus, the mass of the fiber electrospun at 70% RH was high enough to generate sufficient centrifugal force at 600 rpm to overcome the adhesive force between fibers.

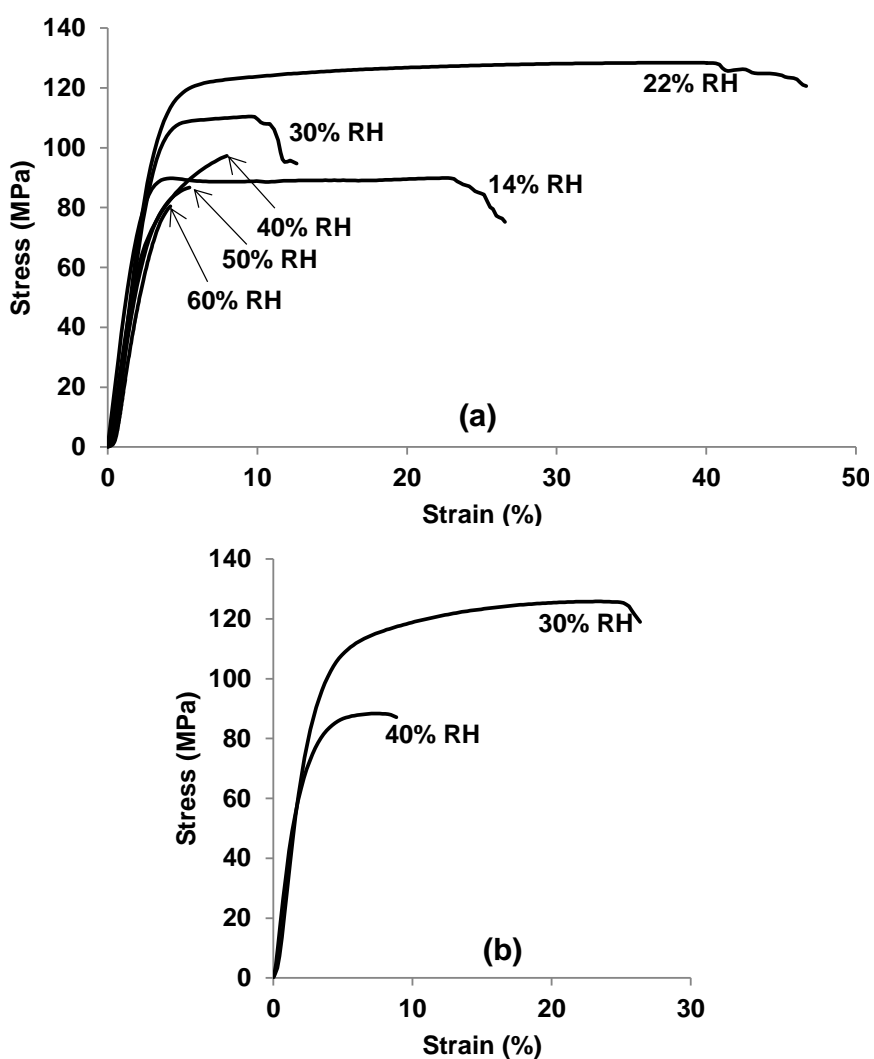


**Figure 5.14** Representative stress-strain curves for PAN nanofiber yarns electrospun at (a) 20°C and (b) 40°C under various RH conditions.

## ***5.4.5 Mechanical Properties of Electrospun Nanofiber Yarns***

### ***5.4.5.1 Effect of Humidity and Temperature***

Representative stress-strain curves for as-spun yarns are shown in Figure 5.14. Tensile strength was found to be lowest for yarn produced at highest RH and increased as humidity decreased. The increase in strength can be attributed to the reduction in average nanofiber diameter with decreasing humidity. However, yarns produced at 20°C-14% RH did not exhibit further increase in strength despite having lowest average nanofiber diameter. This could be due to the formation of beads which act as defects in the yarn. Moreover, beads contribute to the cross-section, which is calculated based on the mass of yarn, used for stress calculation but do not take any additional load which deceptively shows lower strength of the yarns produced at 14% RH.

Another important feature to be noted that, yarns produced at 22% RH also exhibited pronounced elasto-plastic behavior with large deformation to failure whereas those produced at higher humidity do not (Figure 5.14a). A massive reduction in strain at break (47% to 11%) of the yarns was observed when RH was increased from 22% to 30%. These could be due to either huge increase in crystallinity or defects in the structure of the nanofibers produced at 30% RH. WAXD was performed to investigate the crystallinity of the nanofibers. The X-ray diffraction patterns along with calculated fractional crystallinity are shown in Figure 5.15. No significant difference (1%) in crystallinity between nanofibers produced at 22% and 30% RH was observed that it could be accounted for such a big reduction in toughness ( $56.2 \text{ MJ/m}^3$  to  $11.5 \text{ MJ/m}^3$ ) (Figure 5.14). Thus, it can be concluded that the reduction in strain in break or

toughness is due to the defects presence in the structure of the nanofiber. Nanofibers produced at higher RH undergo phase demixing which creates pores in the internal structures of the fibers. These pores act as stress concentration sites during tensile loading and cause the fibers to fail early. Due to the same reason, nanofibers electrospun at 40°C-30% RH exhibited high strength owing to their solid internal structure, whereas those electrospun at 40°C-40% RH were weaker because of porous structure. However, toughness of the yarns produced at 40°C-30% RH shows lower strain in break than those produced at 20°C-22% RH despite of both having solid internal structure. This could be due to 5% increase in crystallinity, as shown in Figure 5.15.

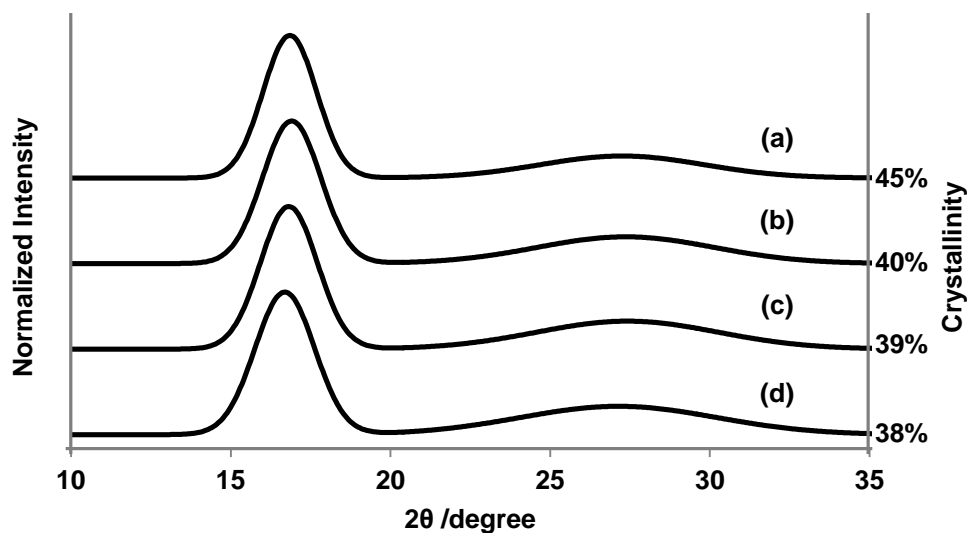


**Figure 5.15** Integrated WAXD plots and calculated percentage crystallinity of as-spun PAN nanofiber yarns electrospun at (a) 40°C-30% RH, (b) 20°C-22% RH, (c) 20°C-30% RH, and (d) 20°C-60% RH. Intensity profiles of integrated scans are shifted upward for clear comparison.

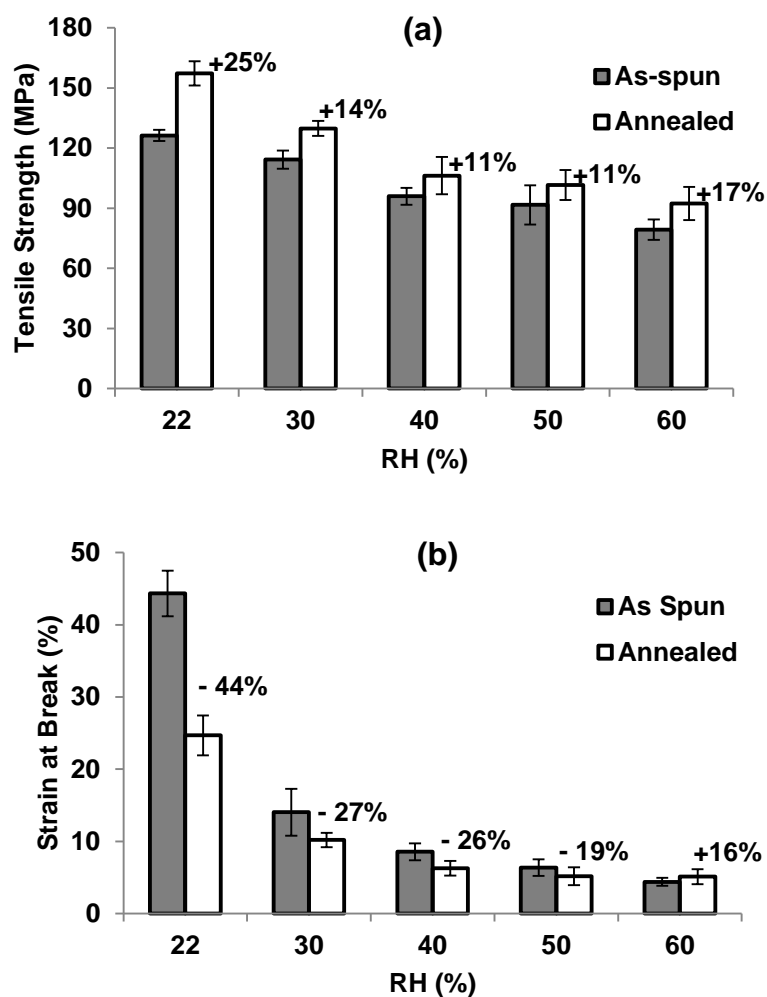


**Figure 5.16** Effect of annealing on tensile strength and strain at break for electrospun PAN nanofiber yarns produced at 20°C under various RH conditions. Numbers showing on histograms are percentage change in strength and strain at break due to annealing.

#### 5.4.5.2 Effect of Annealing

The average tensile strength and strain in break of as-spun and annealed nanofiber yarns at 20°C under various RH conditions are shown in Fig. 5.16. The results show significant improvement in mechanical strength compare to as-spun nanofiber yarns for all the RH conditions. Annealing is often used to increase the degree of crystallinity of

polymers which improves the mechanical strength [122]. The calculated percentage crystallinity from integrated WAXD plots of annealed yarns electrospun at 20°C-22% RH and 20°C-60% RH confirms 12% and 11% increase in crystallinity, respectively, as shown in Figure 5.17.

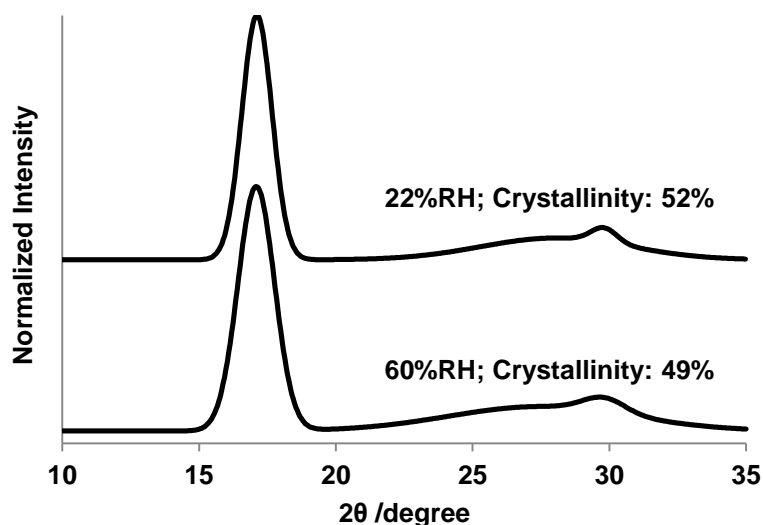


**Figure 5.17** Integrated WAXD plots and calculated percentage crystallinity of annealed PAN nanofiber yarns electrospun at 20°C and various RH conditions. Intensity profiles of integrated scans are shifted upward for clear comparison.

As shown in Figure 5.16b, annealing also affected the strain at failure of the nanofiber yarns. At 22% RH, the failure strain decreased by 44% due to annealing. However, with the increase of RH the amount reduction in failure strain decreased and eventually increased by 16% at 60% RH. This trend can be explained by two contrasting influence of annealing on the nanofibers at higher RH. On the one hand, annealing reduces the toughness of fibers by increasing the crystallinity, but on the other hand, it reduces the

structural defects of the fiber by alleviating the surface roughness and reducing porosity in the internal structure, as discussed in sections 5.4.2.3 and 5.4.3.2. At 22% RH, as-spun nanofibers were mostly defect less and exhibited large deformation to failure owing to their low crystallinity. After annealing, crystallinity of those fibers increased, and fibers broke solely due to higher crystallinity. In contrast, the porosity in the internal structure of as-spun nanofibers produced at high RH acted as stress concentration sites, and hence fibers exhibited low failure strain. Annealing reduced the porosity, and consequently, the difference between failure strain of as-spun and annealed yarn decreased, and finally at 60% RH an improvement in failure strain was observed for annealed yarn.

## **5.5 Chapter Conclusions**

The study in this chapter demonstrates that RH and temperature affect the surface morphology, structure, diameter, and mechanical properties of electrospun PAN nanofibers. The competition between solvent drying and VIPS was found to be the deciding factor of the morphology and structure evolution of the fibers during electrospinning. At low RH, the former prevails, and solid and smooth fibers are produced, while VIPS plays a vital role at high RH and porous fibers with large diameter and rough surface are observed. Phase behavior of water/DMF/PAN system at working temperatures was found as a powerful and effective tool to explore the morphology evolution with the electrospun fibers. The size of the miscible area in the ternary phase diagram decides the RH level at which the transition from solid structure



to porous structure happens. At 20°C working temperature, the transition was observed in between 22% and 30% RH, while between 30% and 40% RH was found for 40°C due to an increase in the size of miscibility area. At very low RH, beads were found as a consequence of capillary instability which emerges from surface tension of polymer solution and can be prevented by increasing RH. Thus, the morphology of electrospun nanofiber can be maneuvered by changing RH and temperature during electrospinning.

Mechanical properties of electrospun nanofiber yarns were found to be affected by the diameters as well as structure and beads in fibers. At 20°C, the highest tensile strength and strain at break were observed for yarn produced at 22% RH due to their solid structure, low diameter, and no beads in the fibers. With increasing RH to 30%, a big drop in strain at break of the yarns was observed due to the induced porosity in the structure. Similar observations were also found for yarns produced at 40°C as RH was increased from 30% to 40%. Both strength and strain at break of porous nanofiber yarn decreased as an increasing function of RH as porosity increased with RH. However, the mechanical properties of solid fibers were found to be dictated by diameter and crystallinity as yarns produced at 30°C-30% RH exhibited lower strain at break than those produced at 20°C-22% RH due to their higher crystallinity.

Annealing was found to improve the strength and reduce the strain at break for solid nanofiber yarns. However, annealing improved the overall performance of porous nanofiber yarns by alleviating surface roughness and reducing internal porosity.

## **PART II: STABILIZATION STUDIES OF ELECTROSPUN PAN NANOFIBERS**

### **Chapter 6: STABILIZATION OF PAN FIBERS**

#### **6.1 Introduction**

The CNFs from electrospun PAN nanofibers require subsequent heat-treatments such as stabilization and carbonization before they can be successfully used as composite reinforcements. The establishment of the morphological structure during the heat treatment process determines the physical and mechanical properties of the ECNFs, which depend on many factors such as precursor fiber properties, type of co-monomer, and heat treatment conditions during stabilization and carbonization [28, 162, 163].

Stabilization of PAN is commonly performed in air between 200°C and 400°C. During this process, PAN converts into a nonplastic cyclic compound that can withstand at high temperature during the carbonization process [35, 164]. It is the most influential step in determining the mechanical properties of carbon fibers, and complex physical and chemical changes occur in this step, including cyclization, dehydrogenation, oxidation, and cross-linking reactions [35, 163-169]. Stabilization is a time consuming process and may take several hours to complete. Since stabilization reactions are exothermal, and PAN polymer is not a good thermal conductive medium, extreme care needs to be taken to avoid local over-heating, which will lead to uneven stabilization, and form defects in the carbon fiber. Various environment such as hydrogen chloride (HCl) [171], sulfur dioxide (SO<sub>2</sub>) [172], nitrogen oxide (NO<sub>2</sub>) [172], and ammonia (NH<sub>3</sub>) [173] have been

tried besides oxygen to facilitate stabilization and reduce the treatment time. However, these gases are corrosive, and the process needs special instruments. The studies in this dissertation, therefore, used air as a stabilization environment. It has been found that fibers stabilized in inert environment showed worse mechanical performance along with poor carbon yield, compared to those stabilized in air.

## **6.2 Stabilization Chemistry**

The stabilization chemistry of PAN has been extensively studied in the past 50 years. To certain degree there are some general consensuses among these studies, however, for the detailed stabilization reactions, no direct evidence or definitive mechanisms have been reported and verified. In this section, commonly accepted findings of stabilization reactions are introduced.

### ***6.2.1 Cyclization Reaction***

Cyclization is the most important reaction during stabilization. During cyclization the nitrile groups ( $-C\equiv N$ ) covert into conjugated carbon-nitrogen double bonds ( $-C=N$ ). Cyclization does not occur along the whole chain, and transfer reaction may occur, leading to intermolecular propagation [174]. The scheme of cyclization reaction is shown in Figure 6.1. The formed ladder structure during cyclization helps the polymer to withstand higher temperature during carbonization and improves carbon yield. Subsequent color changes are observed during this reaction. The color of PAN fibers changes from white to yellow to golden yellow to dark brown and finally to black [175].

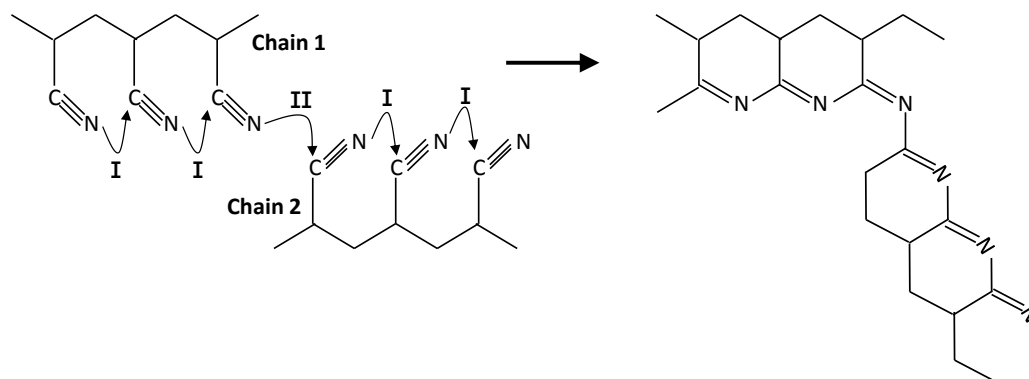


**Figure 6.1** Cyclization reaction (I- intramolecular, II- intermolecular).

### 6.2.2 Oxidation Reaction

Oxidation introduces oxygen containing groups and takes place when PAN fibers are stabilized in an oxidative atmosphere. Oxidation provides better thermal stability to the structure. There exist many assumptions for oxidized structures, such as ketonic structure [176], nitron structure [177], and cyclization with epoxide bridges [178]. The most commonly accepted model is ketonic structure which is a carbonyl group ( $-C=O$ ) and forms through elimination of water, as shown in Figure 6.2.

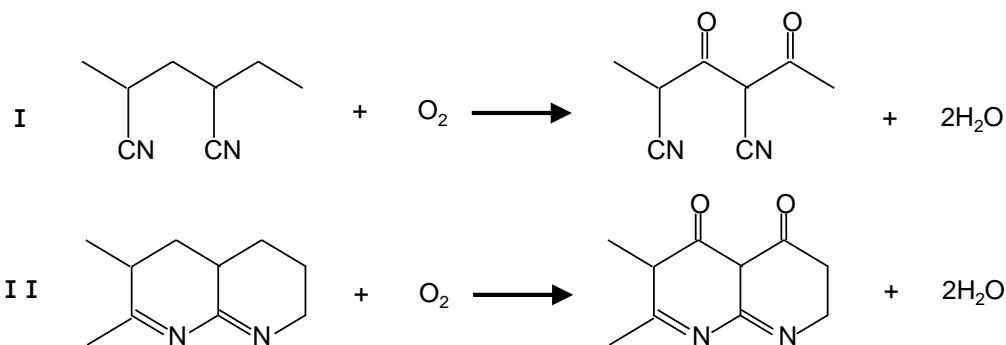


**Figure 6.2** Oxidation reaction (I- initial PAN, II- cyclized PAN).

### 6.2.3 Dehydrogenation Reaction

Dehydrogenation results in formation of carbon-carbon double bonds ( $-C=C-$ ) and conjugated structures in PAN molecules (Figure 6.3). Dehydrogenation reaction requires oxygen to occur, and must happen after oxidation. However, it is impossible to completely separate the dehydrogenation and oxidation reactions. The formation of  $C=C$  double bonds improves thermal stability and reduces chain scission during carbonization.

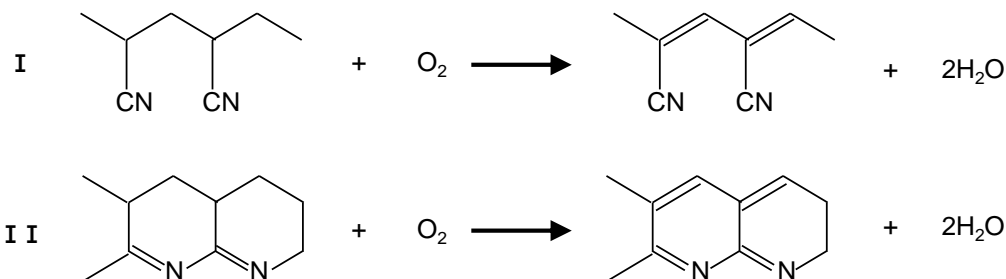


**Figure 6.3** Dehydrogenation reaction (I-initial PAN, II-cyclized PAN).

### 6.2.4 Cross-linking Reaction

At higher stabilization temperature crosslinking reaction may occur as shown in Figure 6.4.

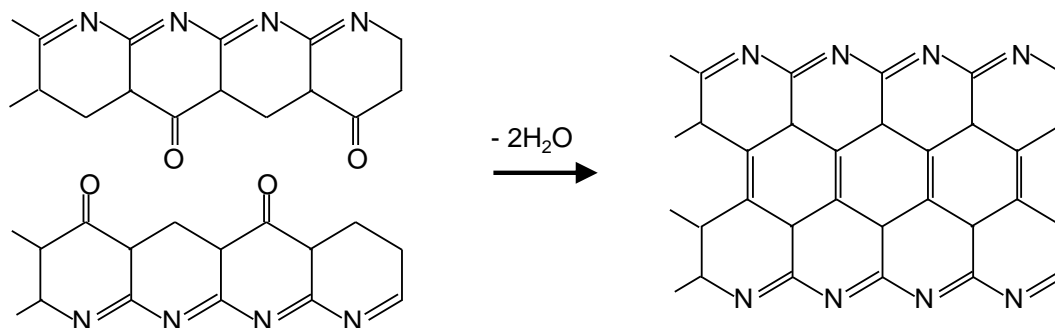


**Figure 6.4** Cross-linking reaction.

### 6.2.5 Volatile Byproducts during Stabilization

During stabilization reactions some volatile byproducts are released. Fitzer et al. [165] used gas chromatography to detect those byproducts as shown in Figure 6.5. Hydrogen cyanide (HCN) is evolved due to cyclization reaction, while  $\text{CO}_2$  and  $\text{H}_2\text{O}$  are formed during oxidation, dehydrogenation, and cross-linking reactions. The release of HCN mostly happens in the early stage of stabilization, while the release of  $\text{CO}_2$  and  $\text{H}_2\text{O}$  took a much longer time indicating that the stabilization of PAN homo-polymer is limited by oxygen diffusion.

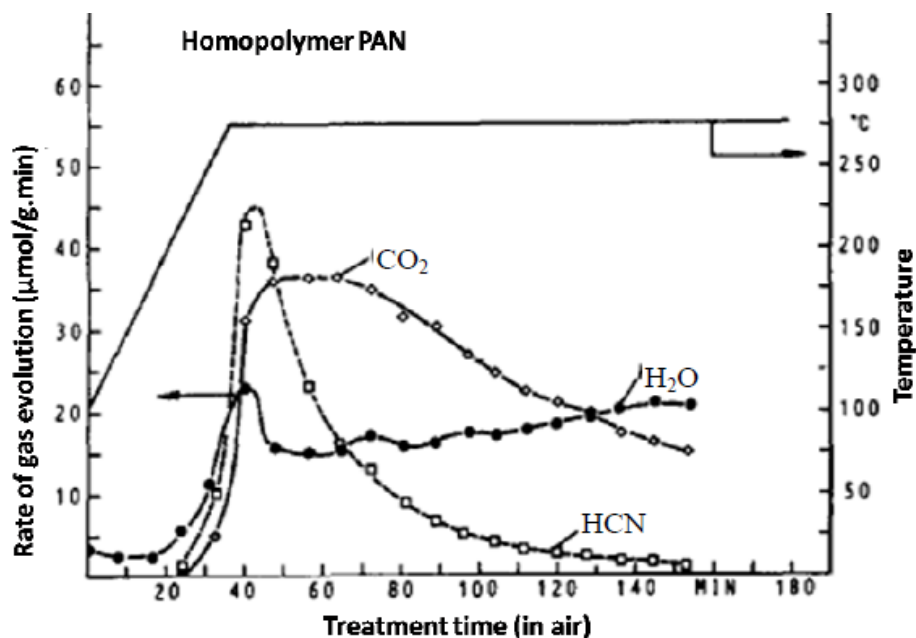


**Figure 6.5** Volatile byproducts produced during stabilization of PAN homopolymer [165].

### 6.2.6 Effect of Co-monomer

Besides PAN homo-polymer, co-polymers are also used as precursor for carbon fibers. The most commonly used co-monomers are itaconic acid (IA) and methacrylic acid (MA). The introduction of a few percent of co-monomer enhances the internal mobility of the polymer segments by interrupting the sequences of acrylonitrile molecules and therefore reducing the number of interactions with neighboring sequences. The co-monomer affects the solubility, oxygen permeation, melting point depression, and acts as a site of initial cyclization [179]. The typical DSC curves of PAN homo- and co-polymer precursor fibers are shown in Figure 6.6. It can be seen that the addition of co-monomer significantly lowers the cyclization temperature and makes the exothermic peak much broader. The lower reaction temperature will require less energy

consumption and will speed up the stabilization. A broader exothermic peak means a lower heat releasing rate, and, therefore, less possibility of local overheating.

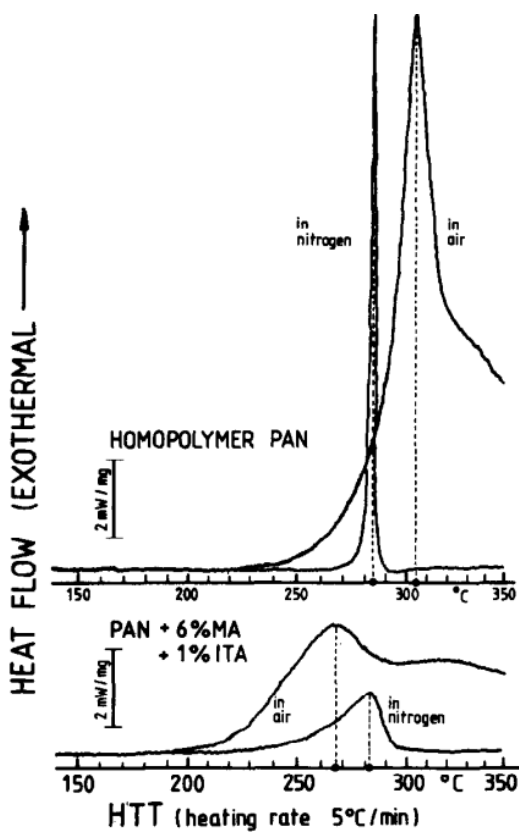


**Figure 6.6** Effect of co-monomer on stabilization of PAN [165].

### 6.3 Methods to Characterize Stabilization

Many methods have been proposed to evaluate the degree of stabilization by investigating the changes of chemical and physical properties. Some of the methods are discussed briefly here.



During stabilization PAN molecules are converted into cyclized polymer structure which causes the diffraction peak ( $2\theta=17^\circ$ ) of PAN crystal disappears, and simultaneously the formed aromatic structure shows a broad diffraction peak at  $2\theta=25.5^\circ$ . These changes can be determined using WAXD [180, 181].

Infrared spectroscopy (IR) can also be used to investigate the cyclization reaction. The nitrile groups ( $-C\equiv N$ ) of PAN has a strong absorption peak at  $\sim 2240\text{ cm}^{-1}$ . While stabilization proceeds this peak weakens and another peak evolves at  $\sim 1610\text{ cm}^{-1}$  due to the formation of new ( $-C=N$ ) bonds [163, 182].

While WAXD and IR are ex-situ techniques, there are various in situ methods, such as shrinkage [183, 184, 185] and stress [44, 186] measurements and differential scanning calorimetry (DSC) [187, 188], that have been used to monitor the extent of stabilization reaction. The chemical shrinkage during stabilization is attributed to the  $120^\circ$  rotation of the molecular chain due to the intermolecular cyclization of the neighboring polymer chains. On the other hand, if fibers are stabilized at constant length, chemical stress is developed. Stabilization reactions are exothermic and the heat evolution can be monitored by DSC. Also, the peak position could be used to calculate the reaction activation energy of cyclization.

Besides the above mentioned techniques, density change [189], mass change [44], dynamic mechanical analysis [190], and oxygen content [189] are used to investigate stabilization.

## 6.4 Overview of Research on Stabilization of Electrospun PAN Nanofibers

So far, the reported values for the strength of the electrospun PAN based CNFs are far below the strength of the micro carbon fiber. One of the crucial reasons is the lack of optimization of the stabilization conditions. Not only very few research articles are found on mechanical characterization of electrospun PAN based CNFs, but also the stabilization conditions employed in those work varied a whole lot. For instance, Zussman et al. [191] stabilized  $220^{\pm 60}$  nm diameter PAN nanofibers in air for 30 min at  $250^{\circ}\text{C}$ , and then they carbonized the nanofiber in two steps, at  $750^{\circ}\text{C}$  for 1 h and at  $1100^{\circ}\text{C}$  for 1h. Their individual CNF strength varied from 320 MPa to 900 MPa depending on nanofiber diameter and gauge length. While Zhou et al. [192] treated their PAN nanofibers at  $280^{\circ}\text{C}$  for 3 h during stabilization. Their reported tensile strength of CNF yarns were between 300 MPa and 600 MPa, which showed increasing trends with the increase of carbonization temperature between  $1000^{\circ}\text{C}$  and  $2200^{\circ}\text{C}$ . Arsad et al. [193] stabilized their PAN nanofibers by treating at  $300^{\circ}\text{C}$  for 1h. They presented tensile strengths between 1.86 GPa and 3.52 GPa for individual CNFs depending on the carbonization temperature.

## 6.5 Key Research Questions – II

Research Question 4: *How can one use various in situ characterization techniques to understand the reaction kinetics of stabilization?*

The chemical and physical changes that occur during stabilization are so complex that many mechanisms are still under research. Until now, no suitable mathematical model has been developed to explain the effect of various stabilization parameters. The only method to optimize the stabilization is to test carbonized fiber with a series of conditions to determine which condition is the best one; however, this approach is very time consuming and laborious. If one can understand the kinetics of various stabilization reactions, then it would help in better optimizing the stabilization process. Various in situ characterization techniques, as discussed in section 6.3, can be used to investigate the stabilization. In situ techniques provide real time data, and hence, no major event can be missed.

Research Question 5: *Does the understanding of reaction kinetics helps in determining optimum stabilization time? How does applied tension during stabilization affect the mechanical properties of final ECNFs?*

Although ex-situ characterization techniques, such as WAXD and IR, provide essential information on changes in molecular level during stabilization, using these techniques alone is a kind of trial and error procedure and very time consuming. However, one can significantly reduce this effort through analyzing the data from in situ characterization and by understanding the reaction kinetics. Applying tension during thermal treatment has been found to improve mechanical properties of resultant carbon fibers [35]. Thus, it is important to investigate the effect of tension during stabilization on the mechanical properties of the final ECNFs.

## **Chapter 7: IN SITU CHARACTERIZATION AND KINETICS OF STABILIZATION REACTIONS**

### **7.1 Introduction**

In this study, the kinetics of various reactions such as cyclization, oxidation, dehydrogenation, and crosslinking during oxidative stabilization of electrospun PAN nanofibers are studied by using various in situ characterization techniques. The transition time of the completion of various stabilization reactions are also determined.

### **7.2 Experimental**

#### ***7.2.1 Electrospun Nanofiber Production***

The PAN nanofibers used in this study were prepared by electrospinning 10% PAN in DMF solution at 15 kV electrospinning voltage under environmental condition of 22% RH and 20°C. The as spun nanofiber yarns were then dried in a vacuum oven at 60°C for 12 h followed by annealing at 95°C for 4 h.

#### ***7.2.2 In situ Characterization Techniques***

Heat flow and weight loss during stabilization were recorded by differential scanning calorimetry (DSC Q-50, TA Instruments) and thermo-gravimetric analysis (TGA Q-500, TA Instruments), respectively. In situ stabilization shrinkage and dynamic mechanical properties were monitored by a dynamic mechanical analyzer (DMA Q-800, TA Instruments). A small amount of load 0.5 MPa was applied during shrinkage

measurement. For dynamic mechanical tests, a constant tension of 3 MPa was applied, and the dynamic force amplitude was 0.5 MPa at a frequency of 2 Hz.

## **7.3 Results and Discussion**

### ***7.3.1 Separation of Different Stabilization Reactions***

Based on the discussion in sections 6.2.1 to 6.2.4, it can be understood that cyclization reaction can proceed in inert environment, whereas oxygen is required for other reactions to occur. Therefore, it is possible to separate reactions by altering gas environment during stabilization. This separation can help in understanding the individual reaction kinetics and in establishing an accurate stabilization model.

All the reactions during PAN stabilization release heat and can be monitored by DSC. Figure 7.1 represents the exothermic heat evolution during stabilization of electrospun PAN nanofiber in different gas environments at 5°C/min heating rate. DSC of the fibers in air exhibited a broad exothermic peak due to the overlap of multiple stabilization reactions, whereas in nitrogen only a sharp narrow peak due to cyclization reaction was observed. To isolate the effect of oxygen only, the samples treated in nitrogen were quickly cooled down to room temperature and then heat treated in air at the same heating rate. As shown in Figure 7.1, further heat treatment in air revealed two broad exothermic peaks at about 194°C and 324°C. The low temperature peak can be attributed to oxidation and dehydrogenation reactions, while the high temperature peak is caused by cross-linking reaction [169, 194]. After treating in nitrogen the initiation

and peak temperatures (229°C and 312°C) for oxidation moved to lower temperatures (144°C and 194°C) suggests that oxidation preferentially occurs in the cyclized PAN rather than in the uncyclized PAN. In both cases, run in air only and rerun in air after run in nitrogen, an increase in heat flow was observed above 390°C which is possibly due to the burning of the samples and is not desired.

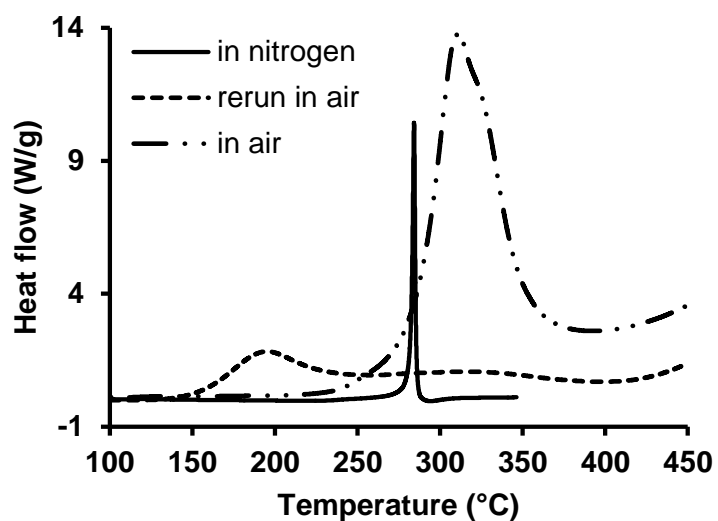


**Figure 7.1** Exothermic heat evolution during DSC runs of electrospun PAN nanofibers in different gas environments at 5°C/min heating rates.

The weight of PAN nanofibers during stabilization in nitrogen (Figure 7.2) shows a sharp drop due to the cyclization reaction above 260°C. The evolution of HCN during stabilization may lead to the major weight loss [165]. Stabilization in air resulted in less weight loss than nitrogen (Figure 7.2a, c). For the sample rerun in air after run in nitrogen, the weight increase above 140°C is attributed to the oxygen take up due to

oxidation, and the weight loss above 280°C is associated with the cross-linking reaction (Fig. 5c). The increase in the rate of weight loss in air above 390°C is due to the fast decomposition of the samples. The results are in accordance with the findings from DSC runs.

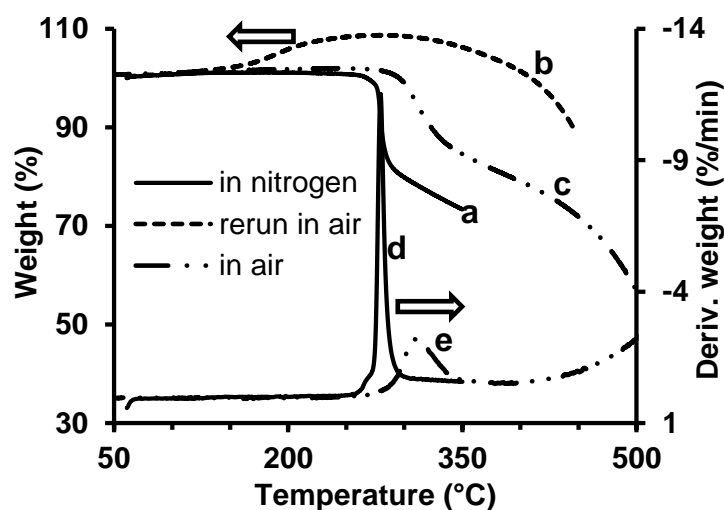


**Figure 7.2** Weight loss during TGA runs of electrospun PAN nanofibers in different gas environments at 5°C/min heating rates. (a) in nitrogen, (b) sample ‘a’ rerun in air, (c) in air only, (d) derivative of plot ‘a’, and (e) derivative of plot ‘c’.

### 7.3.2 Evolution of Kinetic Parameters of the Stabilization Reactions

The apparent activation energies ( $E_a$ ) of the stabilization reactions were determined by using Kissinger [195] and Ozawa [196] methods. These two methods are found to be mostly used in literature [163, 197, 198], because they can be used to quantify  $E_a$  without any prior knowledge of reaction mechanism but just acquiring a series of DSC curves obtained at different heating rates.

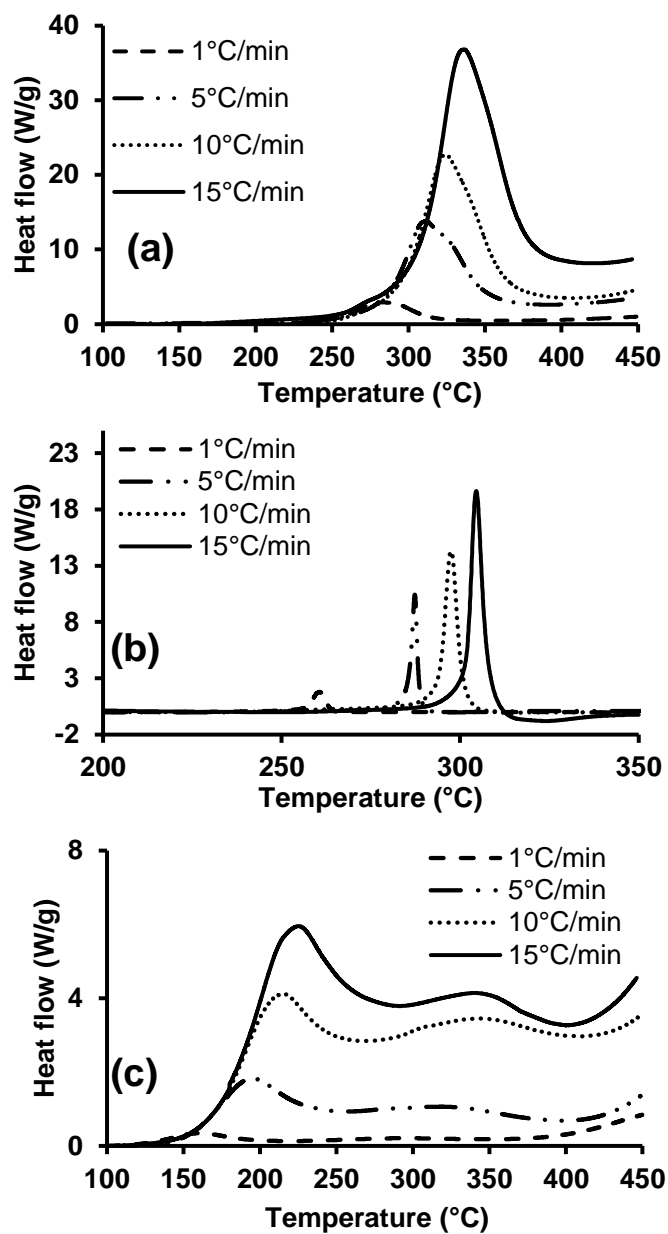


**Figure 7.3** DSC plots of electrospun PAN nanofibers in different gas environments at different heating rates. (a) in air, (b) in nitrogen, and (c) rerun in air after running in nitrogen.



Figure 7.3 presents the DSC plots in air and in nitrogen followed by run in air at various heating rates. With increasing the heating rate, the exothermic peaks shifted to higher temperatures, and the peaks became more and more strong. A comparison of exothermic peaks of PAN fibers heated in different gas environment suggests that the reactions in air occur in a much broader temperature range and the exothermic peak appears at a higher temperature ( $>20^{\circ}\text{C}$ ) than in nitrogen. As mentioned before only cyclization reaction occurs when PAN is treated in nitrogen, while in air other stabilization reactions that need oxygen also happen besides cyclization. The oxidative reactions are mainly controlled by the diffusion of oxygen and are more affected by the transport of mass than that of heat, while cyclization reactions are greatly influenced by temperature and the free radical cyclization reaction is initiated when a certain temperature is reached. Thus, oxidation needs more time to complete than cyclization.

**Table 7.1** DSC peak maxima for electrospun PAN nanofibers in various gas environments.

Heating rate, $\phi$ ( $^{\circ}\text{C}/\text{min}$ )	In air	In Nitrogen	Rerun in air after running in nitrogen	
	$T_m$ ( $^{\circ}\text{C}$ )	$T_m$ ( $^{\circ}\text{C}$ )	$T_m$ ( $^{\circ}\text{C}$ ) (1 <sup>st</sup> peak)	$T_m$ ( $^{\circ}\text{C}$ ) (2 <sup>nd</sup> peak)
1	281.2	260.7	159.3	290.0
5	311.4	284.2	193.8	323.7
10	324.5	297.4	212.0	342.3
15	336.3	304.5	221.9	348.1

As listed in Table 7.1, the DSC peak maximum ( $T_m$ ) shows a regular increase with the increasing of heating rate ( $\Phi$ ), which was employed for Kissinger and Ozawa methods to evaluate  $E_a$ . Kissinger's method uses an equation as follows [195]:

$$-\frac{E_a}{R} = \frac{d[\ln(\Phi/T_m^2)]}{d(1/T_m)}$$

where  $T_m$  is the absolute temperature corresponding to the maximum in the DSC exotherm at a heating rate of  $\Phi$ .  $E_a$  is calculated from the slope of the linear plot of  $\ln(\Phi/T_m^2)$  against  $1/T_m$ .

Ozawa's method makes the use of the following equation [196]:

$$-2.19 \frac{E_a}{R} = \frac{d(\log \Phi)}{d(1/T_m)}$$

$E_a$ , obtained from the slope ( $S$ ) of the linear plot of  $\log \Phi$  against  $1/T_m$ , was refined by iteration, making use of a two-term approximation for the Arrhenius temperature [198].

$$p(x) = e^{-x} \left[ \frac{x+1}{x+3} \right]$$

where  $x=E_a/RT$ . The theoretical slope ( $D$ ) of the above equation is  $-1-2/x+1/(1+x)-1/(x+3)$ . The process of the iteration was continued until constant value for  $E_a$  ( $= -2.303RS/D$ ) is reached. This refinement is recommended for Ozawa method in ASTM E698.

The Kissinger and Ozawa plots are shown in Figure 7.4. The activation energies related to different reactions are named as cyclization activation energy ( $E_{a\text{-cyclization}}$ ), oxidation and dehydrogenation activation energy ( $E_{a\text{-oxidation}}$ ), and additional cross-linking

activation energy ( $E_{a\text{-crosslinking}}$ ). Based on the calculated activation energies, the pre-exponential factor,  $A$  in the Arrhenius equation  $k=Ae^{-E_a/RT}$  ( $k$  is the rate constant of reactions) is calculated by

$$A = \frac{\Phi E_a}{RT_m^2} e^{E_a/RT}$$

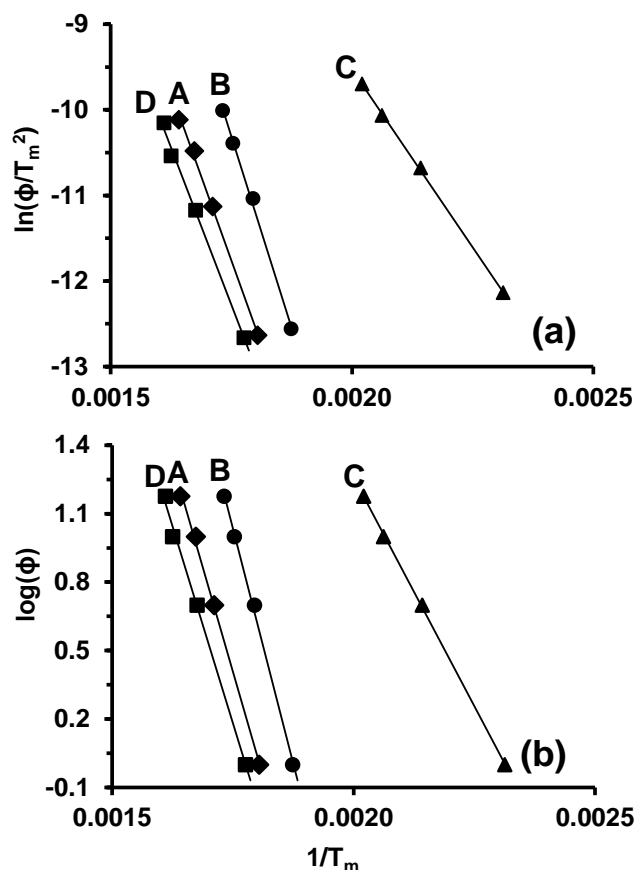


**Figure 7.4** Plots according to (a) Kissinger's method and (b) Ozawa's method. A. PAN nanofiber in air, B. cyclization peak of PAN nanofibers in nitrogen, C and D. oxidation and crosslinking peak of PAN nanofiber rerun in air after running in nitrogen, respectively.

All the calculated results for  $E_a$  and A values are summarized in Table 7.2. Both methods gave nearly identical values for each set of  $E_a$  and A. Among all types of reactions, the cyclization reaction exhibited the highest activation energy. The reason is that homo-polymer PAN without any acidic constituent does not initiate ladder polymer formation very readily and need high temperature to overcome the energy barrier [176, 199]. On the other hand, formation of ladder structure, that is cyclization, is prerequisite for oxidation and dehydrogenation. Thus, the activation energy for oxidation and dehydrogenation is found to be the lowest as it is evaluated from cyclized PAN. During stabilization of PAN in air, the oxidation and dehydrogenation reactions are delayed until a cyclized PAN structure is formed [176].

**Table 7.2** Calculated kinetic parameters determined by Kissinger's and Ozawa's methods.

	Kissinger's method		Ozawa's method	
	$E_a$ (kJ/mol)	A ( $s^{-1}$ )	$E_a$ (kJ/mol)	A ( $s^{-1}$ )
In air	130.6	$1.2 \times 10^{11}$	130.6	$1.1 \times 10^{11}$
$E_{a-cyclization}$	148.7	$2.3 \times 10^{13}$	148.9	$2.4 \times 10^{13}$
$E_{a-oxidation}$	68.9	$9.5 \times 10^6$	69.0	$9.3 \times 10^6$
$E_{a-crosslinking}$	122.0	$8.9 \times 10^9$	122.4	$9.6 \times 10^9$

### 7.3.3 Reaction Shrinkage in PAN Nanofiber Yarn during Stabilization

Figure 7.5 depicts the in situ strain measurement during stabilization of PAN nanofiber yarn in air at a heating rate of  $5^\circ\text{C}/\text{min}$ . Stretching of the yarn was observed till  $237^\circ\text{C}$

due to the applied tension in DMA which was also observed for PAN fiber by Liu et al. [185] and Bahl et al. [183]. Beyond 237°C shrinkage in the yarn is observed which increased with the temperature. In literature [165, 183-185], this shrinkage was discussed as chemical or reaction shrinkage and attributed to the 120° rotation of the molecular chain due to the intermolecular cyclization (Figure 6.1-II) of the neighboring polymer chains. Thus, in situ shrinkage measurement during stabilization of PAN in air can be used to study the cyclization reaction and therefore be used as criteria to find optimum stabilization time. Fitzer et al. [165] used the derivative of the shrinkage in determining the beginning and the end of the chemical shrinkage. The beginning, end, and maximum rate of chemical shrinkage were found to be at 237°C, 390°C and 319°C as shown in Figure 7.5, and the amount of total chemical shrinkage was found to be 27%. By comparing the DSC heat flow in nitrogen (Fig. 4) and shrinkage measurement in air (Fig. 8), the difference between cyclization reactions in these two environments can be explained. In both cases, the cyclization reaction begins almost at the same temperature, but it occurs in a much broader temperature range in air along with the maximum reaction rate appearing at a higher temperature (>35°C). Although cyclization can occur in inert environment, oxygen can also affect the cyclization reaction, which can be explained as follows.

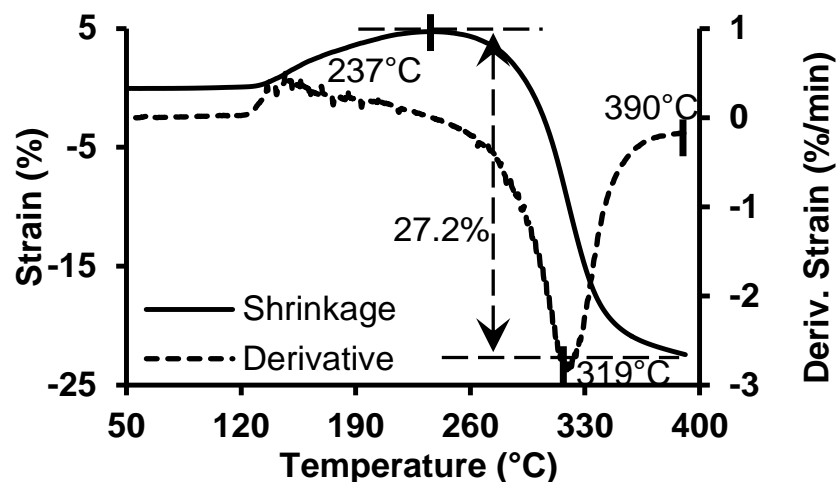


**Figure 7.5** Change in PAN nanofiber yarn length under a tension of 0.5 MPa in air at a heating rate of 5°C/min.

It has been found in literature [163, 165, 168, 200] that, the nature of the polymer and the stabilization environment play important roles in deciding the cyclization reaction mechanism as well as the ratio of inter- to intramolecular cyclization, which decides the amount of chemical shrinkage. For example, the cyclization reaction in PAN homopolymer is initiated by radical mechanism, whereas cyclization is initiated by ionic mechanism in acid containing PAN [200]. Since the chemical shrinkage increases with increasing the amount of acidic content in PAN, it is believed that the ionic mechanism prefers intermolecular cyclization more than the radical mechanism does. Stabilization of PAN homo-polymer in oxygen containing environment leads to larger shrinkage as compared to stabilization in inert environment [183, 184]. As in the acidic group containing PAN, the formed oxidative groups during stabilization of PAN homo-

polymer in air are believed to initiate intermolecular cyclization reaction, which depends on oxygen diffusion rate and progresses slowly.

To study the effect of temperature on the fiber shrinkage, yarns were heated at 5°C/min to various final temperatures and isothermally treated at those temperatures. The in situ shrinkage measurements along with the temperature profiles are shown in Figure 7.6a. It can be seen that the shrinkage i.e. cyclization reaction was faster at higher temperature. However, temperature did not significantly affect the amount of final shrinkage although it was not the case for PAN micro fiber observed by Liu et al. [185]. They observed about 33% reduction in shrinkage when temperature was increased from 250°C to 285°C. The shrinkage rate of the fiber can be limited either by radical cyclization or by ionic cyclization i.e. oxygen diffusion. With increasing temperature the radical cyclization rate increases at a faster rate than the rate of oxygen diffusion does. In microfiber the oxygen diffusion rate is much slower than that in nanofiber. Thus, the oxygen diffusion limitation on the stabilization becomes more and more significant with increasing temperature in micro fiber than in nanofiber.

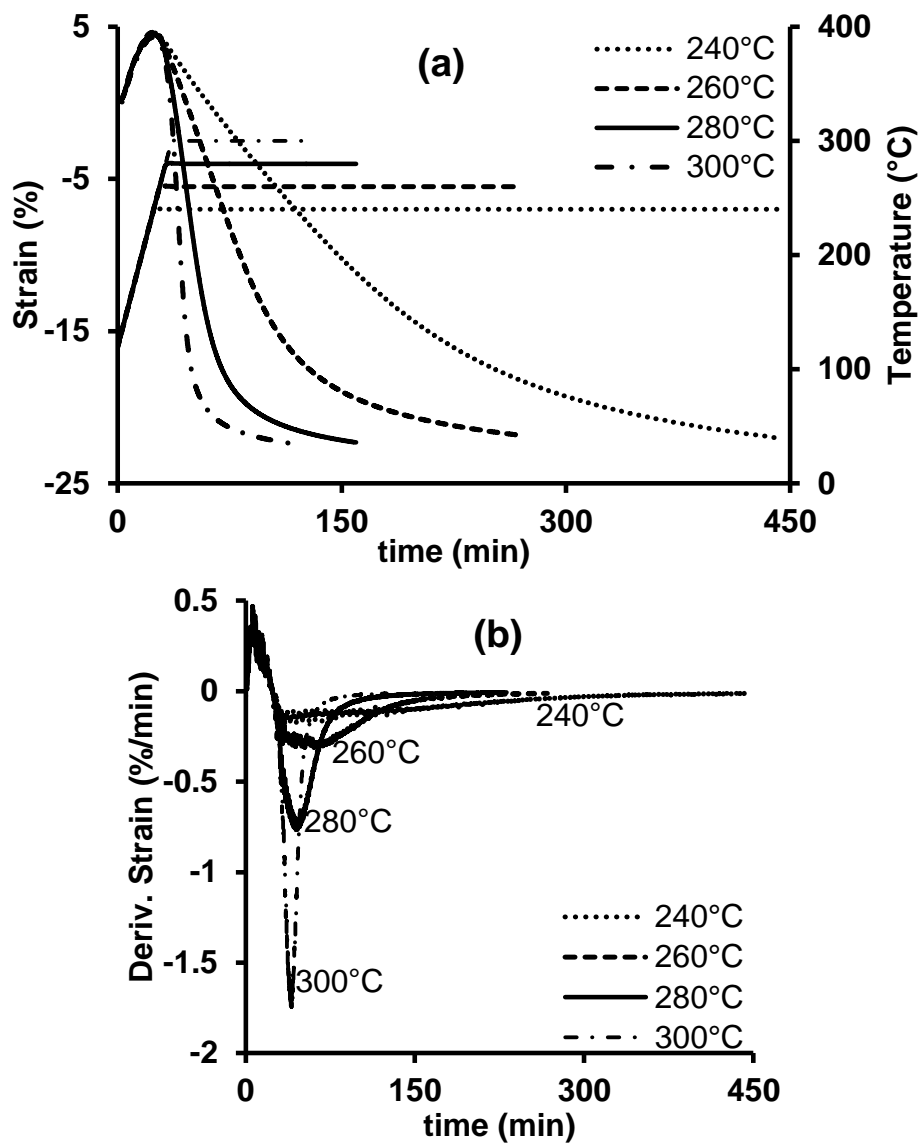


**Figure 7.6** Reaction shrinkage behavior of PAN nanofiber yarn isothermally stabilized at various final temperatures under a tension of 0.5 MPa in air. (a) Shrinkage along with temperature profile, and (b) derivative of strain. Heating rate was 5°C/min.

It has been found that the cyclization reaction follows first order kinetics [166, 184, 201], and therefore shrinkage in air is fitted by  $S(t) = S - S_1 \cdot \exp(-k_1 \cdot t) - S_2 \cdot \exp(-k_2 \cdot t)$ , where  $S$  is the final shrinkage,  $S_1$  is the shrinkage due to radical cyclization and  $S_2$  is the



shrinkage due to ionic cyclization which is caused by the formed oxidative groups, and  $k_1$  and  $k_2$  are the reaction rate constants of the respective cyclization reactions. It is noted here that  $k_1$  should be higher than  $k_2$  as the radical cyclization progresses at a faster rate than the ionic cyclization does, which depends on the oxygen diffusion. The curve fitting of the isothermal shrinkage curves at various final temperatures are shown in Figure 7.7a. An example of the curve fitting showing the fast decay due to radical cyclization and the slow decay due to the ionic cyclization is also shown in Figure 7.7b. The Arrhenius plots of reaction rates  $k_1$  and  $k_2$  along with the calculated activation energy from the curve fitting are shown in Figure 7.8. The activation energy (143.5 kJ/mol) of the fast decay fitting was found to be very close to the activation energy (148.7 kJ/mol) calculated from the DSC runs in  $N_2$  which confirms that the fast decaying shrinkage is due to the radical cyclization. While the activation energy of slow decaying shrinkage was found 96.3 kJ, and it needed longer time for completion which means it is limited by oxygen diffusion. The isothermal stabilization times for various final temperatures at which fibers reach to the maximum reaction shrinkage are listed in Table 7.3.

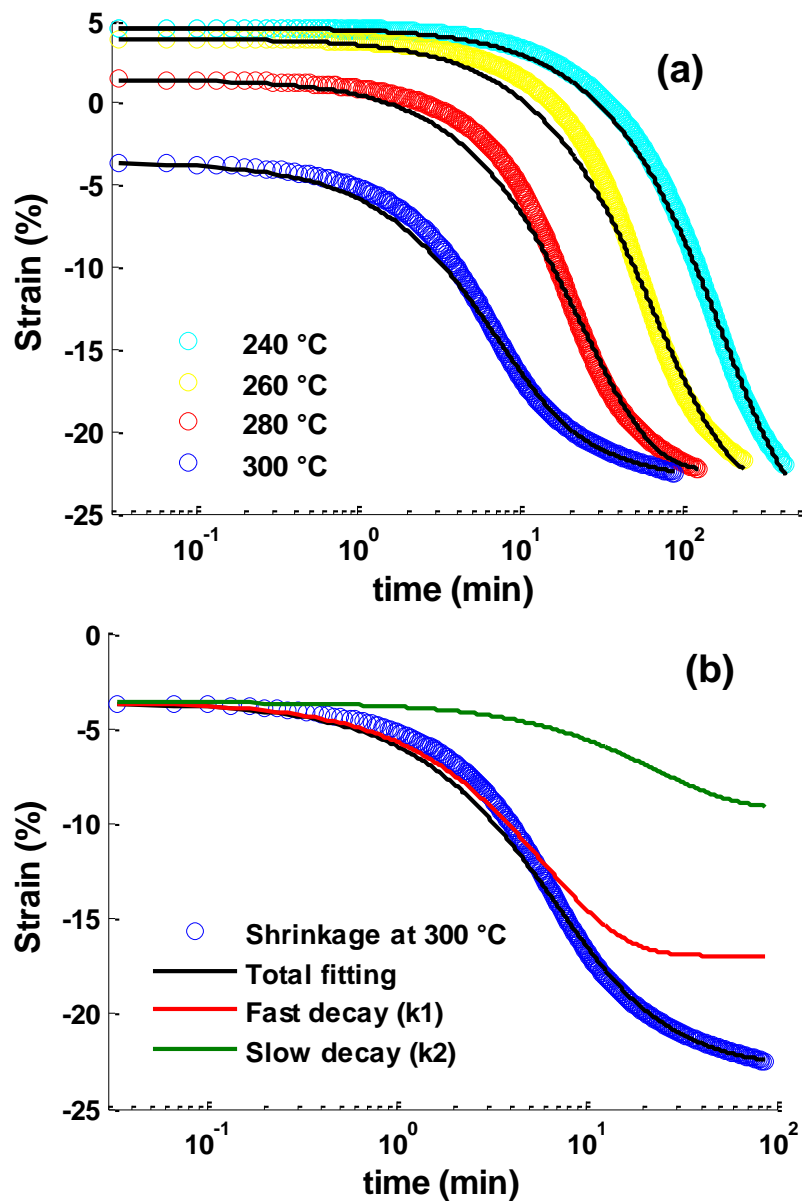


**Figure 7.7** (a) Curve fitting of the shrinkage of PAN nanofiber yarn isothermally stabilized in air at various final temperature after heating at 5°C/min. (b) An example of curve fitting showing the fast decay (radical cyclization) and the slow decay (ionic cyclization).

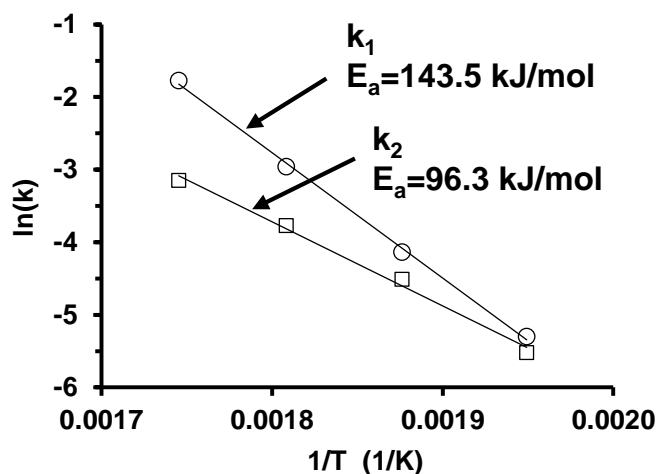


**Figure 7.8** Arrhenius plots of parameters  $k_1$  and  $k_2$ .

**Table 7.3** Isothermal time at various final temperatures to reach to the maximum shrinkage.

Temperature (°C)	Isothermal time (min)
240	398
260	189
280	95
300	74

#### 7.3.4 Dynamic Mechanical Properties of PAN Nanofiber Yarn during Stabilization

Figure 7.9 depicts the change in dynamic mechanical behavior of PAN nanofiber yarn in air at a heating rate of 5°C/min. The  $\tan \delta$  peaks at 120°C, and 160°C are due to the molecular motion of the sequences in the ordered paracrystalline regions and the glass transition of the less ordered amorphous regions, respectively [202]. Whereas the  $\tan \delta$  peak at 329°C is attributed to the chemical change during stabilization [190]. It can also

be seen from the figure that the storage modulus monotonically increased with temperature above 230°C and reached to a plateau, whereas the loss modulus increased to a maximum and then decreased with temperature. It has been showed that cyclization of PAN causes increase in both storage and loss moduli, whereas crosslinking reaction causes further increase in storage modulus and decrease in loss modulus [194]. Thus, the maximum value of the loss modulus can be attributed to a transition where the crosslinking reaction becomes dominant.

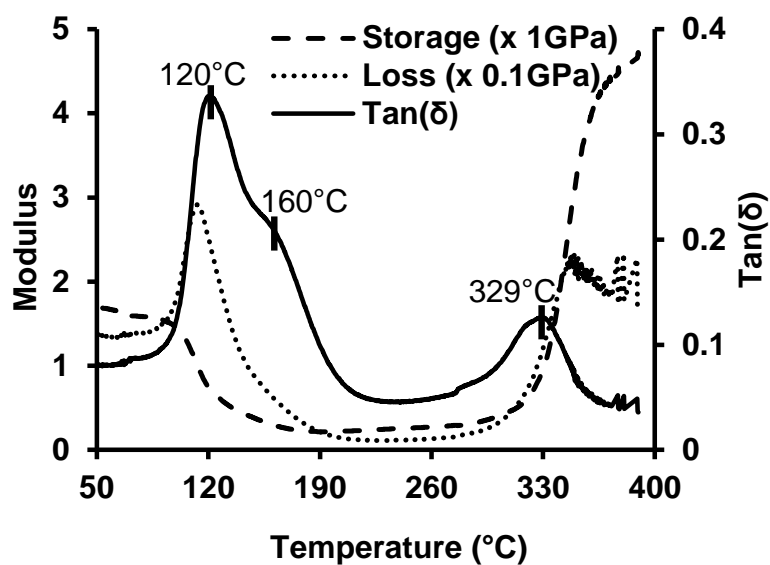


**Figure 7.9** Change in storage modulus, loss modulus, and  $\tan(\delta)$  during stabilization of PAN nanofiber yarn in air at a heating rate of 5°C/min.

The changes in storage modulus and loss modulus during isothermal stabilization at various final temperatures in air are shown in Figure 7.10. The transition times at which the loss modulus and the storage modulus reach to the maximum values are shown in Table 7.4. Although, the time at which the storage modulus reaches to the maximum

value indicates the completion of all the stabilization reactions, it may cause over-oxidation leading to thermal degradation and hinder the carbonization process [166]. Thus, the optimum stabilization time may be between these two transition times.

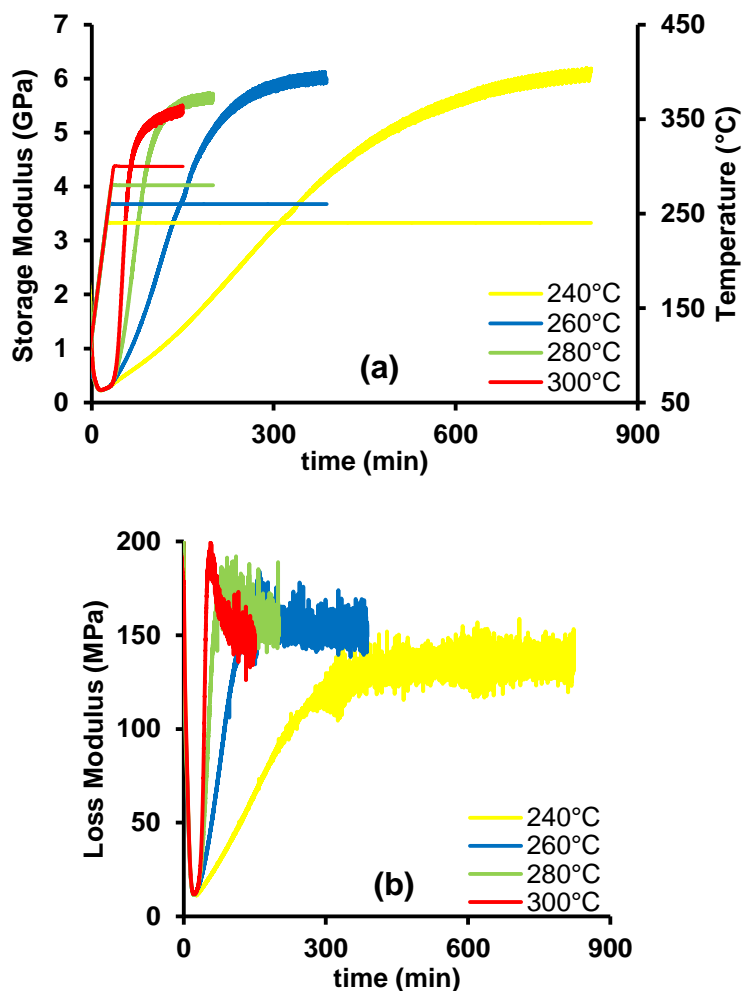


**Figure 7.10** Dynamic mechanical behavior of PAN nanofiber yarn isothermally stabilized in air at various final temperatures after heating at 5°C/min. (a) Storage modulus, and (b) loss modulus.

**Table 7.4** Calculated isothermal time at various final temperatures to reach to the maximum storage modulus and loss modulus.

Temperature (°C)	Isothermal time (min)	
	Loss modulus	Storage modulus
240	471	730
260	132	359
280	50	162
300	18	100

#### 7.4 Chapter Conclusions

The individual reactions during oxidative stabilization of electrospun PAN precursor nanofibers can be separated by altering the environment from nitrogen to air in sequence. The cyclization reaction was found to have the highest activation energy followed by oxidation/dehydrogenation and crosslinking reactions. Cyclization reaction in air progresses by two different mechanisms such as radical cyclization which depends only on the temperature and ionic cyclization which is initiated by the formed oxidative groups and limited by the rate of oxygen diffusion. The transition time of the completion of cyclization reaction was determined from the derivative of the shrinkage measurement curve, while the transition time of crosslinking reaction becoming dominant and end of all stabilization reactions was determined from the dynamic mechanical analysis during oxidative stabilization.

## **Chapter 8: OPTIMIZATION OF STABILIZATION TIME**

### **8.1 Introduction**

In this study, 260°C was used as stabilization temperature, as the final storage modulus of PAN nanofiber yarn stabilized at this temperature was highest among all the yarns stabilized at various temperatures. According to the shrinkage measurement, the stabilization time should be 189 min to complete the cyclization reaction, while the dynamic mechanical property characterization tells the optimum stabilization time should lie in between 132 min and 359 min. WAXD of stabilization yarn and mechanical properties of the carbonized yarn were used as post process characterization methods to evaluate the optimum stabilization time.

### **8.2 Experimental**

#### ***8.2.1 Stabilization Process***

A programmable air convection oven (Model 825, Cole-Parmer) was used for stabilization. The as spun PAN nanofiber yarns, prepared from 10% PAN in DMF solution at 20°C and 22% RH, were placed into the oven and heated from room temperature to 260°C at a ramp rate of 5°C/min and held there for a preset amount of time. For constant length stabilization yarns were held on a steel plate by applying ceramic glue at two ends.

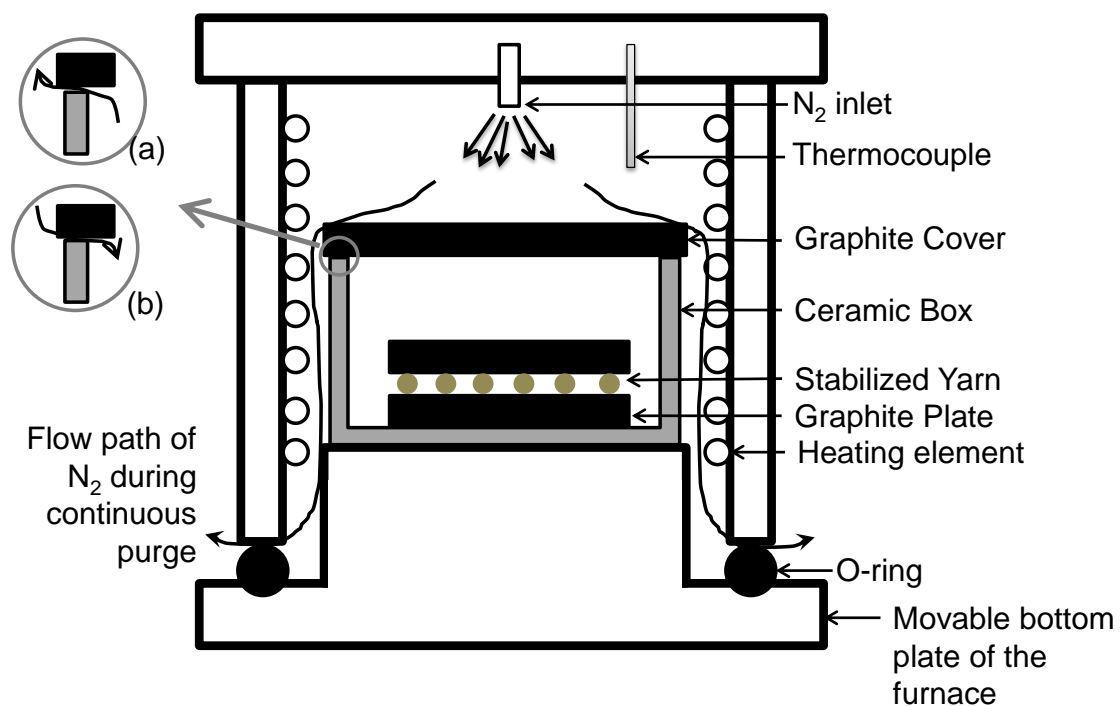


**Figure 8.1** A schematic of cross-sectional view of sample arrangement inside the furnace. Insets are showing gas flow direction during vacuum (a) – purge (b) cycles.

### 8.2.2 Carbonization Process

After stabilizing in air, yarns were carbonized in a N<sub>2</sub> atmosphere at 1100°C for 40 min, utilizing a Whipmix Pro 100 furnace. The temperature ramp rate used during carbonization was 5°C/min. It is to be noted here that this furnace is designed for ceramic sintering application and not intended for carbonization application. To the best of my knowledge, for the first time this furnace was utilized for carbonization application by introducing a special arrangement. Figure 8.1 depicts the cross-sectional view of the furnace along with samples inside. Stabilized yarns were put in between two graphite plates inside a homemade alumina ceramic box. A graphite cover was applied



on the top of the box so that N<sub>2</sub> flow did not directly attack the sample. Directly purge on the samples (without any cover) often resulted in yarn breakage. Ten vacuum-purge cycles were employed during 30 min presoak stage before a continuous N<sub>2</sub> purge was applied. During vacuum-purge cycle, a pump was automatically turned on first to pull out all the gas from the furnace, after reaching a certain vacuum the pump was automatically turned off and at the same time the flow controller was turned on to fill N<sub>2</sub> into the furnace. N<sub>2</sub> was then purged for 5 min before the bottom plate was pushed up to seal the chamber and the vacuum pump was turned on to start another vacuum-purge cycle. By doing this for several times a highly inert condition was achieved and it was then maintained by a constant flow of N<sub>2</sub>. Graphite plates were used to eliminate or reduce any oxidation reaction caused by any oxygen diffusion at high temperature. No tension was applied to the yarn during carbonization.

### ***8.2.3 Characterization Techniques***

#### ***8.2.3.1 WAXD***

Wide angle X-ray diffraction (WAXD) patterns of the yarns were obtained by a Rigaku pinhole collimation SAXS system.

#### ***8.2.3.2 Tensile Testing of ECNF Yarn***

As carbonized samples were very brittle to clamp, paper window frames were used for their mechanical characterization. A modification to the old design, used by other researchers [203, 204] for polymeric single fiber testing, was done as shown in Figure 8.2. Before beginning the tensile test the two legs on both sides of the center line need

to be cut. In the case of old design (Figure 8.2a), the applied force during cutting caused deformation at the center line (Figure 8.3a) which could break significant number of nanofibers in the mounted yarn. This problem was resolved by employing the new design (Figure 8.2c) as it can be seen from Figure 8.3b that there was no deformation at the center line where the yarn would be mounted. A photograph of few paper window frames is shown in Figure 8.4.

All the carbonized samples were tested at a force ramp of 1 N/min, as they are not sensitive to strain rate, and a gauge length of 6 mm was used. All the stress values were calculated based on theoretical cross-sectional area which was determined from the measured yarn denier and the density of the material. Density of the carbonized nanofibers was assumed to be 1.78 g/cc as reported in literature [205-207].

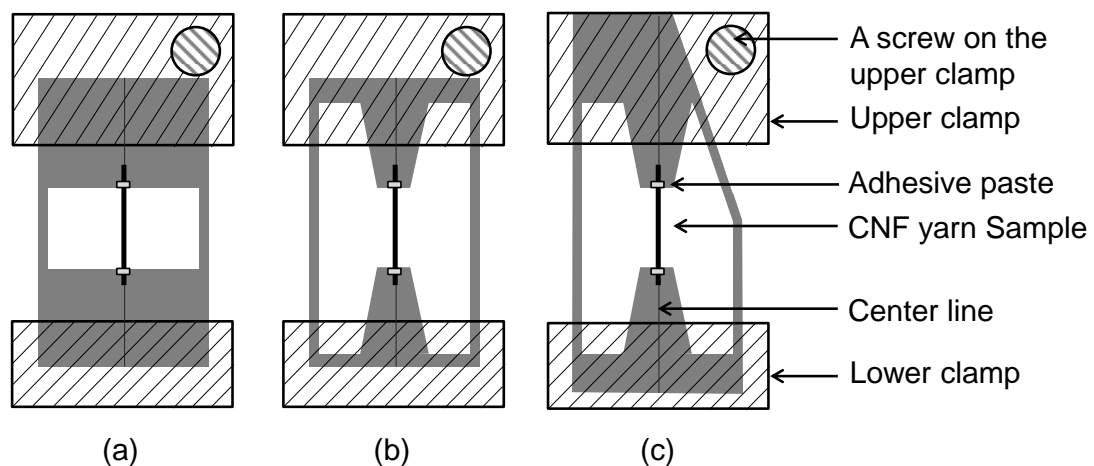


**Figure 8.2** A schematic of paper window frames for tensile test of carbonized yarn. (a) Old design, (b) new design (d) new design modified for clamp geometry.

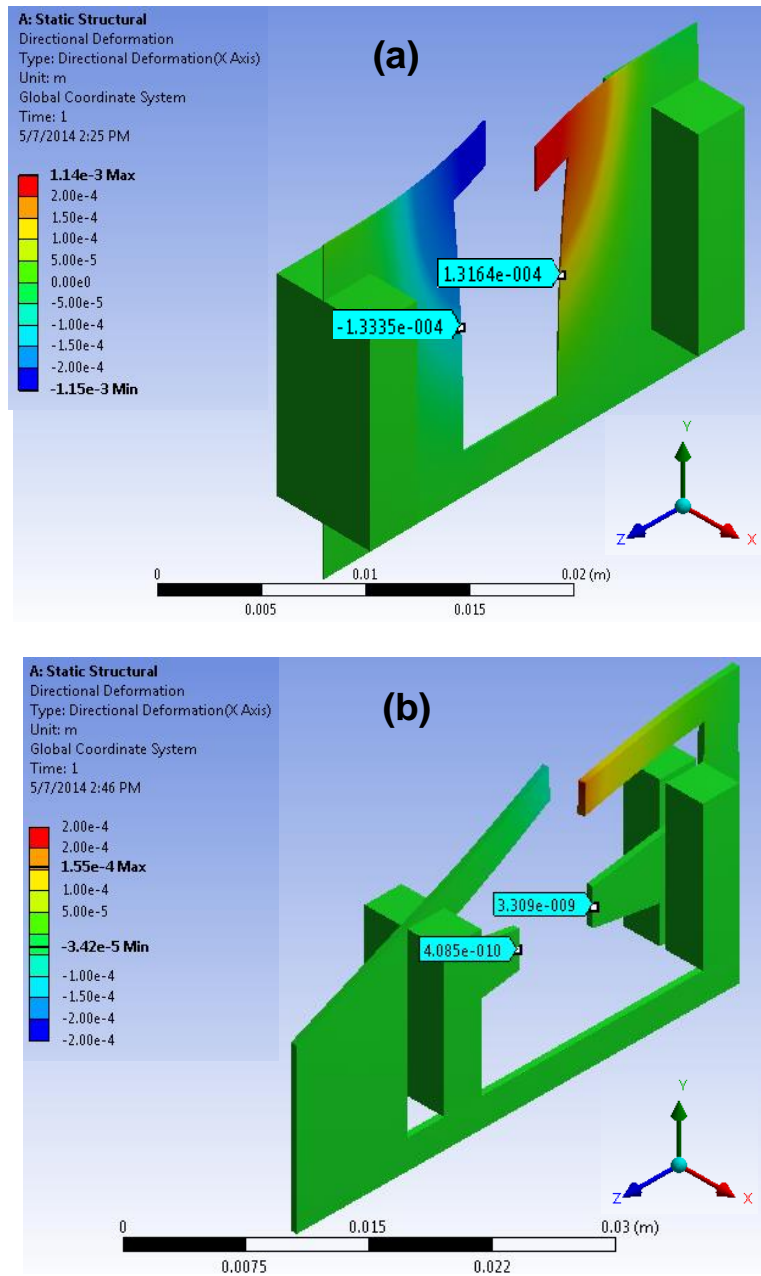


**Figure 8.3** Finite element analysis of the tensile test window frames. (a) old design, (b) new design.



**Figure 8.4** A photograph of few paper window frames.

#### 8.2.3.3 SEM

Morphology of the carbonized nanofibers was observed by a Zeiss Neon high resolution scanning electron microscope (SEM).

### 8.3 Results and Discussion

#### 8.3.1 WAXD Analysis of Stabilized Nanofibers

Figure 8.5 shows the changes in WAXD pattern of PAN nanofibers after stabilizing in air at 260°C for various times. The electrospun precursor nanofibers depicted a strong peak centered at 16.7° and a weak diffusion diffraction centered at 29.4°. These two peaks represent the X-ray reflection of (100) and (110) crystallographic planes [191, 180, 208]. Yu et al. [180] showed that the intensity of (100) peak of PAN decreased as the stabilization progressed due to the destruction of PAN crystals structure, and this peak did not become superpose with others, and its center hardly moved during

stabilization; and can therefore, be used to evaluate the progress of the stabilization reaction.

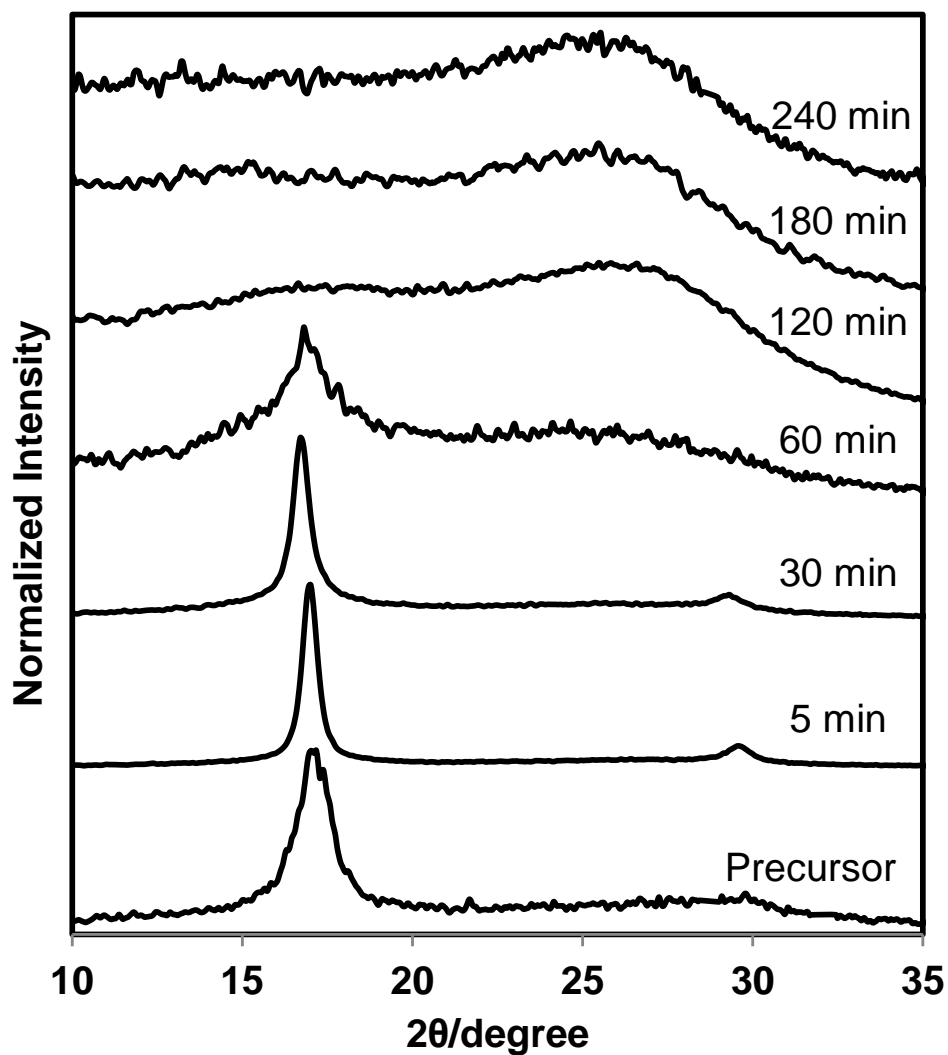


**Figure 8.5** WAXD pattern of PAN precursor nanofiber yarn and nanofiber yarns isothermally stabilized at 260°C in air for various times.

As seen from Figure 8.5, the relative intensity of (100) peak for nanofiber stabilized for 30 min did not show a great change. However, it greatly decreased after 60 min, and almost disappeared for 120 min stabilized nanofibers. For nanofibers stabilized for 180 min and 240 min, the intensity of (100) peak was completely disappeared. The (110) peak also remained and even became stronger till 30 min of stabilization, and at 60 min, it almost disappeared. A new peak at the  $2\theta$  angle of around  $26^\circ$  was observed for nanofibers stabilized for 60 min, which became stronger with time. This new peak is attributed to (101) crystallographic plane representing the ladder-like polymeric structure in the stabilized PAN nanofiber [208].

### ***8.3.2 Effect of Stabilization Time on Mechanical Properties of ECNFs***

The PAN nanofiber yarns stabilized at  $260^\circ\text{C}$  in air for various times were carbonized in nitrogen by heating at  $5^\circ\text{C}/\text{min}$  to  $1100^\circ\text{C}$  and then isothermally treated for 40 min. It is noted that no constraint on the yarn was applied during both stabilization and carbonization. Tensile property data shows that stabilization time has a significant effect on the property of the final carbon nanofiber yarns (Fig. 8.6 and Table 8.1). The optimum time for stabilizing the fibers at  $260^\circ\text{C}$  was about 150 min; longer and shorter stabilization times resulted in a decrease in the tensile properties of the final carbon nanofiber yarns. Thus, the variations in the mechanical properties of the ultimate carbon nanofiber yarns are in agreement with the findings from the analysis of in situ characterization and the WAXD analysis of the stabilized fibers.

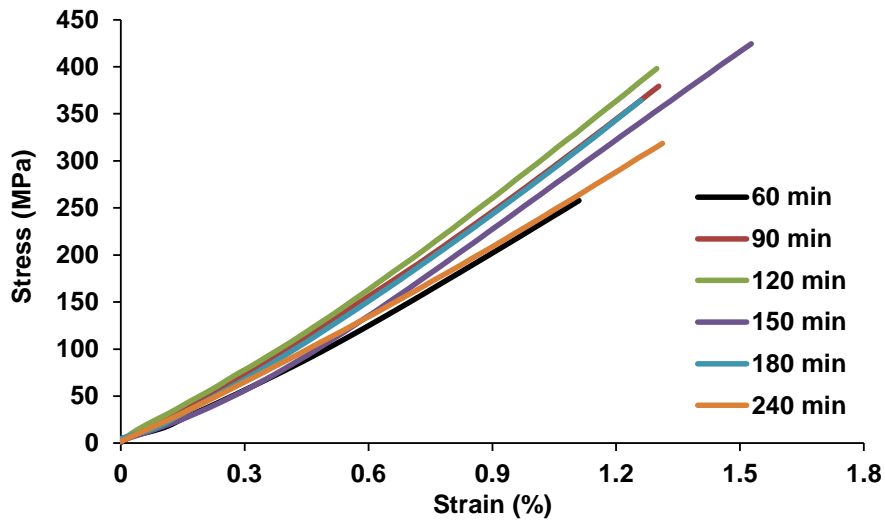


**Figure 8.6** Representative tensile stress-strain curves of carbonized nanofiber yarns after stabilization at 260°C for various times.

**Table 8.1** Tensile properties of carbonized nanofiber yarns after stabilization at 260°C for various times. No constraint was applied during stabilization and carbonization.

Stabilization time (min)	Tensile strength (MPa)	Tensile Modulus (GPa)
60	258 <sup>±41</sup>	24.5 <sup>±3.4</sup>
90	370 <sup>±44</sup>	28.5 <sup>±2.4</sup>
120	390 <sup>±58</sup>	31.0 <sup>±3.6</sup>
150	432 <sup>±37</sup>	33.6 <sup>±2.2</sup>
180	391 <sup>±39</sup>	29.5 <sup>±2.4</sup>
240	336 <sup>±35</sup>	25.4 <sup>±4.2</sup>

### 8.3.3 Effect of Constant Length Stabilization on Final ECNFs

It has been reported that tension applied during thermal treatment is important to enhance mechanical properties of resultant carbon fibers [35, 209, 210]. The applied

tension prevents the polymer chains from relaxing and losing their orientation, which becomes locked in through crosslinking [209]. To apply tension during stabilization the length of the as spun yarns were held at constant length. Figure 8.7 depicts representative stress-strain graphs and Table 8.2 represents the tensile properties of the final carbonized nanofiber yarns after carbonizing at 1100°C for 40 min without applying any tension. The mechanical properties of the yarns carbonized from constant length stabilized fibers were found to be much higher than those carbonized from free shrinkage stabilized fibers (see Table 8.1). However, the optimum time was found to be reduced to 120 min from 150 min. To investigate the reason behind this the morphology of few selective yarns stabilized at constant length and their corresponding carbonized yarns were studied.

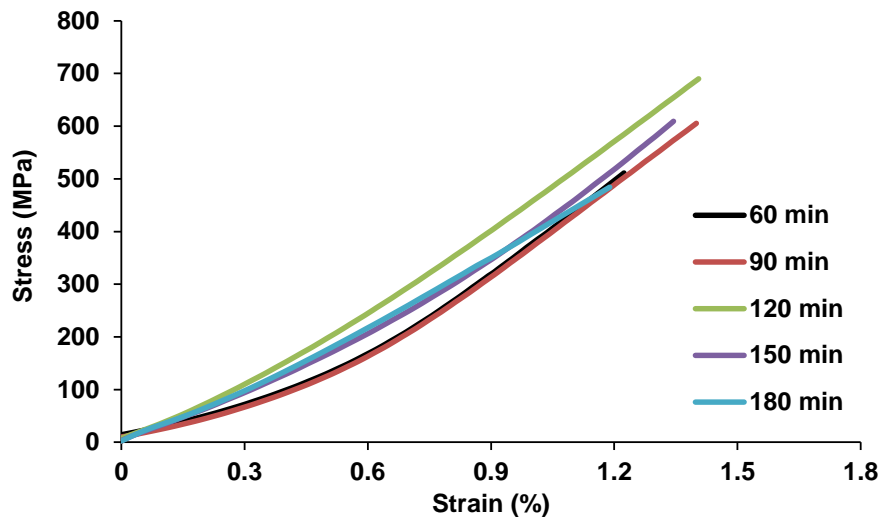


**Figure 8.7** Representative tensile stress-strain curves of carbonized nanofiber yarns after constant length stabilization at 260°C for various times.



**Table 8.2** Tensile properties of carbonized nanofiber yarns after constant length stabilization at 260°C for various times. No tension was applied during carbonization.

Stabilization time (min)	Tensile strength (MPa)	Tensile Modulus (GPa)
60	497 <sup>±79</sup>	47.8 <sup>±7.2</sup>
90	628 <sup>±43</sup>	51.4 <sup>±5.7</sup>
120	679 <sup>±64</sup>	56.0 <sup>±2.3</sup>
150	547 <sup>±66</sup>	46.0 <sup>±3.2</sup>
180	490 <sup>±88</sup>	45.5 <sup>±4.8</sup>

SEM images show relatively less defects on fiber surface when stabilization was performed for 120 min (Figure 8.6a) at constant length, and with increasing the stabilization time the number of defects increased (Figure 8.6b, c). These surface defects were carried to the resultant carbonized fibers as shown in Figure 8.6e for yarns stabilized for 180 min at constant length. During the stabilization without applying any constraint, the length of the yarns decreases as the stabilization reaction progresses (Figure 7.6a). In other words, if stabilization is performed at constant length, the tension on the yarn increases with time. Although applying tension during stabilization improves the orientation of the fibers, too much tension can introduce defects in the fibers. Thus, a controlled amount of tension during stabilization is required for better mechanical properties of the carbonized fiber. Moreover, the mechanical properties of the carbonized yarns depend not only on the strength but also on the alignment of the individual CNFs. It can be seen from Figure 8.6d, e that the alignment of the CNFs was not great in the carbonized yarns, which is another reason to see lower mechanical strength of the carbonized yarns. Thus, pre-stretching of the as spun yarns as well as

controlled amount of tension during stabilization and carbonization are required to maximize the mechanical strength of the carbonized yarns.

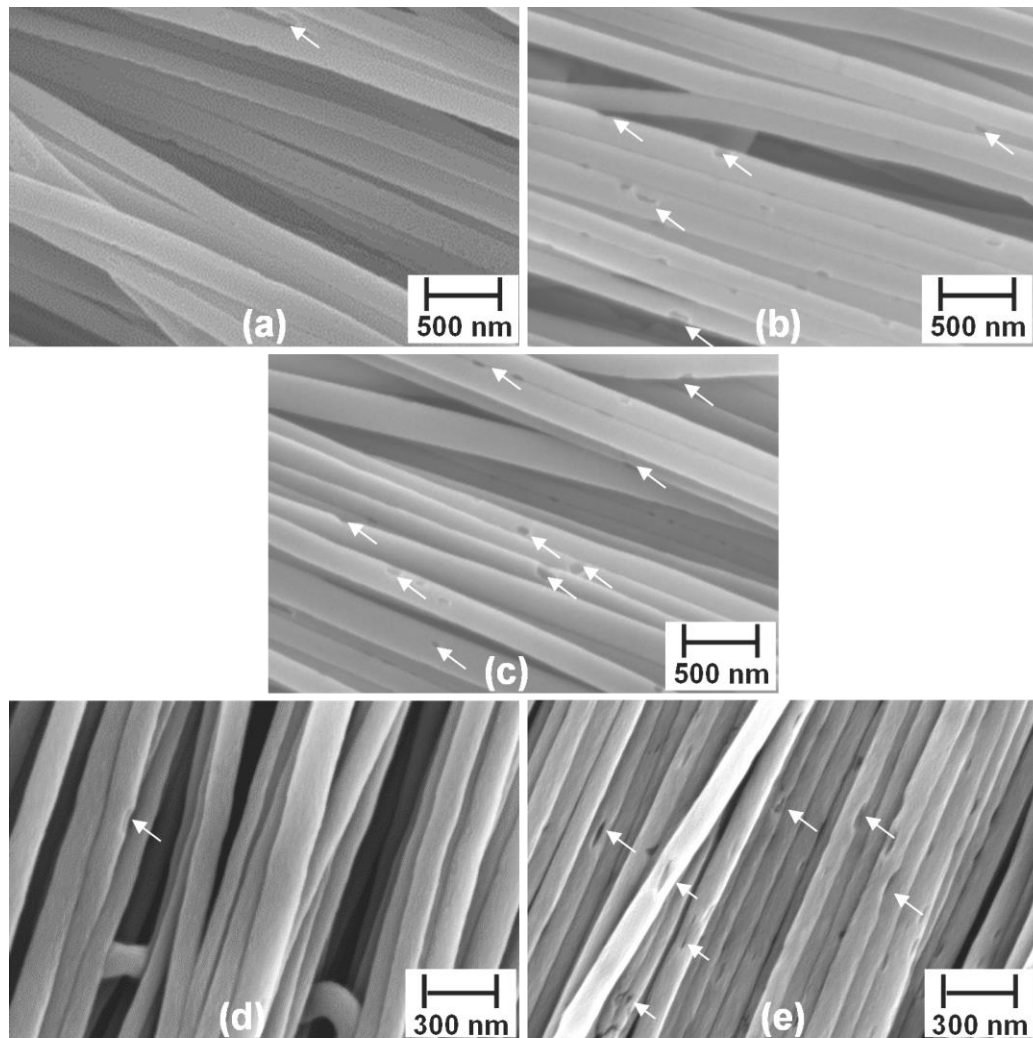


**Figure 8.8** Morphology of yarns stabilized at constant length at 260°C for (a) 120 min, (b) 150 min, and (c) 180 min, and morphology of yarns showed (d) in a and (e) in c after carbonization. Arrows showing the defects on the surface.

#### **8.4 Chapter Conclusions**

According to the WAXD results of stabilized yarns and the mechanical properties of carbonized yarns, the transition times, evaluated from in situ shrinkage measurement and dynamic mechanical analysis, during oxidative stabilization, can be used to narrow down the stabilization time range. The optimum stabilization time for isothermal treatment, after reaching to 260°C at a ramp rate of 5°C/min, was found to be 150 min. Constant length stabilization helps improving the mechanical performance of the carbonized yarns, however also introduces defects in the structure due to too much tension resulting from shrinkage force.

## Chapter 9: CONCLUDING REMARKS

### 9.1 Inferences

In this work efforts have been made to address five research questions posted under sections 2.5 and 6.5. An electrospinning based process technology has been developed to fabricate continuous PAN-based CNF yarns. The influence of various process parameters on the microstructure and mechanical properties of electrospun PAN nanofiber have been investigated. The mechanism of pore formation during electrospinning has also been explored. The kinetics of various reactions during stabilization of electrospun PAN nanofibers has been studied to attain optimum stabilization time. The major conclusions that can be drawn from the current study can be grouped as follows:

- The deposited electrospun nanofiber can be aligned by using a disc ( $w = 1.27$  cm,  $d = 25$  cm), rotating at 600 rpm or higher, as a collector. After immersing in distilled water, the aligned electrospun nanofibers can be peeled off from the surface of the collector in the form of yarn.
- The influence of electric field and flow rate on the diameter of electrospun nanofiber cannot be isolated, rather they are unified. A set of electric field and flow rate conditions with minimal jet fluctuation can be determined by analyzing the Taylor cone morphology and monitoring the fiber current. Nanofibers made in these conditions are thinnest and exhibit highest tensile strength, modulus, and stiffness.

- Ternary phase diagram of water/DMF/PAN can be utilized to better understand the mechanism of pore formation during electrospinning. The competition between solvent drying and VIPS is found to be the deciding factor of the morphology evolution of the fibers during electrospinning. At low RH, the former prevails, and solid and smooth fibers are produced along with beads on fiber, which is a consequence of capillary instability. While, VIPS plays a vital role at high RH and porous fibers with large diameter and rough surface are observed. The size of the miscible area in the ternary phase diagram decides the RH level at which the transition from solid structure to porous structure happens. The mechanical properties of solid fibers are found to be dictated by diameter and crystallinity, while amount of porosity is the most influential factor for porous nanofibers. Annealing is found to reduce the porosity of the fiber, and hence, enhances the mechanical performance of the fiber.
- DSC, TGA, shrinkage, and DMA can be used as in situ characterization techniques to understand the kinetics of various stabilization reactions. The cyclization reaction is found to have the highest activation energy followed by oxidation/dehydrogenation and crosslinking reactions. It is found that cyclization reaction in air progresses by two different mechanisms such as temperature dependent radical cyclization and ionic cyclization which is limited by the rate of oxygen diffusion. The extent of cyclization reaction is determined from the derivative of shrinkage curve, while the transition time of crosslinking reaction becoming dominant is evaluated from dynamic mechanical analysis.

- WAXD of stabilized yarns and mechanical performance of carbonized yarns show that the transition times, evaluated from in situ shrinkage measurement and dynamic mechanical analysis during oxidative stabilization, can be used to narrow down the stabilization time range. Applying tension during stabilization is found to improve the properties of carbonized nanofiber; however the tension should be controlled to avoid introducing defects in the structure.

## **9.2 Contributions**

This dissertation has contributed in the field of electrospinning by introducing unique techniques to investigate and explain the influence of various process parameters on physico-mechanical properties of electrospun nanofibers. It has also set the foundation toward the development of strong ECNFs for composite applications.

Contributions in the field of electrospinning:

- Analysis of the morphology of Taylor cone at the tip of the needle and monitor the fiber current to better understand the influence of electric field and flow rate during electrospinning.
- Validation of the relationship between volumetric charge density and nanofiber diameter, which means higher flow rate can be achieved by employing higher electrospinning voltage, leading to higher production rate without trading off the physical and structural properties of the nanofibers.

- Explanation of the mechanism of morphology and structure evolution during electrospinning by the means of water/solvent/polymer ternary phase diagram. This can help maneuvering the internal porosity and surface morphology of electrospinning nanofibers by controlling RH and temperature, which will lead to ever-increasing opportunities in new applications such as drug delivery, tissue engineering, regenerative medicine, and energy storage applications.
- Development of simultaneously strong and tough electrospun nanofibers by choosing right combination of process parameters. This unique dual nano-macro nature of electrospun nanofibers provides an easy way to bridge scales and makes them readily available for macroscopic applications.

Contributions toward the development of ECNF yarns:

- Utilization of various in situ characterization techniques such as DSC, TGA, shrinkage, and DMA to understand the kinetics of individual stabilization reactions.
- Analysis of data from in situ characterization techniques to narrow down the stabilization time range, that to be investigated for optimization. This will significantly reduce experimentation effort.

### **9.3 Recommendations for Future Work**

In this research, the electrospun PAN nanofibers produced at 20°C under 22% RH are aligned, uniform, smooth, and solid, and can be considered as near to perfect precursor

nanofibers for manufacturing ECNFs. However, the mechanical properties of the final carbonized nanofiber yarns were much lower than traditional carbon micro fibers. To improve the mechanical performance of the ECNFs, following recommendations are made:

- Although conventional spinning method produces fibers with lower macromolecular orientation as compared to electrospun nanofiber, the conventional as spun fibers are stretched to increase the orientation before heat treatment. In this dissertation, the electrospun PAN nanofibers were not stretched which may be one of the reasons to see lower strength of the ECNFs. Thus, a systematic study on the influence of various amount of stretching before heat treatment on the macromolecular orientation of the nanofibers, and how it affects the physical and mechanical changes of the fibers in the subsequent heat treatments, are recommended.
- If tension is not applied during stabilization, the orientation of the as spun stretched fibers can be lost. However, the applied tension should be controlled to avoid introducing defects in the fiber, as shown in section 8.3.3. Therefore, an investigation on the effects of various controlled amount of tension on the mechanical performance of final ECNFs is important.
- As happens during stabilization, fibers may lose the orientation during carbonization. Thus, an arrangement should be made to apply controlled amount of



tension during carbonization. The furnace used in this study cannot be utilized to make such arrangement. A tube furnace is recommended for this study.

- It has been shown in various research studies that PAN co-polymer is advantageous over PAN homo-polymer. It significantly lowers the cyclization temperature, and less heat is released during heat treatment, which means less possibility of local heating. Almost all the high strength commercial CFs are made from PAN co-polymer. In this research PAN homo-polymer was used which can be replaced by PAN co-polymer in future studies.
- Finally, mechanical characterization of the individual ECNFs along with WAXD studies of the carbonized yarns would provide better understanding of the structural changes at micro and molecular level during carbonization.

## REFERENCES

- [1] Fitzer, Erich, and Manocha, L.M. *Carbon Reinforcements and Carbon/Carbon Composites*. Springer-Verlag, Berlin (1998): 3-69.
- [2] Mimeault, V.J., and McKee, D.W. "Surface Properties of Carbon Fibers." *Carbon* 10, no. 3 (1972): 330-31.
- [3] Bacon, Roger, and Charles T. Moses. "Carbon Fibers, from Light Bulbs to Outer Space." In *High Performance Polymers: Their Origin and Development*. Springer, Netherlands (1986): 341-353.
- [4] Park, Soo-Jin, and Seul-Yi Lee. "History and Structure of Carbon Fibers." In *Carbon Fibers*. Springer, Netherlands (2015): 1-30.
- [5] Park, Soo-Jin, and Long-Yue Meng. "Surface Treatment and Sizing of Carbon Fibers." In *Carbon Fibers*. Springer, Netherlands (2015): 101-133.
- [6] Kim, Yoong A., Hayashi, T., Endo, M., Dresselhaus, M. S. "Carbon nanofibers." In *Springer Handbook of Nanomaterials*. Springer, Berlin-Heidelberg (2013): 233-262.
- [7] Fitzer, Erich. *Carbon fibres and their composites*. Springer, New York (1985).
- [8] Liu, Jie, Zhongren Yue, and Hao Fong. "Continuous nanoscale carbon fibers with superior mechanical strength." *Small* 5, no. 5 (2009): 536-542.
- [9] Johnson, J. W., and D. J. Thorne. "Effect of internal polymer flaws on strength of carbon fibres prepared from an acrylic precursor." *Carbon* 7, no. 6 (1969): 659-661.
- [10] Thorne, Derek J. "Carbon fibres with large breaking strain." *Nature* 248, (1974): 754-756.
- [11] Teo, Kenneth BK, Charanjeet Singh, Manish Chhowalla, and William I. Milne. "Catalytic synthesis of carbon nanotubes and nanofibers." *Encyclopedia of Nanoscience and Nanotechnology* 10, no. 1 (2003): 665-686.
- [12] Mordkovich, V. Z. "Carbon nanofibers: a new ultrahigh-strength material for chemical technology." *Theoretical Foundations of Chemical Engineering* 37, no. 5 (2003): 429-438.
- [13] Ozkan, Tanil, Mohammad Naraghi, and Ioannis Chasiotis. "Mechanical properties of vapor grown carbon nanofibers." *Carbon* 48, no. 1 (2010): 239-244.

- [14] Peng, Bei, Mark Locascio, Peter Zapol, Shuyou Li, Steven L. Mielke, George C. Schatz, and Horacio D. Espinosa. "Measurements of near-ultimate strength for multiwalled carbon nanotubes and irradiation-induced crosslinking improvements." *Nature Nanotechnology* 3, no. 10 (2008): 626-631.
- [15] Greßler, Sabine, René Fries, and Myrtil Simkó. "Carbon Nanotubes–Part I: Introduction, Production, Areas of Application (NanoTrust Dossier No. 022en–February 2012)."
- [16] Yu, Decai, and Feng Liu. "Synthesis of carbon nanotubes by rolling up patterned graphene nanoribbons using selective atomic adsorption." *Nano Letters* 7, no. 10 (2007): 3046-3050.
- [17] Grobert, Nicole. "Carbon nanotubes–becoming clean." *Materials Today* 10, no. 1 (2007): 28-35.
- [18] Andrews, Rodney, David Jacques, Dali Qian, and Terry Rantell. "Multiwall carbon nanotubes: synthesis and application." *Accounts of Chemical Research* 35, no. 12 (2002): 1008-1017.
- [19] Neubauer, E., M. Kitzmantel, M. Hulman, and P. Angerer. "Potential and challenges of metal-matrix-composites reinforced with carbon nanofibers and carbon nanotubes." *Composites Science and Technology* 70, no. 16 (2010): 2228-2236.
- [20] Pfautsch, Emily. "Challenges in commercializing carbon nanotube composites." *WISE Journal of Engineering and Public Policy* 11 (2007): 1-42.
- [21] Du, J. H., Jinbo Bai, and H. M. Cheng. "The present status and key problems of carbon nanotube based polymer composites." *Express Polymer Letters* 1, no. 5 (2007): 253-273.
- [22] Behabtu, Natnael, Colin C. Young, Dmitri E. Tsentalovich, Olga Kleinerman, Xuan Wang, Anson WK Ma, E. Amram Bengio et al. "Strong, light, multifunctional fibers of carbon nanotubes with ultrahigh conductivity." *Science* 339, no. 6116 (2013): 182-186.
- [23] Lu, Weibang, Mei Zu, Joon-Hyung Byun, Byung-Sun Kim, and Tsu-Wei Chou. "State of the art of carbon nanotube fibers: opportunities and challenges." *Advanced Materials* 24, no. 14 (2012): 1805-1833.
- [24] Doshi, Jayesh, and D.H. Reneker. "Electrospinning Process and Applications of Electrospun Fibers." *Industry Applications Society Annual Meeting, Conference Record of the 1993 IEEE*, (1993): 1698-703.
- [25] Reneker, Darrell H., and Iksoo Chun. "Nanometre diameter fibres of polymer, produced by electrospinning." *Nanotechnology* 7, no. 3 (1996): 216.

- [26] DZENIS, Yuris. "Spinning continuous fibers for nanotechnology." *Science* 304, no. 5679 (2004): 1917-1919.
- [27] Chun, Iksoo, Darrell H. Reneker, Hao Fong, Xiaoyan Fang, Joe Deitzel, Nora Beck Tan, and Kristen Kearns. "Carbon nanofibers from polyacrylonitrile and mesophase pitch." *Journal of Advanced Materials* 31, no. 1 (1999): 36-41.
- [28] Zhang, Lifeng, Alex Aboagye, Ajit Kelkar, Chuilin Lai, and Hao Fong. "A review: carbon nanofibers from electrospun polyacrylonitrile and their applications." *Journal of Materials Science* 49, no. 2 (2014): 463-480.
- [29] Reneker, Darrell H., Alexander L. Yarin, Hao Fong, and Sureeporn Koombhongse. "Bending instability of electrically charged liquid jets of polymer solutions in electrospinning." *Journal of Applied physics* 87, no. 9 (2000): 4531-4547.
- [30] Arinstein, Arkadii, Michael Burman, Oleg Gendelman, and Eyal Zussman. "Effect of supramolecular structure on polymer nanofibre elasticity." *Nature Nanotechnology* 2, no. 1 (2007): 59-62.
- [31] Zussman, E., M. Burman, A. L. Yarin, R. Khalfin, and Y. Cohen. "Tensile deformation of electrospun nylon-6,6 nanofibers." *Journal of Polymer Science Part B: Polymer Physics* 44, no. 10 (2006): 1482-1489.
- [32] Zong, Xinhua, Kwangsok Kim, Dufei Fang, Shaofeng Ran, Benjamin S. Hsiao, and Benjamin Chu. "Structure and process relationship of electrospun bioabsorbable nanofiber membranes." *Polymer* 43, no. 16 (2002): 4403-4412.
- [33] Jones, B. F., and R. G. Duncan. "The effect of fibre diameter on the mechanical properties of graphite fibres manufactured from polyacrylonitrile and rayon." *Journal of Materials Science* 6, no. 4 (1971): 289-293.
- [34] Fennessey, Sian F., and Richard J. Farris. "Fabrication of aligned and molecularly oriented electrospun polyacrylonitrile nanofibers and the mechanical behavior of their twisted yarns." *Polymer* 45, no. 12 (2004): 4217-4225.
- [35] Rahaman, Muhammad Syukri Abdul, Ahmad Fauzi Ismail, and Azeman Mustafa. "A review of heat treatment on polyacrylonitrile fiber." *Polymer Degradation and Stability* 92, no. 8 (2007): 1421-1432.
- [36] Wangxi, Zhang, Liu Jie, and Wu Gang. "Evolution of structure and properties of PAN precursors during their conversion to carbon fibers." *Carbon* 41, no. 14 (2003): 2805-2812.
- [37] Sánchez-Soto, Pedro José, M. A. Avilés, J. C. del Río, J. M. Ginés, J. Pascual, and J. L. Pérez-Rodríguez. "Thermal study of the effect of several solvents on

- polymerization of acrylonitrile and their subsequent pyrolysis." *Journal of Analytical and Applied Pyrolysis* 58 (2001): 155-172.
- [38] Wiles, Kenton B. "Determination of reactivity ratios for acrylonitrile/methyl acrylate radical copolymerization via nonlinear methodologies using real time FTIR." PhD diss., Virginia Polytechnic Institute and State University (2002).
- [39] Park, Soo-Jin, and Gun-Young Heo. "Precursors and Manufacturing of Carbon Fibers." In *Carbon Fibers*, Springer, Netherlands (2015): 31-66.
- [40] Huang, Xiaosong. "Fabrication and Properties of Carbon Fibers." *Materials* 2, no. 4 (2009): 2369-2403.
- [41] Lian, Feng, Jie Liu, Zhaokun Ma, and Jieying Liang. "Stretching-induced deformation of polyacrylonitrile chains both in quasicrystals and in amorphous regions during the in situ thermal modification of fibers prior to oxidative stabilization." *Carbon* 50, no. 2 (2012): 488-499.
- [42] Wu, Gangping, Chunxiang Lu, Licheng Ling, Aimin Hao, and Fu He. "Influence of tension on the oxidative stabilization process of polyacrylonitrile fibers." *Journal of Applied Polymer Science* 96, no. 4 (2005): 1029-1034.
- [43] Lindenmeyer, P. H., and R. Hosemann. "Application of the theory of paracrystals to the crystal structure analysis of polyacrylonitrile." *Journal of Applied Physics* 34, no. 1 (1963): 42-45.
- [44] Gupta, A., and I. R. Harrison. "New aspects in the oxidative stabilization of PAN-based carbon fibers." *Carbon* 34, no. 11 (1996): 1427-1445.
- [45] Nataraj, S. K., K. S. Yang, and T. M. Aminabhavi. "Polyacrylonitrile-based nanofibers-a state-of-the-art review." *Progress in Polymer Science* 37, no. 3 (2012): 487-513.
- [46] Tucker, Nick, Jonathan J. Stanger, Mark P. Staiger, Hussam Razzaq, and Kathleen Hofman. "The History of the Science and Technology of Electrospinning from 1600 to 1995." *Journal of Engineered Fabrics & Fibers* 7, no. 3 (2012).
- [47] Zeleny, John. "Instability of electrified liquid surfaces." *Physical Review* 10, no. 1 (1917): 1-6.
- [48] Vonnegut, Bernard, and Raymond L. Neubauer. "Production of monodisperse liquid particles by electrical atomization." *Journal of Colloid Science* 7, no. 6 (1952): 616-622.

- [49] Taylor, Geoffrey. "Studies in electrohydrodynamics. I. The circulation produced in a drop by electrical field." *Proceedings of the Royal Society of London A: Mathematical, Physical and Engineering Sciences* 291, no. 1425 (1966): 159-166.
- [50] Cooley, John F. "Apparatus for electrically dispersing fluids." U.S. Patent 692,631, issued February 4, 1902.
- [51] Anton, Formhals. "Process and apparatus for preparing artificial threads." U.S. Patent 1,975,504, issued October 2, 1934.
- [52] Anton, Formhals. "Artificial thread and method of producing same." U.S. Patent 2,187,306, issued January 16, 1940.
- [53] Anton, Formhals. "Production of artificial fibers from fiber forming liquids." U.S. Patent 2,323,025, issued June 29, 1943.
- [54] Anton, Formhals. "Method and apparatus for spinning." U.S. Patent 2,349,950, issued May 30, 1944.
- [55] Norton, Charles L. "Method of and apparatus for producing fibrous or filamentary material." U.S. Patent 2,048,651, issued July 21, 1936.
- [56] Taylor, Geoffrey. "Electrically driven jets." *Proceedings of the Royal Society of London A: Mathematical, Physical and Engineering Sciences* 313, no. 1515 (1969): 453-475.
- [57] Taylor, Geoffrey. "Disintegration of water drops in an electric field." *Proceedings of the Royal Society of London A: Mathematical, Physical and Engineering Sciences* 280, no. 1382 (1964): 383-397.
- [58] Baumgarten, Peter K. "Electrostatic spinning of acrylic microfibers." *Journal of Colloid and Interface Science* 36, no. 1 (1971): 71-79.
- [59] Feng, J. J. "The stretching of an electrified non-Newtonian jet: A model for electrospinning." *Physics of Fluids* 14, no. 11 (2002): 3912-3926.
- [60] Li, Wan-Ju, Cato T. Laurencin, Edward J. Caterson, Rocky S. Tuan, and Frank K. Ko. "Electrospun nanofibrous structure: a novel scaffold for tissue engineering." *Journal of biomedical materials research* 60, no. 4 (2002): 613-621.
- [61] Yoo, Hyuk Sang, Taek Gyoung Kim, and Tae Gwan Park. "Surface-functionalized electrospun nanofibers for tissue engineering and drug delivery." *Advanced Drug Delivery Reviews* 61, no. 12 (2009): 1033-1042.

- [62] Buchko, Christopher J., Kenneth M. Kozloff, and David C. Martin. "Surface characterization of porous, biocompatible protein polymer thin films." *Biomaterials* 22, no. 11 (2001): 1289-1300
- [63] Sill, Travis J., and Horst A. von Recum. "Electrospinning: applications in drug delivery and tissue engineering." *Biomaterials* 29, no. 13 (2008): 1989-2006.
- [64] Huang, Zheng-Ming, Chuang-Long He, Aizhao Yang, Yanzhong Zhang, Xiao-Jian Han, Junlin Yin, and Qingsheng Wu. "Encapsulating drugs in biodegradable ultrafine fibers through co-axial electrospinning." *Journal of Biomedical Materials Research Part A* 77, no. 1 (2006): 169-179.
- [65] Wang, Liuyang, Juan Xie, Lixia Gu, and Gang Sun. "Preparation of antimicrobial polyacrylonitrile fibers: Blending with polyacrylonitrile-co-3-allyl-5, 5-dimethylhydantoin." *Polymer Bulletin* 56, no. 2-3 (2006): 247-256.
- [66] Yun, Ki Myoung, Christopher J. Hogan, Yasuko Matsubayashi, Masaaki Kawabe, Ferry Iskandar, and Kikuo Okuyama. "Nanoparticle filtration by electrospun polymer fibers." *Chemical Engineering Science* 62, no. 17 (2007): 4751-4759.
- [67] Liu, Lei, Zhaoyang Liu, Hongwei Bai, and Darren Delai Sun. "Concurrent filtration and solar photocatalytic disinfection/degradation using high-performance Ag/TiO<sub>2</sub> nanofiber membrane." *Water Research* 46, no. 4 (2012): 1101-1112.
- [68] Tian, Ye, Min Wu, Ruigang Liu, Yanxiang Li, Deqian Wang, Junjun Tan, Rongcheng Wu, and Yong Huang. "Electrospun membrane of cellulose acetate for heavy metal ion adsorption in water treatment." *Carbohydrate Polymers* 83, no. 2 (2011): 743-748
- [69] Xiang, Hai-fan, Shuai-xia Tan, Xiao-lan Yu, Yu-hua Long, Xiao-li Zhang, and Ning Zhao. "Sound absorption behavior of electrospun polyacrylonitrile nanofibrous membranes." *Chinese Journal of Polymer Science* 29, no. 6 (2011): 650-657.
- [70] Gibson, Phillip, Heidi Schreuder-Gibson, and Donald Rivin. "Transport properties of porous membranes based on electrospun nanofibers." *Colloids and Surfaces A: Physicochemical and Engineering Aspects* 187 (2001): 469-481.
- [71] Patel, Alpa C., Shuxi Li, Ce Wang, Wanjin Zhang, and Yen Wei. "Electrospinning of porous silica nanofibers containing silver nanoparticles for catalytic applications." *Chemistry of Materials* 19, no. 6 (2007): 1231-1238.
- [72] Doh, Seok Joo, Cham Kim, Se Geun Lee, Sung Jun Lee, and Hoyoung Kim. "Development of photocatalytic TiO<sub>2</sub> nanofibers by electrospinning and its application to degradation of dye pollutants." *Journal of Hazardous Materials* 154, no. 1 (2008): 118-127.

- [73] Huang, Xiao-Jun, Zhi-Kang Xu, Ling-Shu Wan, Christophe Innocent, and Patrick Seta. "Electrospun nanofibers modified with phospholipid moieties for enzyme immobilization." *Macromolecular Rapid Communications* 27, no. 16 (2006): 1341-1345.
- [74] Joshi, Prakash, Lifeng Zhang, Qiliang Chen, David Galipeau, Hao Fong, and Qiquan Qiao. "Electrospun carbon nanofibers as low-cost counter electrode for dye-sensitized solar cells." *ACS Applied Materials & Interfaces* 2, no. 12 (2010): 3572-3577.
- [75] Ballengee, Jason B., and Peter N. Pintauro. "Composite fuel cell membranes from dual-nanofiber electrospun mats." *Macromolecules* 44, no. 18 (2011): 7307-7314.
- [76] Fang, Jian, Haitao Niu, Hongxia Wang, Xungai Wang, and Tong Lin. "Enhanced mechanical energy harvesting using needleless electrospun poly (vinylidene fluoride) nanofibre webs." *Energy & Environmental Science* 6, no. 7 (2013): 2196-2202.
- [77] Kim, Chan, Kap Seung Yang, Masahito Kojima, Kazuto Yoshida, Yong Jung Kim, Y. Ahm Kim, and Morinobu Endo. "Fabrication of Electrospinning-Derived Carbon Nanofiber Webs for the Anode Material of Lithium-Ion Secondary Batteries." *Advanced Functional Materials* 16, no. 18 (2006): 2393-2397.
- [78] Kim, C., and K. S. Yang. "Electrochemical properties of carbon nanofiber web as an electrode for supercapacitor prepared by electrospinning." *Applied Physics Letters* 83, no. 6 (2003): 1216-1218.
- [79] Im, Ji Sun, Soo-Jin Park, Taejin Kim, and Young-Seak Lee. "Hydrogen storage evaluation based on investigations of the catalytic properties of metal/metal oxides in electrospun carbon fibers." *International Journal of Hydrogen Energy* 34, no. 8 (2009): 3382-3388.
- [80] Wu, Sujuan, Qidong Tai, and Feng Yan. "Hybrid photovoltaic devices based on poly (3-hexylthiophene) and ordered electrospun ZnO nanofibers." *The Journal of Physical Chemistry C* 114, no. 13 (2010): 6197-6200.
- [81] Pinto, N. J., A. T. Johnson Jr, A. G. MacDiarmid, C. H. Mueller, N. Theofylaktos, D. C. Robinson, and F. A. Miranda. "Electrospun polyaniline/polyethylene oxide nanofiber field-effect transistor." *Applied Physics Letters* 83, no. 20 (2003): 4244-4246.
- [82] Huang, Jiaying, Shabnam Virji, Bruce H. Weiller, and Richard B. Kaner. "Polyaniline nanofibers: facile synthesis and chemical sensors." *Journal of the American Chemical Society* 125, no. 2 (2003): 314-315.



- [83] Gupta, Pankaj, Casey Elkins, Timothy E. Long, and Garth L. Wilkes. "Electrospinning of linear homopolymers of poly (methyl methacrylate): exploring relationships between fiber formation, viscosity, molecular weight and concentration in a good solvent." *Polymer* 46, no. 13 (2005): 4799-4810.
- [84] Theron, S. A., E. Zussman, and A. L. Yarin. "Experimental investigation of the governing parameters in the electrospinning of polymer solutions." *Polymer* 45, no. 6 (2004): 2017-2030.
- [85] Geng, Xinying, Oh-Hyeong Kwon, and Jinho Jang. "Electrospinning of chitosan dissolved in concentrated acetic acid solution." *Biomaterials* 26, no. 27 (2005): 5427-5432.
- [86] Uyar, Tamer, and Flemming Besenbacher. "Electrospinning of uniform polystyrene fibers: The effect of solvent conductivity." *Polymer* 49, no. 24 (2008): 5336-5343.
- [87] Fong, H., I. Chun, and D. H. Reneker. "Beaded nanofibers formed during electrospinning." *Polymer* 40, no. 16 (1999): 4585-4592.
- [88] Ali, Ashraf A., and M. A. El-Hamid. "Electro-spinning optimization for precursor carbon nanofibers." *Composites Part A: Applied Science and Manufacturing* 37, no. 10 (2006): 1681-1687.
- [89] Heikkilä, Pirjo, and Ali Harlin. "Parameter study of electrospinning of polyamide-6." *European Polymer Journal* 44, no. 10 (2008): 3067-3079.
- [90] Zhang, Chunxue, Xiaoyan Yuan, Lili Wu, Yue Han, and Jing Sheng. "Study on morphology of electrospun poly (vinyl alcohol) mats." *European Polymer Journal* 41, no. 3 (2005): 423-432.
- [91] Pelipenko, Jan, Julijana Kristl, Biljana Janković, Saša Baumgartner, and Petra Kocbek. "The impact of relative humidity during electrospinning on the morphology and mechanical properties of nanofibers." *International journal of pharmaceutics* 456, no. 1 (2013): 125-134.
- [92] De Vrieze, Sander, Tamara Van Camp, A. Nelvig, B. Hagström, Philippe Westbroek, and Karen De Clerck. "The effect of temperature and humidity on electrospinning." *Journal of materials science* 44, no. 5 (2009): 1357-1362.
- [93] Pham, Quynh P., Upma Sharma, and Antonios G. Mikos. "Electrospinning of polymeric nanofibers for tissue engineering applications: a review." *Tissue engineering* 12, no. 5 (2006): 1197-1211.
- [94] Lee, K. H., H. Y. Kim, H. J. Bang, Y. H. Jung, and S. G. Lee. "The change of bead morphology formed on electrospun polystyrene fibers." *Polymer* 44, no. 14 (2003): 4029-4034.

- [95] Lee, Joon Seok, Kyu Ha Choi, Han Do Ghim, Sam Soo Kim, Du Hwan Chun, Hak Yong Kim, and Won Seok Lyoo. "Role of molecular weight of atactic poly (vinyl alcohol)(PVA) in the structure and properties of PVA nanofabric prepared by electrospinning." *Journal of Applied Polymer Science* 93, no. 4 (2004): 1638-1646.
- [96] Demir, Mustafa Muammer, I. Yilgor, E. E. A. Yilgor, and Burak Erman. "Electrospinning of polyurethane fibers." *Polymer* 43, no. 11 (2002): 3303-3309.
- [97] McKee, Matthew G., Garth L. Wilkes, Ralph H. Colby, and Timothy E. Long. "Correlations of solution rheology with electrospun fiber formation of linear and branched polyesters." *Macromolecules* 37, no. 5 (2004): 1760-1767.
- [98] Lin, Jinyou, Bin Ding, and Jianyong Yu. "Direct fabrication of highly nanoporous polystyrene fibers via electrospinning." *ACS Applied Materials & Interfaces* 2, no. 2 (2010): 521-528.
- [99] Lee, Keun Hyung, Hak Yong Kim, Young Min La, Douk Rae Lee, and Nak Hyun Sung. "Influence of a mixing solvent with tetrahydrofuran and N, N-dimethylformamide on electrospun poly (vinyl chloride) nonwoven mats." *Journal of Polymer Science Part B: Polymer Physics* 40, no. 19 (2002): 2259-2268.
- [100] Mit-upatham, Chidchanok, Manit Nithitanakul, and Pitt Supaphol. "Effects of Solution Concentration, Emitting Electrode Polarity, Solvent Type, and Salt Addition on Electrospun Polyamide-6 Fibers: A Preliminary Report." *Macromolecular Symposia* 216, no. 1 (2004): 293-300.
- [101] Jiang, Hongliang, Dufei Fang, Benjamin S. Hsiao, Benjamin Chu, and Weiliam Chen. "Optimization and characterization of dextran membranes prepared by electrospinning." *Biomacromolecules* 5, no. 2 (2004): 326-333.
- [102] Huang, Lei, Karthik Nagapudi, Robert P. Apkarian, and Elliot L. Chaikof. "Engineered collagen-PEO nanofibers and fabrics." *Journal of biomaterials science. Polymer edition* 12, no. 9 (2001): 979-993.
- [103] Fong, Hao, and Darrell H. Reneker. "Elastomeric nanofibers of styrene-butadiene-styrene triblock copolymer." *Journal of Polymer Science Part B: Polymer Physics* 37, no. 24 (1999): 3488-3493.
- [104] Liu, Haiqing, and You-Lo Hsieh. "Ultrafine fibrous cellulose membranes from electrospinning of cellulose acetate." *Journal of Polymer Science Part B: Polymer Physics* 40, no. 18 (2002): 2119-2129.
- [105] Li, Yan, Zhengming Huang, and Yandong Lǔ. "Electrospinning of nylon-6, 66, 1010 terpolymer." *European Polymer Journal* 42, no. 7 (2006): 1696-1704.

- [106] Yuan, Xiaoyan, Yuanyuan Zhang, Cunhai Dong, and Jing Sheng. "Morphology of ultrafine polysulfone fibers prepared by electrospinning." *Polymer International* 53, no. 11 (2004): 1704-1710.
- [107] Du, Jinmei, Samantha Shintay, and Xiangwu Zhang. "Diameter control of electrospun polyacrylonitrile/iron acetylacetonate ultrafine nanofibers." *Journal of Polymer Science Part B: Polymer Physics* 46, no. 15 (2008): 1611-1618.
- [108] Yördem, O. S., Melih Papila, and Yusuf Z. Menceloğlu. "Effects of electrospinning parameters on polyacrylonitrile nanofiber diameter: An investigation by response surface methodology." *Materials & Design* 29, no. 1 (2008): 34-44.
- [109] Buchko, Christopher J., Loui C. Chen, Yu Shen, and David C. Martin. "Processing and microstructural characterization of porous biocompatible protein polymer thin films." *Polymer* 40, no. 26 (1999): 7397-7407.
- [110] Megelski, Silke, Jean S. Stephens, D. Bruce Chase, and John F. Rabolt. "Micro- and nanostructured surface morphology on electrospun polymer fibers." *Macromolecules* 35, no. 22 (2002): 8456-8466.
- [111] Tan, S. H., R. Inai, M. Kotaki, and S. Ramakrishna. "Systematic parameter study for ultra-fine fiber fabrication via electrospinning process." *Polymer* 46, no. 16 (2005): 6128-6134.
- [112] Ki, Chang Seok, Doo Hyun Baek, Kyung Don Gang, Ki Hoon Lee, In Chul Um, and Young Hwan Park. "Characterization of gelatin nanofiber prepared from gelatin-formic acid solution." *Polymer* 46, no. 14 (2005): 5094-5102.
- [113] Tripatanasuwan, Sureporn, Zhenxin Zhong, and Darrell H. Reneker. "Effect of evaporation and solidification of the charged jet in electrospinning of poly (ethylene oxide) aqueous solution." *Polymer* 48, no. 19 (2007): 5742-5746.
- [114] Cai, Yunshen, and Michael Gevelber. "The effect of relative humidity and evaporation rate on electrospinning: fiber diameter and measurement for control implications." *Journal of Materials Science* 48, no. 22 (2013): 7812-7826.
- [115] Fashandi, Hossein, and Mohammad Karimi. "Comparative studies on the solvent quality and atmosphere humidity for electrospinning of nanoporous polyetherimide fibers." *Industrial & Engineering Chemistry Research* 53, no. 1 (2013): 235-245.
- [116] Lu, Ping, and Younan Xia. "Maneuvering the internal porosity and surface morphology of electrospun polystyrene yarns by controlling the solvent and relative humidity." *Langmuir* 29, no. 23 (2013): 7070-7078.
- [117] Kim, Byoung-Suhk, and Ick-Soo Kim. "Recent nanofiber technologies." *Polymer Reviews* 51, no. 3 (2011): 235-238.

- [118] Nasouri, Komeil, Hossein Bahrambeygi, Amir Rabbi, Ahmad Mousavi Shoushtari, and Ali Kafrou. "Modeling and optimization of electrospun PAN nanofiber diameter using response surface methodology and artificial neural networks." *Journal of Applied Polymer Science* 126, no. 1 (2012): 127-135.
- [119] Basu, Sandip, Ashwini K. Agrawal, and Manjeet Jassal. "Concept of minimum electrospinning voltage in electrospinning of polyacrylonitrile N, N-dimethylformamide system." *Journal of Applied Polymer Science* 122, no. 2 (2011): 856-866.
- [120] Samatham, Ravikant, and Kwang J. Kim. "Electric current as a control variable in the electrospinning process." *Polymer Engineering & Science* 46, no. 7 (2006): 954-959.
- [121] Pai, Chia-Ling, Mary C. Boyce, and Gregory C. Rutledge. "Morphology of porous and wrinkled fibers of polystyrene electrospun from dimethylformamide." *Macromolecules* 42, no. 6 (2009): 2102-2114.
- [122] Tan, Eunice PS, and C. T. Lim. "Effects of annealing on the structural and mechanical properties of electrospun polymeric nanofibres." *Nanotechnology* 17, no. 10 (2006): 2649.
- [123] Yang, Dayong, Bo Lu, Yong Zhao, and Xingyu Jiang. "Fabrication of aligned fibrous arrays by magnetic electrospinning." *Advanced materials* 19, no. 21 (2007): 3702-3706.
- [124] Xu, C. Y., R. Inai, M. Kotaki, and S. Ramakrishna. "Aligned biodegradable nanofibrous structure: a potential scaffold for blood vessel engineering." *Biomaterials* 25, no. 5 (2004): 877-886.
- [125] Huang, Yu, Xiangfeng Duan, Qingqiao Wei, and Charles M. Lieber. "Directed assembly of one-dimensional nanostructures into functional networks." *Science* 291, no. 5504 (2001): 630-633.
- [126] Tamura, Takuya, Ryouhei Takemori, and Hiroyoshi Kawakami. "Proton conductive properties of composite membranes containing uniaxially aligned ultrafine electrospun polyimide nanofiber." *Journal of Power Sources* 217 (2012): 135-141.
- [127] Li, Dan, Yuliang Wang, and Younan Xia. "Electrospinning of polymeric and ceramic nanofibers as uniaxially aligned arrays." *Nano Letters* 3, no. 8 (2003): 1167-1171.
- [128] Teo, W. E., and S. Ramakrishna. "A review on electrospinning design and nanofibre assemblies." *Nanotechnology* 17, no. 14 (2006): R89.

- [129] Reneker, Darrell H., and Alexander L. Yarin. "Electrospinning jets and polymer nanofibers." *Polymer* 49, no. 10 (2008): 2387-2425.
- [130] La Mora, De, and J. Fernández. "The effect of charge emission from electrified liquid cones." *Journal of Fluid Mechanics* 243 (1992): 561-574.
- [131] Yu, Deng-Guang, Gareth R. Williams, Xia Wang, Xin-Kuan Liu, Hao-Lin Li, and SW Annie Bligh. "Dual drug release nanocomposites prepared using a combination of electro spraying and electrospinning." *RSC Advances* 3, no. 14 (2013): 4652-4658.
- [132] Yarin, Alexander L., Sureeporn Koombhongse, and Darrell Hyson Reneker. "Taylor cone and jetting from liquid droplets in electrospinning of nanofibers." *Journal of Applied Physics* 90, no. 9 (2001): 4836-4846.
- [133] Fallahi, Delaram, Mehdi Rafizadeh, Naser Mohammadi, and Behrooz Vahidi. "Effect of applied voltage on jet electric current and flow rate in electrospinning of polyacrylonitrile solutions." *Polymer International* 57, no. 12 (2008): 1363-1368.
- [134] Papkov, Dimitry, Yan Zou, Mohammad Nahid Andalib, Alexander Goponenko, Stephen ZD Cheng, and Yuris A. Dzenis. "Simultaneously strong and tough ultrafine continuous nanofibers." *ACS Nano* 7, no. 4 (2013): 3324-3331.
- [135] Fridrikh, Sergey V., H. Yu Jian, Michael P. Brenner, and Gregory C. Rutledge. "Controlling the fiber diameter during electrospinning." *Physical review letters* 90, no. 14 (2003): 144502.
- [136] Hohman, Moses M., Michael Shin, Gregory Rutledge, and Michael P. Brenner. "Electrospinning and electrically forced jets. I. Stability theory." *Physics of Fluids* 13, no. 8 (2001): 2201-2220.
- [137] Hohman, Moses M., Michael Shin, Gregory Rutledge, and Michael P. Brenner. "Electrospinning and electrically forced jets. II. Applications." *Physics of fluids* 13, no. 8 (2001): 2221-2236.
- [138] Casper, Cheryl L., Jean S. Stephens, Nancy G. Tassi, D. Bruce Chase, and John F. Rabolt. "Controlling surface morphology of electrospun polystyrene fibers: effect of humidity and molecular weight in the electrospinning process." *Macromolecules* 37, no. 2 (2004): 573-578.
- [139] McCann, Jesse T., Manuel Marquez, and Younan Xia. "Highly porous fibers by electrospinning into a cryogenic liquid." *Journal of the American Chemical Society* 128, no. 5 (2006): 1436-1437.

- [140] Qi, Zhonghua, Hao Yu, Yanmo Chen, and Meifang Zhu. "Highly porous fibers prepared by electrospinning a ternary system of nonsolvent/solvent/poly (L-lactic acid)." *Materials Letters* 63, no. 3 (2009): 415-418.
- [141] Nayani, Karthik, Hari Katepalli, Chandra S. Sharma, Ashutosh Sharma, Sandip Patil, and R. Venkataraghavan. "Electrospinning combined with nonsolvent-induced phase separation to fabricate highly porous and hollow submicrometer polymer fibers." *Industrial & Engineering Chemistry Research* 51, no. 4 (2011): 1761-1766.
- [142] Zhang, Y. Z., Y. Feng, Z. M. Huang, S. Ramakrishna, and C. T. Lim. "Fabrication of porous electrospun nanofibres." *Nanotechnology* 17, no. 3 (2006): 901.
- [143] Gupta, Amit, Carl D. Saquing, Mehdi Afshari, Alan E. Tonelli, Saad A. Khan, and Richard Kotek. "Porous nylon-6 fibers via a novel salt-induced electrospinning method." *Macromolecules* 42, no. 3 (2008): 709-715.
- [144] Srinivasarao, Mohan, David Collings, Alan Philips, and Sanjay Patel. "Three-dimensionally ordered array of air bubbles in a polymer film." *Science* 292, no. 5514 (2001): 79-83.
- [145] Dayal, Pratyush, Jing Liu, Satish Kumar, and Thein Kyu. "Experimental and theoretical investigations of porous structure formation in electrospun fibers." *Macromolecules* 40, no. 21 (2007): 7689-7694.
- [146] Fashandi, H., and M. Karimi. "Characterization of porosity of polystyrene fibers electrospun at humid atmosphere." *Thermochimica Acta* 547 (2012): 38-46.
- [147] Flory, Paul J. "Principles of polymer chemistry." *The George Fisher Baker Non-resident Lectureship in Chemistry at Cornell University*. Cornell University Press, Ithaca, New York 1953: (247-264).
- [148] Tompa, Hans. *Polymer solutions*. Butterworths scientific publications, London 1956.
- [149] Yilmaz, L., and A. J. McHugh. "Analysis of nonsolvent–solvent–polymer phase diagrams and their relevance to membrane formation modeling." *Journal of Applied Polymer Science* 31, no. 4 (1986): 997-1018.
- [150] Altena, Frank W., and C. A. Smolders. "Calculation of liquid-liquid phase separation in a ternary system of a polymer in a mixture of a solvent and a nonsolvent." *Macromolecules* 15, no. 6 (1982): 1491-1497.
- [151] Fashandi, H., and M. Karimi. "Pore formation in polystyrene fiber by superimposing temperature and relative humidity of electrospinning atmosphere." *Polymer* 53, no. 25 (2012): 5832-5849.

- [152] Koningsveld, R., and L. A. Kleintjens. "Liquid-liquid phase separation in multicomponent polymer systems. X. Concentration dependence of the pair-interaction parameter in the system cyclohexane-polystyrene." *Macromolecules* 4, no. 5 (1971): 637-641.
- [153] Zhang, Jian, Youwei Zhang, and Jiongxin Zhao. "Thermodynamic study of non-solvent/dimethyl sulfoxide/polyacrylonitrile ternary systems: effects of the non-solvent species." *Polymer Bulletin* 67, no. 6 (2011): 1073-1089.
- [154] Tan, Lianjiang, Ding Pan, and Ning Pan. "Thermodynamic study of a water-dimethylformamide-polyacrylonitrile ternary system." *Journal of Applied Polymer Science* 110, no. 6 (2008): 3439-3447.
- [155] Dong, Ruijiao, Jiongxin Zhao, Youwei Zhang, and Ding Pan. "Morphology control of polyacrylonitrile (PAN) fibers by phase separation technique." *Journal of Polymer Science Part B: Polymer Physics* 47, no. 3 (2009): 261-275.
- [156] N. Schuld, B. A. Wolf, "Polymer-Solvent Interaction Parameters", in *Polymer Handbook*, 4th edition, J.Brandrup, E. H.Immergut, E. A.Grulke, Eds., John Wiley & Sons, New York (1999): 247-289
- [157] Karimi, M., W. Albrecht, M. Heuchel, Th Weigel, and A. Lendlein. "Determination of solvent/polymer interaction parameters of moderately concentrated polymer solutions by vapor pressure osmometry." *Polymer* 49, no. 10 (2008): 2587-2594.
- [158] Beevers, R. B. "The physical properties of polyacrylonitrile and its copolymers." *Journal of Polymer Science: Macromolecular Reviews* 3, no. 1 (1968): 113-254.
- [159] <http://coecs.ou.edu/Brian.P.Grady/saxssoftware.html>
- [160] Nunes, Suzana Pereira, and Takashi Inoue. "Evidence for spinodal decomposition and nucleation and growth mechanisms during membrane formation." *Journal of Membrane Science* 111, no. 1 (1996): 93-103.
- [161] Park, Hyun Chae, Yoon Po Kim, Hwa Yong Kim, and Yong Soo Kang. "Membrane formation by water vapor induced phase inversion." *Journal of Membrane Science* 156, no. 2 (1999): 169-178.
- [162] Inagaki, Michio, Ying Yang, and Feiyu Kang. "Carbon nanofibers prepared via electrospinning." *Advanced Materials* 24, no. 19 (2012): 2547-2566.
- [163] Ouyang, Qin, Lu Cheng, Haojing Wang, and Kaixi Li. "Mechanism and kinetics of the stabilization reactions of itaconic acid-modified polyacrylonitrile." *Polymer Degradation and Stability* 93, no. 8 (2008): 1415-1421.

- [164] Bashir, Z. "A critical review of the stabilisation of polyacrylonitrile." *Carbon* 29, no. 8 (1991): 1081-1090.
- [165] Fitzer, E., W. Frohs, and M. Heine. "Optimization of stabilization and carbonization treatment of PAN fibres and structural characterization of the resulting carbon fibres." *Carbon* 24, no. 4 (1986): 387-395.
- [166] Xue, Yan, Jie Liu, and Jieying Liang. "Correlative study of critical reactions in polyacrylonitrile based carbon fiber precursors during thermal-oxidative stabilization." *Polymer Degradation and Stability* 98, no. 1 (2013): 219-229.
- [167] Xue, Yan, Jie Liu, and Jieying Liang. "Kinetic study of the dehydrogenation reaction in polyacrylonitrile-based carbon fiber precursors during thermal stabilization." *Journal of Applied Polymer Science* 127, no. 1 (2013): 237-245.
- [168] Henrici-Olive, G., and S. Olive. "Inter-versus intramolecular oligomerization of nitrile groups in polyacrylonitrile." *Polymer Bulletin* 5, no. 8 (1981): 457-461.
- [169] Mittal, J., O. P. Bahl, R. B. Mathur, and N. K. Sandle. "IR studies of PAN fibres thermally stabilized at elevated temperatures." *Carbon* 32, no. 6 (1994): 1133-1136.
- [170] Zussman, E., X. Chen, W. Ding, L. Calabri, D. A. Dikin, J. P. Quintana, and R. S. Ruoff. "Mechanical and structural characterization of electrospun PAN-derived carbon nanofibers." *Carbon* 43, no. 10 (2005): 2175-2185.
- [171] Didchenko, Rostislav, and Charles D. Amata. "Rapid stabilization of polyacrylonitrile fibers prior to carbonization." U.S. Patent 3,954,947, issued May 4, 1976.
- [172] Weber, Claudia, Ulrich Altenhofen, and Helmut Zahn. "Basic Studies on the Stability of Filtration Fabrics Part I: The Effects of Sulphur Dioxide and Nitrogen Oxides on Polyacrylonitrile." *Textile Research Journal* 58, no. 9 (1988): 507-514.
- [173] Kiminta, D. M. "Rapid stabilization of acrylic precursors for carbon fibres using ammonia." *International Journal of Polymeric Materials* 23, no. 1-2 (1993): 57-65.
- [174] Watt, W. "Nitrogen evolution during the pyrolysis of polyacrylonitrile." *Nature* 236, no. 62 (1972): 10-11.
- [175] Sun, Tongqing, Yongping Hou, and Haojing Wang. "Mass DSC/TG and IR ascertained structure and color change of polyacrylonitrile fibers in air/nitrogen during thermal stabilization." *Journal of Applied Polymer Science* 118, no. 1 (2010): 462-468.
- [176] Watt, W., and W. Johnson. "Mechanism of oxidation of polyacrylonitrile fibres." *Nature* 257 (1975): 210-212.



- [177] Peebles, L. H., and J. Brandrup. "A chemical means of distinguishing between conjugated and conjugated bonds." *Die Makromolekulare Chemie* 98, no. 1 (1966): 189-203.
- [178] Standage, A. E., and R. D. Matkowsky. "Thermal oxidation of polyacrylonitrile." *European Polymer Journal* 7, no. 7 (1971): 775-783.
- [179] Henrici-Olivé, G., and S. Olivé. "The chemistry of carbon fiber formation from polyacrylonitrile." In *Industrial Developments*, Springer, Berlin-Heidelberg (1983): 1-60.
- [180] Yu, Mei-Jie, Yu-Jun Bai, Cheng-Guo Wang, Yong Xu, and Peng-Zong Guo. "A new method for the evaluation of stabilization index of polyacrylonitrile fibers." *Materials Letters* 61, no. 11 (2007): 2292-2294.
- [181] Dalton, Stephen, Frank Heatley, and Peter M. Budd. "Thermal stabilization of polyacrylonitrile fibres." *Polymer* 40, no. 20 (1999): 5531-5543.
- [182] Zhu, Y., M. A. Wilding, and S. K. Mukhopadhyay. "Estimation, using infrared spectroscopy, of the cyclization of poly (acrylonitrile) during the stabilization stage of carbon fibre production." *Journal of Materials Science* 31, no. 14 (1996): 3831-3837.
- [183] Bahl, Om Parkash, and Lalit Mohan Manocha. "Shrinkage behaviour of polyacrylonitrile during thermal treatment." *Die Angewandte Makromolekulare Chemie* 48, no. 1 (1975): 145-159.
- [184] Simitzis, Johannis, and Spyridon Soulis. "Correlation of chemical shrinkage of polyacrylonitrile fibres with kinetics of cyclization." *Polymer International* 57, no. 1 (2008): 99-105.
- [185] Liu, Yaodong, Han Gi Chae, and Satish Kumar. "Gel-spun carbon nanotubes/polyacrylonitrile composite fibers. Part I: Effect of carbon nanotubes on stabilization." *Carbon* 49, no. 13 (2011): 4466-4476.
- [186] Ogawa, H., and K. Saito. "Oxidation behavior of polyacrylonitrile fibers evaluated by new stabilization index." *Carbon* 33, no. 6 (1995): 783-788.
- [187] Devasia, Renjith, C. P. Nair, P. Sivadasan, B. K. Katherine, and K. N. Ninan. "Cyclization reaction in poly (acrylonitrile/itaconic acid) copolymer: An isothermal differential scanning calorimetry kinetic study." *Journal of Applied Polymer Science* 88, no. 4 (2003): 915-920.
- [188] Kakida, Hideto, Kohji Tashiro, and Masamichi Kobayashi. "Mechanism and kinetics of stabilization reaction of polyacrylonitrile and related copolymers I.

- relationship between isothermal DSC thermogram and FT/IR spectral change of an acrylonitrile/methacrylic acid copolymer." *Polymer Journal* 28, no. 1 (1996): 30-34.
- [189] Hou, Yongping, Tongqing Sun, Haojing Wang, and Dong Wu. "Effect of heating rate on the chemical reaction during stabilization of polyacrylonitrile fibers." *Textile Research Journal* 78, no. 9 (2008): 806-811.
- [190] Suresh, K. I., K. Saji Thomas, and C. P. Nair. "Viscoelastic properties of polyacrylonitrile terpolymers during thermo-oxidative stabilization (cyclization)." *Polymers for Advanced Technologies* 19, no. 7 (2008): 831-837.
- [191] Zussman, E., X. Chen, W. Ding, L. Calabri, D. A. Dikin, J. P. Quintana, and R. S. Ruoff. "Mechanical and structural characterization of electrospun PAN-derived carbon nanofibers." *Carbon* 43, no. 10 (2005): 2175-2185.
- [192] Zhou, Zhengping, Chuilin Lai, Lifeng Zhang, Yong Qian, Haoqing Hou, Darrell H. Reneker, and Hao Fong. "Development of carbon nanofibers from aligned electrospun polyacrylonitrile nanofiber bundles and characterization of their microstructural, electrical, and mechanical properties." *Polymer* 50, no. 13 (2009): 2999-3006.
- [193] Arshad, Salman N., Mohammad Naraghi, and Ioannis Chasiotis. "Strong carbon nanofibers from electrospun polyacrylonitrile." *Carbon* 49, no. 5 (2011): 1710-1719.
- [194] Liu, Yaodong, Han Gi Chae, and Satish Kumar. "Gel-spun carbon nanotubes/polyacrylonitrile composite fibers. Part II: Stabilization reaction kinetics and effect of gas environment." *Carbon* 49, no. 13 (2011): 4477-4486.
- [195] Kissinger, Homer E. "Reaction kinetics in differential thermal analysis." *Analytical Chemistry* 29, no. 11 (1957): 1702-1706.
- [196] Ozawa, Takeo. "Kinetic analysis of derivative curves in thermal analysis." *Journal of Thermal Analysis and Calorimetry* 2, no. 3 (1970): 301-324.
- [197] Tiptipakorn, Sunan, Siriporn Damrongsakkul, Shinji Ando, Kasinee Hemvichian, and Sarawut Rimdusit. "Thermal degradation behaviors of polybenzoxazine and silicon-containing polyimide blends." *Polymer Degradation and Stability* 92, no. 7 (2007): 1265-1278.
- [198] Nair, CP Reghunadhan, K. Krishnan, and K. N. Ninan. "Differential scanning calorimetric study on the Claisen rearrangement and thermal polymerisation of diallyl ether of bisphenols." *Thermochimica Acta* 359, no. 1 (2000): 61-67.
- [199] Beltz, L. A., and R. R. Gustafson. "Cyclization kinetics of poly (acrylonitrile)." *Carbon* 34, no. 5 (1996): 561-566.

- [200] Bajaj, P., T. V. Sreekumar, and K. Sen. "Thermal behaviour of acrylonitrile copolymers having methacrylic and itaconic acid comonomers." *Polymer* 42, no. 4 (2001): 1707-1718.
- [201] Fitzer, E., and D. J. Müller. "The influence of oxygen on the chemical reactions during stabilization of pan as carbon fiber precursor." *Carbon* 13, no. 1 (1975): 63-69.
- [202] Bashir, Z., and Sanjay Rastogi. "The Explanation of the Increase in Slope at the Tg in the Plot of d- Spacing Versus Temperature in Polyacrylonitrile." *Journal of Macromolecular Science, Part B* 44, no. 1 (2005): 55-78.
- [203] Tan, E. P. S., S. Y. Ng, and C. T. Lim. "Tensile testing of a single ultrafine polymeric fiber." *Biomaterials* 26, no. 13 (2005): 1453-1456.
- [204] Chen, Zonggang, Bo Wei, Xiumei Mo, C. T. Lim, S. Ramakrishna, and Fuzhai Cui. "Mechanical properties of electrospun collagen–chitosan complex single fibers and membrane." *Materials Science and Engineering: C* 29, no. 8 (2009): 2428-2435.
- [205] Bauer, Dieter W. "Carbon or graphite." U.S. Patent 3,991,248, issued November 9, 1976.
- [206] Bazshushtari, Afshin, and Edward L. Morris Jr. "Carbon fiber reinforced carbon/carbon composite and method of its manufacture." U.S. Patent 5,609,707, issued March 11, 1997.
- [207] Roy, D., A. K. Bhowmick, and S. K. De. "Dynamic mechanical properties of short carbon fiber-filled styrene–isoprene–styrene block copolymer." *Journal of Applied Polymer Science* 49, no. 2 (1993): 263-273.
- [208] Liu, Jie, Peixun Zhou, Lifeng Zhang, Zhaokun Ma, Jieying Liang, and Hao Fong. "Thermo-chemical reactions occurring during the oxidative stabilization of electrospun polyacrylonitrile precursor nanofibers and the resulting structural conversions." *Carbon* 47, no. 4 (2009): 1087-1095.
- [209] Wu, Gangping, Chunxiang Lu, Licheng Ling, Aimin Hao, and Fu He. "Influence of tension on the oxidative stabilization process of polyacrylonitrile fibers." *Journal of Applied Polymer Science* 96, no. 4 (2005): 1029-1034.
- [210] Edie, D. D. "The effect of processing on the structure and properties of carbon fibers." *Carbon* 36, no. 4 (1998): 345-362.